Synthesis and characterization of Sr-doped NaTaO[3] photocatalysts for water splitting

An, Longjie

(Degree)
博士（理学）

(Date of Degree)
2017-09-25

(Date of Publication)
2018-09-01

(Resource Type)
doctoral thesis

(Report Number)
甲第6997号

(URL)
https://hdl.handle.net/20.500.14094/D1006997

Doctoral Dissertation

Synthesis and characterization of Sr-doped $NaTaO_3$ photocatalysts for water splitting

（Srドープ$NaTaO_3$水分解光触媒の合成と特性分析）

July, 2017

Graduate School of Science, Kobe Univerisity

Longjie An

Table of contents

Chapter 1

General introduction

1.1 ENERGY TECHNOLOGIES

Energy is an essential element to our lives as well as food in the 21st century. Fundamentally, it keeps us warm in the winter and cools us down in the summer. Lights, cars, and smartphones are all driven by energy. In a large scale, factories and cities all demand energy to function normally. Energy has become one of the major factors configuring the modern society. Due to high energy dependence, energy demand increased significantly.

Global demand for energy rose by about 30% from 2000 to 2014. Researchers estimated the demand would increase by 25% in 2040.[1] Satisfying the growing energy demand, it requires advances in the energy technology focusing on sustainability and environmental friendliness. However, in the current state, primary energy sources are composed of oil, natural gas, and coal, all contributing to greenhouse gas emission when combusted. The use of oil alone represents 30% of the world's energy consumption. Depletion of such fossil fuels in future, which will come sooner or later, will bring unrecoverable damage to the development of human society. As sustainable energy technologies, solar energy, nuclear power, and wind power are expected as future energy technologies.

As widely known, the nuclear power plant supplies powerful energy from atomic fission. The energy is too intense that any natural disaster or artificial attack will lead to tremendous damage to residents. Meanwhile, it takes a long time to decompose nuclear waste disposal entirely. Soil leaking and water pollution usually accompany during nuclear decomposition. On the other hand, the wind power generator converts wind energy to electricity. Although it is a clean and safe energy technology, the electric-generating capacity is uncertain. Irregularly changing wind direction will reduce the amount of power. Also, a weak durability to an incredibly high wind like typhoon limited the location to make wind power generator.

Rather than those two technologies, eco-friendly solar energy has attracted attention from the author due to its safety and abundant presence on earth. The power consumption of human society in 2013 was estimated as 567 EJ (1 EJ = 10^{18} J).[1] On the other hand, the annual potential of solar energy on earth was determined in a range of 1575 - 49837 EJ,[2] which is at least three times larger than the energy needed for us to keep sustainable development of society. The question is how we can convert the abundant solar energy into another type of

energy form to easily use and store. Solar cells and photocatalysts are two leading technologies expected to converge solar energy to electrical power or chemical energy so can be directly used.

Solar cells are used to make modules which can generate electrical power from sunlight. The electricity will dispatch long distances for sustaining healthy functioning of electrical goods. Significant advances have been achieved in the development of solar cell technology since it firstly demonstrated in 1839. Nowadays, silicon-based solar cells hit a record high conversion efficiency from sunlight to electricity at 46% in highly specialized research devices come with steep price tags.[3] Taking into account the cost, efficiency records for research solar cells located in a range of 21-25%. A future with massive power plants supplying enough electrical power to cities is not merely a dream.

In addition to good news about solar cells, the technology also possesses shortcomings that are difficult to overcome. The power of electricity converted from sunlight through solar cells depends on sunlight power, which is directly controlled by a climate in particular districts. At night after sunset, with cloudy weather, or in rainy seasons, the electricity cannot be generated, although the cities still need the electrical power to function. By supplying energy sustainably, it requires extra electrical power generated from solar cells to be stored in case. However, electric power cannot be easily stored in large quantities to meet demands on a national scale. Besides, transmission of the electrical power needs good enough infrastructures between departure and destination. The construction and maintenance of the infrastructure cost a lot. How to efficiently store and transmit the energy converted from sunlight are, hence, the main problems to solve in future.

With photocatalysts, on the other hand, sunlight power will be converted to chemical energy. Upon sunlight irradiation, the photocatalysts will decompose water into hydrogen and oxygen through photocatalytic reaction. Hydrogen product is a clean energy source that can be converted to electricity via fuel cells. Compared to electricity generated with solar cells, it is easier to store and transmit hydrogen fuels which produced by splitting water. With these potentials, the author’s Ph.D. research focused on the photocatalysts.

1.2 BASIC OF THE PHOTOCATALYSTS

Schematic illustration of photocatalytic reaction for water splitting is shown in **Fig. 1.1**. To initiate complete water splitting, the band structure of the photocatalyst needs to realize two basic requirements. First, the conduction band of the photocatalyst should possess potential energy more negative than that of the standard hydrogen electrode (H^+/H_2 = 0 eV) to reduce water into hydrogen. Second, valence band should maintain more positive potential energy than the standard oxygen electrode (O_2/H_2O = 1.23 eV) to oxidize water into oxygen.

Upon light irradiation, electrons at the valence band are excited to the conduction band, while leaving holes at the valance band. With enough energy, these charge carriers reduce and oxidize water into H_2 and O_2 on the surface of the photocatalyst. The stoichiometric reaction for water splitting is shown as follow:

$$H_2O + 2h\nu \rightarrow H_2 + 1/2\ O_2$$

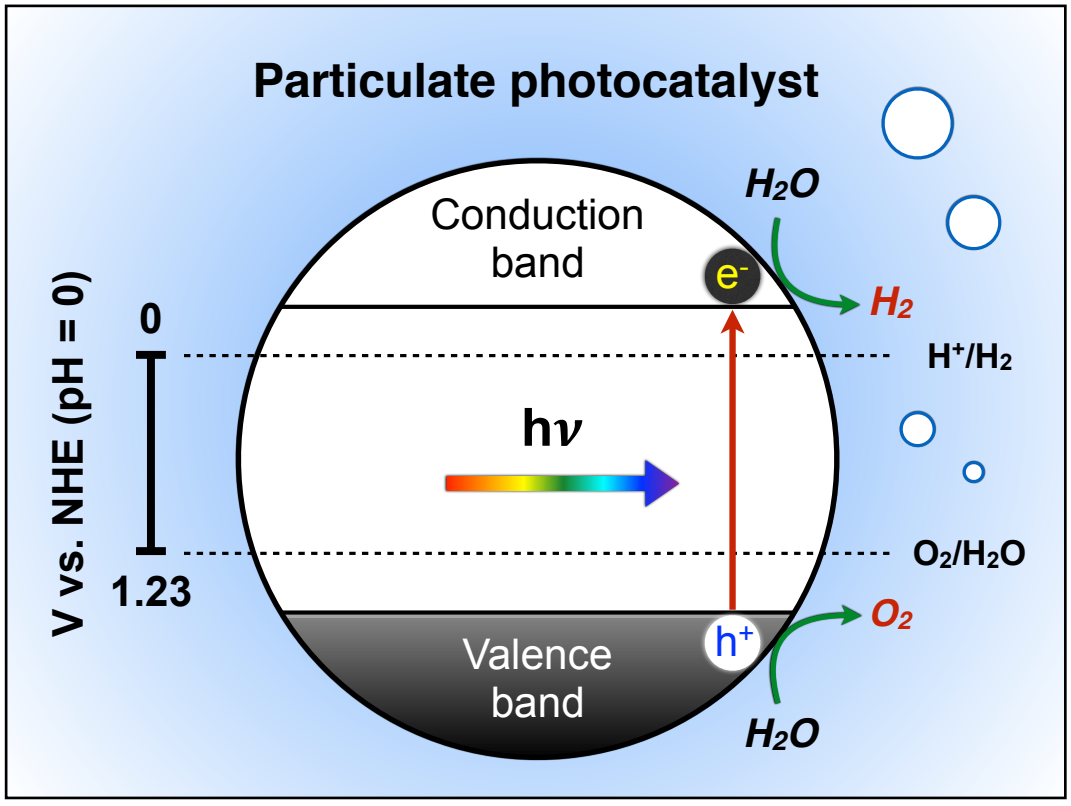

Figure 1.1 Schematic illustration of photocatalytic reaction for water splitting.

In 1972, the first electrochemical photolysis of water was reported by Fujishima and Honda.[4] The electrochemical cell was designed with circuit connection of TiO_2 and platinum electrodes. During light irradiation with a xenon lamp (500 W), water decomposed to O_2 at the TiO_2 electrode and H_2 at the platinum electrode. It suggested the water can be decomposed by light into H_2 and O_2 without any external voltage, according to following reactions:

$$TiO_2 + 2h\nu \rightarrow 2\ e^- + 2\ h^+ \quad (1)$$

(excitation of TiO_2 by light)

$$2\ h^+ + H_2O \rightarrow 1/2\ O_2 + 2\ H^+ \quad (2)$$

(at the TiO_2 electrode)

$$2\ e^- + 2\ H^+ \rightarrow H_2 \quad (3)$$

(at the platinum electrode)

Band gap energy of the rutile TiO_2 electrode is about 3.0 eV (415 nm). Light with the wavelength shorter than 415 nm can excite electrons at the valence band of TiO_2 to the conduction band. Holes left in the TiO_2 valence band oxidized water to O_2. With a more negative potential of the excited electrons moved through the circuit from TiO_2 to platinum, where to reduce water to H_2. Quantum efficiency of H_2 evolution from water splitting reached 10%.

For the application of photocatalyst, powdered TiO_2 photocatalysts were intensively studied. Platinum (Pt) was deposited on TiO_2 surface as a cathodic catalyst. Although several trials were done at an early stage, the efficiency of the reaction was too small to be detected. In 1980, Kawai and Sakata figured out the reason of low activity.[5] They attributed the low H_2 production to back reaction water decomposition in the powder systems, according to the following reaction:

$$H_2 + 1/2\ O_2 \rightarrow H_2O$$

In powdered TiO_2 loaded with Pt, the H_2 and O_2 evolution sites located very close to each other. Produced H_2 and O_2 rapidly recombined to regenerate H_2O. To prevent the backward reaction of the water splitting, gas production sites were separated by adding organic compounds. In water, excited electrons in TiO_2 powder transferred Pt for reducing water to

H_2. In organic compounds, positively charged holes remained in TiO_2 to oxidize organic compounds usually to CO_2. Through this process, the H_2 and O_2 were produced separately in different solvents. Consequently, the back reaction of water decomposition was restricted. H_2 evolution quantum efficiency was 1.2% at 380 nm when sugar was added. With water alone, this was only 0.02%. The break increase of the photocatalytic efficiency revealed possible application of powered photocatalysts. Although the sacrificed organic compounds increased the activity, the final goal of efficient photocatalytic reaction should occur in water alone by considering sustainability. How to increase the water splitting activity using powered photocatalysts in water, thus is the primary target of research in this field.

To realize the goal, understanding of what is concerned with H_2 evolution activity during the reaction is thus critical. **Figure 1.2** shows the schematic illustration of how the electrons and holes are generated and moved for water splitting. It can be divided into the following three steps:

1. As the first step, incident light excites the electrons at valence band to conduction band. Hence electron-hole pairs occurred. In this step, the incident light wavelength is decided by band gap energy of photocatalyst materials. Taking into account the solar energy is mainly composed of visible light, materials with relatively small band gap energy are desirable.

2. Excited electrons are very unstable due to their energy difference from the holes that can easily recombine with the holes to retune to the valence band. In the second step, the recombination of electrons and holes should be restricted. How to separate the electrons from the holes is the biggest challenge.

3. In the final step, the separated electrons and holes should move to surface of photocatalyst particles where the photocatalytic reaction occurs. Here the reduction and oxidation sites should be separated for confining back reaction of water splitting.

Usual consideration on the three steps for water splitting includes light excitation, charge separation and transportation to the surface, and catalytic reaction for reduction and oxidation. The author considered the 2nd step as two different processes. The 3rd step, which is directly

concerned with reaction, is little taken into account in this general introduction, to emphasize the significance of charge separation.

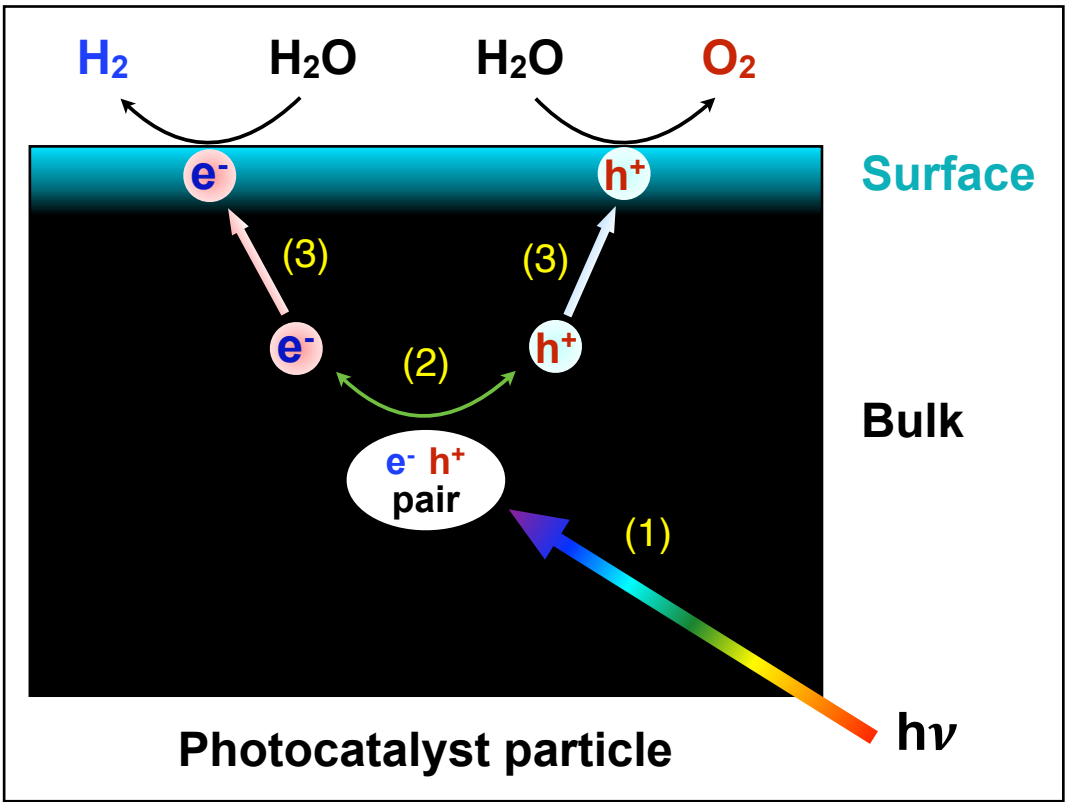

Figure 1.2 Schematic illustration of generation and evolution of charge carriers for water splitting. (1) Excitation, (2) Separation, and (3) Surface movement.

Typical photocatalysts mainly studied for splitting water are metal oxides, for example, TiO_2,[6] $SrTiO_3$,[7] or $NaTaO_3$.[8] These materials have band gap energies larger than 3.0 eV that not able to absorb visible light, but only absorb ultraviolet (UV) light. Metal sulfides and nitrides were prepared to extend the excitation light wavelength. In metal oxides photocatalysts, the valence band constitutes of O 2p orbitals. Replacement of all or some O^{2-} anions with S^{2-} and N^{3-} anions generate a new or hybridized valence band. As a result, the valence band of (oxy)sulfides or (oxy)nitrides is more negative than that of pure oxides. In this way, the band gap energy was decreased.

At the early stage, studies focused on the direct metal sulfides, like CdS.[9,10] It reduced the band gap energy to 2.4 eV. With following studies on sulfides solutions, such as $(AgIn)_xZn_{2(1-}$

$_{x)}S_2$,[11] (CuIn)xZn_2(1-x)S_2,[12] ZnS-$CuInS_2$-$AgInS_2$,[13] the quantum efficiency was increased drastically to 20% (420 nm) in the presence of sacrificing reagents. However, the stability of such sulfides was very low. During the photocatalytic reaction, S^{2-} will be oxidized to S. Similar self-oxidation can also be seen in TaON (2.4 eV).[14,15] To suppress the self-oxidation, CoO_x was loaded on TaON electrodes. Since the CoO_x nanoparticles were efficient hole scavengers, they attracted holes from TaON to CoOx. Hence the oxidation of TaON was suppressed.[16] On the other hand, loading of amorphous oxyhydroxide $CrO_{1.5-m}(OH)_{2m}\cdot xH_2O$ on surface nitrides was also confirmed to suppress self-oxidation.[17] Further reduced band gap energy of 2.1 eV (600 nm) was achieved in $LaMg_xTa_{1-x}O_{1+3x}N_{2-3x}$ solid solution. The self-oxidation of N^{3-} was suppressed by loading of $CrO_{1.5-m}(OH)_{2m}\cdot xH_2O$. However, as the first stable photocatalyst for water splitting operable at up to 600 nm, $LaMg_xTa_{1-x}O_{1+3x}N_{2-3x}$ solid solution showed the water splitting quantum efficiency at only 0.03% (440 nm).[18]

Above studies suggest the band gap engineering is significant for visible light absorption, and anion doping is an efficient way for band gap reproduction. Surface modification can help restrict self-oxidation for gaining stability of the photocatalyst material itself. However, the activity is still limited in these stable photocatalysts can be driven by visible light.

To achieve high efficiency of water splitting, excited electrons and holes should be efficiently move to the surface. Meanwhile, the charge carriers are needed to separate in different sites for restricting backward reaction of water splitting. Loading of cocatalyst on particle surface helps it by trapping electrons and holes.

Noble metals (such as Pt or Au) are usually used as cocatalysts to trap electrons, due to their high work functions.[19] These cocatalysts possess two abilities; one is to trap electrons (trapping ability), and the other is reduce H^+ into H_2 (catalytic ability).

The trapping ability is determined by the work functions of the noble metals that are larger than the most photocatalyst semiconductors. When a noble metal was loaded on the surface of TiO_2,[20] for example, a Schottky barrier was formed at the metal/TiO_2 interface. With fixed Fermi level in the TiO_2, the Schottky barrier height is unilaterally decided by Fermi level of the metal. Lower Fermi level of the metal provides stronger trapping ability. Pt, with the largest work function among many noble metals, has the lowest Fermi level, consequently, to efficiently trap electrons. On the other hand, the catalytic ability of H^+ reduction is related to

the activation energy for H_2 evolution. Pt was found to show lowest activation energy, according to an early study.[21] Therefore, Pt is usually used as H_2 evolution cocatalyst.[9,22,23]

Compared to those noble metals function as reduction cocatalysts, metal oxides work as oxidation cocatalysts, which trap holes instead of electrons. Representative oxidation cocatalysts include CoO_x, IrO_x, and RuO_x.[24-26] O_2 evolution was enhanced efficiently with these oxides cocatalysts. These oxidation cocatalysts can also increase the photostability of (oxy)sulfides and (oxy)nitrides by attracting holes.[27,28]

In $NaTaO_3$ photocatalyst,[8] loading of NiO on particle surface enhanced not only the O_2 evolution but also the H_2 evolution. The maximum quantum efficiency of H_2 evolution reached 20% at 270 nm, in the presence of sacrificial reagents. A later study showed the enhanced generation of both H_2 and O_2 might attribute to the production of Ni via the reduction from NiO during light irradiation.[29] Coexisted cocatalysts of Ni (electron trapper) and NiO (hole trapper) reduced and oxidized, respectively, water to H_2 and O_2 in different sites on $NaTaO_3$ surface.

The synergetic effect of the dual cocatalysts, for example, combination of noble metals (Pt, Au, or Pd) and metal oxides (RuO_2 or IrO_2), was already proved in Zn_2GeO_4.[30] Co-loading of Rh/Cr_2O_3 and Mn_3O_4 on GaN/ZnO photocatalyst also increased water splitting efficiency.[31] Without doubt, loading of the cocatalysts is a powerful way to transport excited electrons and holes to surface at separated sites.

As stated above, challenges on visible absorption (step 1) and charge separation (step 3), as shown in **Fig. 1.2**, were resolved finely. What about charge separation (step 2) in bulk of photocatalyst particles?

Although the cocatalyst strategy significantly increased the quantum efficiency of H_2 evolution upon UV irradiation, visible driven photocatalyst with cocatalyst still showed limited efficiency.[18] The photocatalytic water splitting is highly related to the number of excited electrons and holes reaching the surface from bulk. For increasing the number of carriers on the surface, electron-hole recombination in bulk should be restricted. Otherwise, rapid recombination of electrons and holes will reduce the number of carriers able to be alive

until reaching the surface. Suppression of electron-hole recombination in bulk, hence, is significant to increase the water spitting activity.

The most successful example of suppression to electron-hole recombination is metal-doped $NaTaO_3$. In 2000, La-doped $NaTaO_3$ was found to exhibit 56% quantum efficiency at 270 nm. [32] It is the highest efficiency for H_2 evolution from pure water so far in singular particulate photocatalysts. Doping of alkaline earth metals (Sr, Ba) showed comparable efficiency as La doping.[33] Increased efficiency induced by metal doping is attributed to restricted electron-hole recombination.[34] It explains the metal dopants somehow restricted electron-hole recombination; consequently, water splitting activity increased.

The increased activity in 2 mol% La-doped $NaTaO_3$ was assigned to ordered nano step structure formed on the particle surface.[35] H_2 and O_2 evolution sites were separated due to the nano steps. However, doping of La at larger than 2 mol% gradually reduced the activity, eventually, to the same extent as undoped $NaTaO_3$ at 10 mol% (La). This reduction of activity cannot be explained lonely with separated reaction sites over the nano steps. Besides, the mechanism of the nano step production is unclear. Thus the reason of dopants-induced activity enhancement, as well as restricted electron-hole recombination, is remained uncertain.

To understand deeply on the effect of the metal dopants on $NaTaO_3$ photocatalyst is thus the main topic of the author. Sr dopants are mainly studied and shown in this thesis. With similar water splitting activity in Sr-doped $NaTaO_3$ to La-doped $NaTaO_3$, relatively small information is known. In a comparison of La, deeper understanding on the Sr-doped $NaTaO_3$ may help make clear the mechanism of restricted electron-hole recombination. In the present study, understanding on the mechanism of nano step production was challenged. It further drew clues of suppression to electron-hole recombination, in summary.

1.3 CONTRIBUTIONS OF THE AUTHOR

Although the metal-doped $NaTaO_3$ showed the highest quantum efficiency for H_2 evolution, it only absorbs UV light. If we know the mechanism of effective suppression to electron-hole recombination in doped $NaTaO_3$, it can be strategically applied to visible driven photocatalysts loaded with the cocatalysts on the surface, so as to obtain applicable photocatalysts upon sunlight irradiation. The contributions of the author for understanding the mechanism are listed as follow;

1. In chapter 3, Sr-doped $NaTaO_3$ photocatalysts with various Sr concentrations were synthesized via solid-state method (SSM), hydrothermal method (HTM), and solvothermal method (STM), respectively. Doping sites of Sr in $NaTaO_3$ were examined and compared in the three synthesis methods. **Figure 1.3** (Page 13) shows the illustration of perovskite-structured $NaTaO_3$ for the convenience of understanding. As a result, a presence of B-sites doping via SSM and STM restricted electron-hole recombination. In SSM, Sr substituted Na at A-sites and Ta at B-sites simultaneously to form a solid solution of $NaTaO_3$-$Sr(Sr_{1/3}Ta_{2/3})O_3$. Lattice mismatch between the two materials induced nano steps on the particle surface. A-site doping alone was widely accepted before the present study due to similar ionic radii of metal dopants (Sr, La, or Ba) and Na (A-site). In this chapter, the presence of B-site doping and its significant role in the electron-hole recombination were examined and confirmed.

2. In chapter 4, Sr-doped $NaTaO_3$ (SSM) was etched with HF solution to determine radial distribution of Sr in the $NaTaO_3$ particle. Excessive doping of Sr larger than 5 mol% induced a Sr-rich shell formed on top of a Sr-poor core. The core included a smooth concentration gradient of Sr doped at B-sites. The electron-hole recombination was restricted in the core when the length of the concentration gradient of Sr at B-sites extended. A potential gradient was assumed to form in the conduction band, which comprised of Ta 5d orbital, minimum of $NaTaO_3$ to drive excited electrons in particular direction away from holes. Consequently, electron-hole recombination was restricted. Radial distribution of Sr plays a significant role in charging separation. To design a potential gradient by controlling radial distribution of dopants is an appropriate way for

gaining high suppression to electron-hole recombination. Control of the radial distribution of dopants is a key challenge.

3. In chapter 5, $NaTaO_3$ was doped with Sr at 2 mol% via molten salt method (MSM) under flexible heating time from 1 to 60 h. To control the radial distribution of Sr was the primary challenge. Under 60h-heating, the Sr distributed homogeneously over the $NaTaO_3$ particles due to complete melting of SrO used as Sr supplier. On the other hand, 1h-heating induced Sr segregation on particle surface to form inhomogeneous Sr distribution, as expected. Accordingly, the electron-hole recombination was efficiently restricted upon heating at 1 h. These results support the significant role of radial distribution of Sr to recombination of electrons and holes. Also, the heating time successfully controlled the Sr distribution.

4. In chapter 6, the local structure of Sr was observed by X-ray absorption spectroscopy (XAS) on Sr-doped $NaTaO_3$ prepared via SSM, HTM and MSM. In the observation of X-ray absorption near edge structure (XANES), the peak top energy of Sr-doped $NaTaO_3$ (SSM or MSM) was detected between that of SrO (coordination number of Sr is 6) and $SrTiO_3$ (coordination number of Sr is 12). It suggests simultaneous doping of Sr at A- and B-sites. While the Sr-doped $NaTaO_3$ (HTM) showed almost the same XANES peak top energy as $SrTiO_3$. Thus the A-site doping of Sr alone was assumed in HTM. On the other hand, in the observation of extended X-ray absorption fine structure (EXAFS), both the Sr(B)-O and Sr(A)-O coordinations were detected on Sr-doped $NaTaO_3$ (SSM or MSM). It again strongly supports the coexistence Sr doped at A- and B-sites in SSM and MSM. While in HTM, the EXAFS S/N ratio was not good enough to carefully interpret. However, the EXAFS spectrum of Sr-doped $NaTaO_3$ prepared via HTM was certainly different from SSM.

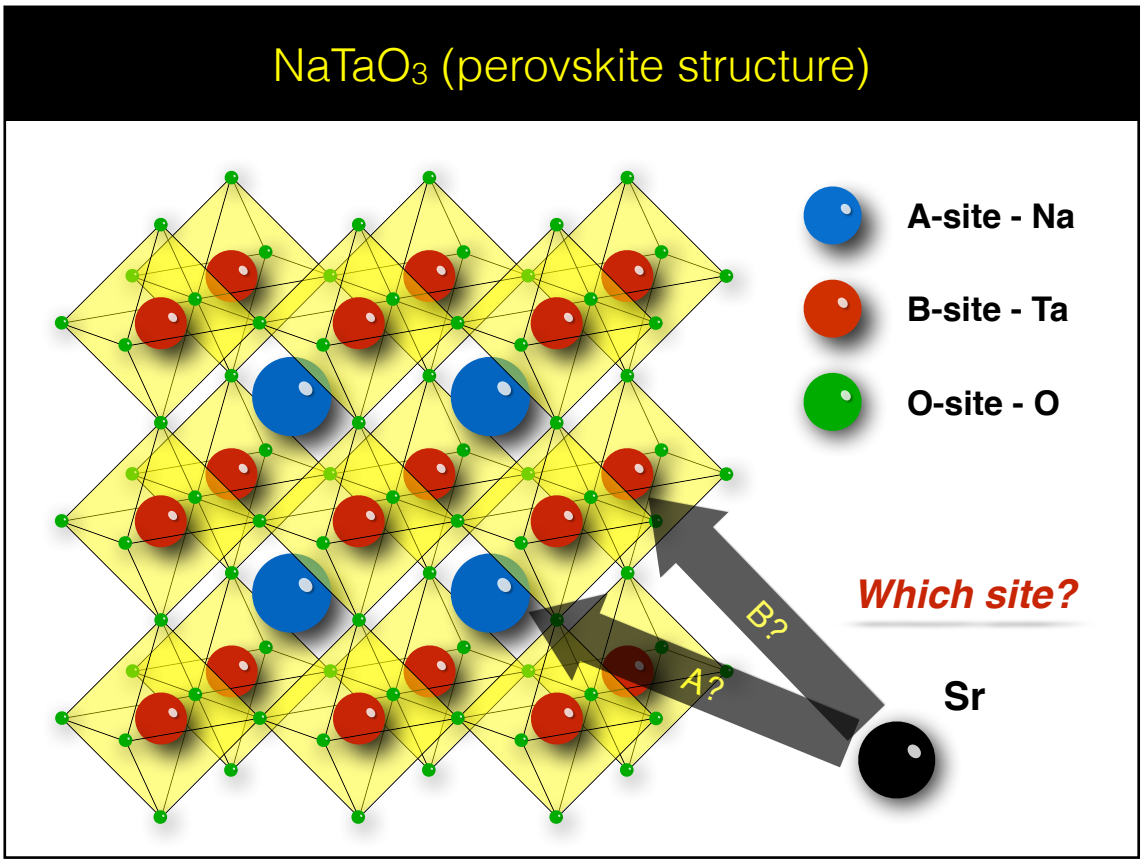

Figure 1.3 Schematic illustration of perovskite structure on $NaTaO_3$. Possible doping sites of Sr is presented.

1.4 REFERENCE

(1) *Key world Energy Statistics 2015*, **2015**, 37.

(2) *World Energy Assessment: Energy and the Challenge of Sustainability*, **2000**, 162-163.

(3) Jacoby, N. *C&EN* **2016**, *94*, 30-35.

(4) Fujishima, A.; Honda, K. *Nature* **1972**, *238*, 37-38.

(5) Kawai, T.; Sakata, T. *Nature* **1980**, *286*, 474-476.

(6) Kudo, A.; Domen, K.; Maruya, K.; Onishi, T. *Chem. Phys. Lett.* **1987**, *133*, 517-519.

(7) Domen, K.; Kudo, A.; Onishi, T. *J. Catal.* **1986**, *102*, 92-98.

(8) Kato, H.; Kudo, A. *J. Phys. Chem. B* **2001**, *105*, 4285-4292.

(9) Darwent, J. R.; Porter, G. *J. Chem. Soc., Chem. Commun.* **1981**, 145-146.

(10) Uchihara, T.; Matsumura, M.; Yamamoto, A.; Tsubomura, H. *J. Phys. Chem.* **1989**, *93*, 5870.

(11) Tsuji, I.; Kato, H.; Kobayashi, H.; Kudo, A. *J. Am. Chem. Soc.* **2004**, *126*, 13406-13413.

(12) Tsuji, I.; Kato, H.; Kobayashi, H.; Kudo, A. *J. Phys. Chem. B* **2005**, *109*, 7323-7329.

(13) Tsuji, I.; Kato, H.; Kudo, A. *Angew. Chem., Int. Ed.* **2005**, *44*, 3565-3568.

(14) Hitoki, G.; Takata, T.; Kondo, J. N.; Hara, M.; Kobayashi, H.; Domen, K. *Chem. Commun.* **2002**, 1698-1699.

(15) Chun, W. J.; Ishikawa, A.; Fujisawa, H.; Takata, T.; Kondo, J. N.; Hara, M.; Kawai, M.; Matsumoto, Y.; Domen, K. *J. Phys. Chem. B* **2003**, *107*, 1798-1803.

(16) Higashi, M.; Domen, K.; Abe, R. *J. Am. Chem. Soc.* **2012**, *134*, 6968-6971.

(17) Yoshida, M.; Takanabe, K.; Maeda, K.; Ishikawa, A.; Kubota, J.; Sakata, Y.; Ikezawa, Y.; Domen, K. *J. Phys. Chem. C* **2009**, *113*, 10151-10157.

(18) Pan, C.; Takata, T.; Nakabayashi, M.; Matsumoto, T.; Shibata, N.; Ikuhara, Y.; Domen, K. *Angew. Chem. Int. Ed.* **2015**, *54*, 2955-2959.

(19) Yang, J.; Wang, D.; Han, H.; Li, C. *Acc Chem. Res.* **2013**, *46*, 1900-1909.

(20) Leung, D. Y. C.; Fu, X. L.; Wang, C. F.; Ni, M.; Leung, M. K. H.; Wang, X. X.; Fu, X. Z. *ChemSusChem* **2010**, *3*, 681-694.

(21) Trasatti, S. *J. Electroanal. Chem.* **1972**, *39*, 163-184.

(22) Bao, N. Z.; Shen, L. M.; Takata, T.; Domen, K. *Chem. Mater.* **2008**, *20*, 110-117.

(23) Yan, H.; Yang, J.; Ma, G.; Wu, G.; Zong, X.; Lei, Z.; Shi, J.; Li, C. *J. Catal.* **2009**, *266*, 165-168.

(24) Kasahara, A.; Nukumizu, K.; Hitoki, G.; Takata, T.; Kondo, J. N.; Hara, M.; Kobayashi, H.; Domen, K. *J. Phys. Chem. A* **2002**, *106*, 6750-6753.

(25) Maeda, K.; Wang, X.; Nishihara, Y.; Lu, D.; Antonietti, M.; Domen, K. *J. Phys. Chem. C* **2009**, *113*, 4940-4947.

(26) Ma, B. J.; Yang, J. H.; Han, H. X.; Wang, J. T.; Zhang, X. H.; Li, C. *J. Phys. Chem. C* **2010**, *114*, 12818-12822.

(27) Higashi, M.; Domen, K.; Abe, R. *J. Am. Chem. Soc.* **2012**, *134*, 6968-6971.

(28) Ohno, T.; Bai, L.; Hisatomi, T.; Maeda, K.; Domen, K. *J. Am. Chem. Soc.* **2012**, *134*, 8254-8259.

(29) Zhang, Q.; Li, Z.; Wang, S.; Li, R.; Zhang, X.; Liang, Z.; Han, H.; Liao, S.; Li, C. *ACS Catal.* **2016**, *6*, 2182-2191.

(30) Ma, B. J.; Wen, F. Y.; Jiang, H. F.; Yang, J. H.; Ying, P. L.; Li, C. *Catal. Lett.* **2010**, *134*, 78-86.

(31) Maeda, K.; Xiong, A. K.; Yoshinaga, T.; Ikeda, T.; Sakamoto, N.; Hisatomi, T.; Takashima, M.; Lu, D. L.; Kanehara, M.; Setoyama, T.; Teranishi, T.; Domen, K. *Angew. Chem., Int. Ed.* **2010**, *49*, 4096-4099.

(32) Kudo, A.; Kato, H. *Chem. Phys. Lett.* **2000**, *331*, 373-377.

(33) Iwase, A.; Kato, H.; Okutomi, H.; Kudo, A. *Chem. Lett.* **2004**, *33*, 1260-1261.

(34) Maruyama, M.; Iwase, A.; Kato, H.; Kudo, A.; Onishi, H. *J. Phys. Chem. C* **2009**, *113*, 13918-13923.

(35) Kato, H.; Asakura, K.; Kudo, A. *J. Am. Chem. Soc.* **2003**, *125*, 3082-3089.

Chapter 2

Methods

2.1 SYNTHESIS

2.1.1 Solid-state method (SSM)

In the synthesis of photocatalysts, the solid-state method (SSM) is the most widely used one. Since the solid starting materials do not react at room temperature, it is necessary to heat them at about 1000-1500 °C to prepare wanted metal-oxide products.[1]

Experimental procedure can be divided into two steps, mixing and heating. In this study, starting materials (Na_2CO_3, Ta_2O_5, and $SrCO_3$) with small quantities (less than 6 g) were well ground in an agate mortar for 20 minutes to acquire a mixture. The mixture was put into an alumina crucible and heated at 1150 °C for 10 hours for the complete synthesis of Sr-doped $NaTaO_3$.

Before the mixing and the heating, the molar ratio of Na_2CO_3/Ta_2O_5 was adjusted to 1.05, due to sublimation of Na^+ during heating. Upon heating above 900 °C, Na_2CO_3 will decompose to Na_2O and CO_2 through a thermal decomposition reaction. Thus produced Na_2O can easily sublimate at 1275 °C. 1150 °C-heating should make part sublimation of Na_2O. To compensate the lost Na^+, a little more Na^+ was added in the starting mixture.

Another important issue to consider is the heating temperature. A solid-state reaction undertakes as well as a high temperature is used. However, too much high temperature induces oxygen vacancies for the metal oxides. High oxidation states in the metal oxides (MO_x) are often unstable at high temperature, due to the following thermal reaction:

$$2\ MO_x\ (s) \rightarrow 2\ MO_{x-1}\ (s) + O_2\ (g)$$

Oxygen vacancies produced in the photocatalysts may work as recombination centers to capture photoexcited electrons, consequently, to reduce the water splitting reaction. This adverse effect restricted the heating temperature from being too high. Taking into consideration of a complete synthesis of Sr-doped $NaTaO_3$ with limited oxygen vacancies, 1150 °C is an ideal reaction temperature.

2.1.2 Hydrothermal method (HTM)

In the hydrothermal method (HTM), photocatalyst particles are crystallized from hot water under high pressure. A chamber lined steel-pressure-vessel called as an autoclave is usually used to endure the high pressure created by water evaporation. Under heating, a temperature deviation is generated and maintained on the opposite sides of the chamber. The substance dissolves in aqueous solution on the hotter side, while it is deposited to form a crystal seed on the cooler side. The desired crystal thus can grow based on the crystal seed. Advantages of the hydrothermal method for the synthesis of the photocatalyst particles include a relatively low heating temperature and crystals in good quality.

In the present study, the Sr-doped $NaTaO_3$ crystal grew in a Teflon jar under 200 °C for 10 hours. Ta_2O_5 and $SrCO_3$, used as starting materials, were put into the Teflon jar containing NaOH aqueous solution. During heating in NaOH solution, Ta_2O_5 is expected to convert to $NaTaO_3$ according to the following two steps:

$$Ta_2O_5 + 5\ H_2O \rightarrow 2\ Ta(OH)_5$$

$$Ta(OH)_5 + NaOH \rightarrow NaTaO_3 + 3\ H_2O$$

NaOH not only works as a catalyst at the first step of the reaction but also a material as the second step. To drive a smooth reaction, a high concentration of Na^+ cation is necessary. $SrCO_3$ is believed to convert to $Sr(OH)_2$ for joining the second step of the reaction to produce Sr-doped $NaTaO_3$ crystals. Any residual NaOH was carefully washed with purified water until pH maintained at about 7.

2.1.3 Solvothermal method (STM)

In addition to the hydrothermal method, solvothermal method (STM) was applied to perform Sr doping on $NaTaO_3$. In the present study, the STM was used to realize B-site doping of Sr. In the structure of B-site doped $NaTaO_3$, Sr should be placed at Ta-position to form Ta-O-Sr bonds. Thus the target is to produce Ta-O-Sr bonds before heating.

The route of crystal growth through solvothermal method is very similar to the hydrothermal method. A key difference is the origin of metal cations. In the synthesis of Sr-doped $NaTaO_3$ prepared via solvothermal method, Ta^{5+} and Sr^{2+} cations were provided in the phase of alkoxides instead of oxides. $Ta(OC_2H_5)_5$ and $Sr(OC_3H_7)_2$ were dissolved in EtOH solvent to produce Ta-O-Sr bonds. Under stirring, the EtOH solution was slowly dripped into Teflon jar containing NaOH aqueous solution under cooling with ice water. Meeting with H_2O, alkoxides such as $Ta(OC_2H_5)_5$ and $Sr(OC_3H_7)_2$ converted to oxides (Ta_2O_5 and SrO) through a hydrolysis reaction. Therefore, alkoxides in EtOH solution including Ta-O-Sr bonds will convert to mixed oxides of Ta_2O_5 and SrO possessing Ta-O-Sr bonds when meeting H_2O. Cooling with ice water reduces the hydrolysis reaction so that the Ta-O-Sr bonds alive during the reaction.

Here list some key steps to realizing successful B-site doping of Sr. The first one is the dissolved condition of metal alkoxides in EtOH solvent. In the present study, ultrasonic cleaning was applied to realize complete dissolution. The second one is the dripping rate of EtOH solution into NaOH aqueous solution. The entire dripping process was lasted few minutes to make sure Ta-O-Sr bonds alive. The last one, also as the most important step, is the presence or absence of ice water cooling. Without cooling, the B-site doping failed.

2.1.4 Molten salt method (MSM)

During synthesis of Sr-doped $NaTaO_3$ via SSM, $SrCO_3$ will decompose to SrO. Compared to the other starting materials, such as Na_2O (m.p. = 1,405 K) and Ta_2O_5 (m.p. = 2,145 K), SrO (m.p. = 2,804 K) has a relatively high melting point. Consequently, doped Sr^{2+} cations mainly segregated on the surface of $NaTaO_3$ particles. To design a smooth spatial distribution of Sr in $NaTaO_3$ particles, a molten salt method (MSM) was used to synthesize Sr-doped $NaTaO_3$.

The experimental procedure of MSM is similar to that of SSM. A feature of MSM is the presence of flux reagent (NaCl) in addition to starting materials (Na_2CO_3, Ta_2O_5, and $SrCO_3$). During heating, a molten NaCl is formed to help the starting materials to move smoothly for complete reaction. The molten NaCl also helps prevent sudden cooling when the heating stops so that product crystals can grow slowly.

In MSM, a mixture of the flux reagent and the starting materials were carefully ground with agate mortar for 20 minutes. Then the mixture was heated in an alumina crucible at 1150 °C for a designed period in a range of 1-60 hours. Each product was washed with purified water to remove excess NaCl.

With the flux used in MSM, the reaction completes at relatively lower temperature than in SSM. However, the same heating temperature was applied in the MSM and SSM to compare the Sr-doped $NaTaO_3$ synthesized via the two methods.

To realize the smooth distribution of Sr, the heating time extended to 60 hours. The high melting point of SrO makes it difficult to reach the bulk of $NaTaO_3$ particles in a limited heating time.

A proper amount of flux, high temperature and long heating time are the key factors to realize smooth distribution of Sr.

2.2 CHARACTERIZATION

2.2.1 Energy-dispersive X-ray spectroscopy (EDX)

Energy-dispersive X-ray spectroscopy (EDX) is a conventional analytical technique for detecting elemental compositions of a sample. Characterization capabilities of EDX rely on a characteristic X-ray emission from a particular element, due to the unique atomic structure of each element.[2]

A primary beam of X-rays or electrons focused into samples will eject an electron from an inner electron shell, leaving a hole where the electron was. An electron from an outer shell having higher energy fills the holes, thus cause an emission of X-ray fluorescence, which is usually named as characteristic X-ray. The energy of the characteristic X-ray in a particular element is decided by the energy gap between the inner shell and outer shell, that is the atomic structure. Therefore, detection of the characteristic X-rays realizes a qualitative and a quantitative analysis of the elemental composition of a sample.

The excitation source of the EDX equipment (Shimadzu, EDX-720) used in the present study is an X-ray beam. The source consists of tungsten (W) cathode and rhodium (Rh) anode. Applying a voltage within 5-50 kV will accelerate thermal electrons from W cathode toward Rh anode. Eventually, the electron beam hits onto the Rh to create Rh-K emission, which comprises the X-ray source of the EDX equipment. The Rh-K emission allows elemental analysis ranges from $_{11}$Na to $_{92}$U. However, the characteristic X-ray signal of Na-K emission is too weak to be detected with this equipment without a vacuum device. The compositional analysis focused on Sr-Ta molar ratio to determine the Sr concentration in the products.

As a sample preparation, 0.5-1 g powder sample was put into a plastic sample holder sealed with a film prior to X-ray irradiation. A Si(Li) detector was used to integrate characteristic X-ray signals. Each sample was applied with 50 kV voltage for 100 seconds to guarantee a quantitative analysis with high accuracy.

2.2.2 X-ray photoelectron spectroscopy (XPS)

In contrast to the bulk-sensitive quantitative technique by EDX, the X-ray photoelectron spectroscopy (XPS) is a surface-sensitive technique. In addition to quantitative analysis on the surface, the XPS spectra also indicate electronic state and chemical states of the elements.[3] Measuring the number and kinetic energy of photoelectrons make the surface analysis possible in a range of 0-10 nm from the top of the surface. The combined use of EDX and XPS allows selective quantitative analysis in bulk and on surface of a sample.

Irradiation of X-rays with sufficient energy can excite an electron from a specific electron shell to become a photoelectron. At ultrahigh vacuum conditions, the kinetic energy of the ejected photoelectron is measured by an electron analyzer. The binding energy of an electron in a particular element can be calculated as follow:

$$E_{binding} = E_{photon} - E_{kinetic}$$

Where E_{photon} represents the enemy of the X-ray photons being irradiated. The XPS equipment (Ulvac-Phi, PHI X-tool) used in this study applied Al-K_{α} emission (E_{photon} = 1486.7 eV) as the X-rays source. Since the binding environment of an element is decided by its oxidation state, the chemical state of the element is inferred to a chemical shift of the binding energy.

The capability of surface analysis depends on the reduction of photoelectron number during escaping from the sample into the vacuum. Charged photoelectrons undergo inelastic collisions when traveling through the sample. Hence, the alive photoelectrons being able to reach the detector are mainly from the surface of the sample.

Under continuous X-ray irradiation, escaping of electrons leads the sample to be positively charged, usually named as a charge-up effect. It makes the correct identification of the chemical state difficult. To exclude charge-up effect, each powder sample with little amount was put on an iridium (Ir) foil before X-ray irradiation. Escaped electrons from the sample are compensated from the Ir foil. Fine amount of sample realizes smooth electron transferring from the Ir foil to the sample. Signal accuracy was obtained by increasing accumulation count.

2.2.3 X-ray diffraction (XRD)

X-ray crystallography (XRD) is a common technique to detect crystallographic structure.[4] Most of the photocatalyst materials can be described as crystalline. Hence the XRD is usually applied to determine the crystal structure of photocatalysts for checking purity. In this study, the author used the XRD to confirm presence and absence of impurity phase, change in lattice volume by doping, and homogeneity of dopants.

Incident X-rays diffract by electron clouds of measured atoms. With diffraction angle gradually changing, the X-ray diffractions are captured with a detector for recognizing lattice distance in a particular lattice plane. In regularly arrayed atoms, such as a crystal, the X-ray diffractions produce a regular array of waves according to Bragg's law,

$$n\lambda = 2d \sin(\theta)$$

where n is a numeric constant, λ is the wavelength of the incident X-ray, d represents the distance between lattice planes, and θ is the angle of incident X-ray. By fixing incident X-ray, the lattice distance (d) can be calculated from the incident angle (θ).

Since the photocatalyst materials used in this study are powder, a powder X-ray diffractometer (Rigaku, SmartLab) was applied. Cu-Kα emission is used as an X-ray source to scatter on powder sample with the incident angle (θ) in a range of 5-40°. In powder X-ray diffraction, the diffraction patterns referring to all lattice planes are presented. Thus the lattice constant of the measured sample can be calculated based on the X-ray diffraction patterns.

Before XRD measurement, each powder sample was ground well with agate mortar until to obtain a soft powder. Then the sample was deposited on a glass sample holder with hollow space as deep as 5 mm.

2.2.4 Scanning electron microscopy (SEM)

Scanning electron microscopy (SEM) is a type of microscopy, which uses a focused beam of electrons to scan the surface of a sample for creating an image. The SEM is one of the widely used techniques to observe particle size and morphology of photocatalyst materials.[5] It was also applied in this study to confirm the change in particle size and shape caused by dopants in Sr-doped $NaTaO_3$ photocatalysts. The actual measurements were performed by Dr. Yohan Park (Univ. Tokyo) and Dr. Hidenori Saito (KAST).

To obtain SEM images with high quality, a field-emission (FE) SEM (Hitachi High-Technologies, S-4800) was employed. Electrons are emitted from an FE source and accelerated in an electrical field to be used as primary electrons. In a high vacuum, these primary electrons interact with the sample to produce secondary electrons through inelastic scattering. The scattered electrons can survive only a few nanometers from the surface due to their low energy and the electric charge. A detector can not collect the secondary electrons from bulk since they lose their energies during moving out. With this surface sensitivity, the surface morphology and particle size can be clearly measured and presented in an image.

2.2.5 Ultraviolet-visible spectroscopy (UV-Vis)

In this study, a ultraviolet-visible spectroscopy (UV-Vis) was applied to determine the change in band gap energy of $NaTaO_3$ by Sr doping. The UV-Vis is an absorption spectroscopy in the ultraviolet-visible spectral region.[6] The ultraviolet or visible radiation refers to the excitation of outer electrons. When an atom or molecule absorbs photon energy, electrons transit from a ground state to an excited state. In the case of Sr-doped $NaTaO_3$ photocatalyst, the electron transition from a valence band to a conduction band causes a UV-Vis absorption corresponding to the band gap energy. The wavelength of the absorption light can be calculated by the following equation:

$$E_g = hc / \lambda$$

where E_g is a band gap energy, h is the Planck constant, c is the speed of light in vacuum, and λ is the wavelength of the photon. Since the h and c are both constants, the equation can be simplified as:

$$E_g\ (eV) = 1240 / \lambda\ (nm)$$

The calculated wavelength of absorbed light is usually in the range of ultraviolet and visible because the photocatalyst materials are semiconductors, which have limited band gap energy. Thus the band gap energy of Sr-doped $NaTaO_3$ can be measured by UV-Vis.

Since the Sr-doped $NaTaO_3$ (powder semiconductor) has little insolubility in any solvent, the transmission method usually used in UV-Vis is not proper in this study. Instead, a diffuse reflection method was applied. Most of the light in diffuse reflection is contributed by scattering beneath the surface of powders. The scattered light is collected with an integration sphere. The incident light is gradually scattered from 200 to 800 nm for detecting band gap energy of Sr-doped $NaTaO_3$.

2.2.6 Raman spectroscopy

Raman spectroscopy was used to determine presence or absence of B-site doping in Sr-doped $NaTaO_3$. As a spectroscopic technique, Raman spectroscopy is usually used to achieve information on rotational and vibrational levels in a material. Upon irradiation with a laser beam, a sample produces electromagnetic radiations by two different scattering, elastic and inelastic. In the elastically scattered radiation (Rayleigh scattering), the scattered photon has the same energy as the input photon. In a comparison, the scattered photon has either lower (Stokes scattering) or higher (Anti-Stokes scattering) energy than the incident photon. The energy shifted due to the difference between the initial and final vibrational or rotational state. By defining the Raman shift of $NaTaO_3$ before and after doping with Sr, the Sr doping site can be observed.

In the earlier study about Raman scattering on $Ba(Mg_{1/3}Ta_{2/3})O_3$,[7] which is a perovskite-structured material with Ta at B-sites were partially substituted with Mg, the vibration of an oxygen octahedron around a Ta at B-site was observed at 800 cm^{-1} with a high intensity. Similar BO_6 breathing vibrations were also detected in $Ba(Y_{1/2}Ta_{1/2})O_3$,[8] $Sr(Al_{1/2}Ta_{1/2})O_3$, and $Sr(Al_{1/2}Nb_{1/2})O_3$,[9] in a range of 750-900 cm^{-1}. In this study, the author applied the characteristic Raman signal of B-site doping in perovskite structure to verify doping site of Sr in $NaTaO_3$.

For a personal convenience, the author used two different types of equipments to observe Raman scattering. One is a fabricated Raman spectrometer, which has a He-Cd laser light source (Kimmon, IK4401R-D) with a wavelength of excitation light at 442 nm, grating spectrometer (Horiba Jobin Yvon, iHR320), and charge-coupled device detector (Andor, DU440BU). The other one is a Raman spectrometer (Jasco, NRS-7100) using laser light with an excitation wavelength of 532 nm. Raman scattering at both excitation wavelengths enabled bulk-sensitive characterization, as Sr-NTO is optically transparent at wavelengths longer than 320 nm. Chapter 3-5 uses the former equipment, and chapter 6 uses the latter one.

2.2.7 *Infrared spectroscopy (IR spectroscopy)*

Infrared (IR) spectroscopy is a commonly used technique to identify chemicals.[10] Photons associated with infrared do not possess sufficient energy to excite electrons, unlike the ultraviolet or the visible photons usually do. But the infrared photons may induce vibrational or rotational excitation of covalently bonded atoms, which can stretch and bend. Compared to the Raman spectroscopy can detect a vibration that causes a change in polarizability, the IR spectroscopy is specialized to a vibration causes a change in dipole moment.

In molecular vibrations, a stretching frequency of a bond can be calculated as follows:

$$\nu = \frac{1}{2\pi c}\sqrt{\frac{k}{\mu}}$$

where c is the speed of light in vacuum, k is the spring constant for the bond, and μ is the reduced mass of the two atoms forming the bond.

One of the applications of the IR spectroscopy used in this study is to examine the presence or absence of water-species in Sr-doped $NaTaO_3$ prepared via hydrothermal method.

The other application is the measurement of the population of photo-excited electrons. Upon ultraviolet (UV) irradiation, the electrons at the valance band of Sr-doped $NaTaO_3$ are excited to the conduction band or being captured at trap levels with potential just beneath the conduction band. These UV-excited electrons can observe IR due to the intraband (conduction band) or interband (between conduction band and trap levels) transition. The absorbed IR energy represents for transition energy, while the absorbance represents a population of UV-excited electrons. This electron population indicates the rate of electron-hole recombination. Hence, the UV-induced IR absorption method helps to determine the change in electron-hole recombination rate of $NaTaO_3$ caused by Sr doping.

The transmission IR absorption was obtained with a Fourier-transform spectrometer (Jasco, FT/IR610) in the presence and the absence of UV light irradiation. A 200-W Hg–Xe lamp (San-ei Electric, UVS-204S) was used as the UV light source.

2.2.8 Scanning transmission electron microscopy (STEM)

Transmission electron microscopy (TEM) is a powerful technique to observe crystal structure and dislocations and grain boundaries in the structure. A high energy beam of electrons is transmitted through a thin sample to form a TEM image. A strength of TEM imaging is the very high resolution.

In this study, an EDX (FEI, Super-X) lined scanning transmission electron microscopy (STEM, FEI, TITAN^{TM}) was used to observe elemental mapping in Sr-doped $NaTaO_3$ prepared via MSM. The measurement was conducted by Dr. Mitsunori Kitta (AIST).

The STEM is a type of TEM that modified with a scanning coil. During electron transmission, the primary electron beam will also interact with the sample to produce secondary electrons and characteristic X-rays. Thus, one feature of STEM is the imaging of the secondary electrons scattered on surface of the sample in the same way as a standard SEM. The other feature is the high-angle annular dark-field (HAADF) imaging. By using a HAADF detector, the electrons scattered in a far more angles can be detected than a bright-field (BF) detector. In HAADF imaging, the contrast of an atomic column is directly related to the atomic number.[11]

When the STEM is lined with an EDX detector, the characteristic X-rays emitted from the sample can be collected to form an elemental mapping. To detect radial distribution of Sr in Sr-doped $NaTaO_3$ particles was the main purpose by using STEM-EDX.

2.2.9 X-ray absorption spectroscopy (XAS)

X-ray absorption fine structure (XAFS) of Sr was observed by X-ray absorption spectroscopy (XAS) in Sr-doped $NaTaO_3$ prepared via various methods. The X-ray source used in this study was synchrotron radiation (BL-12C in Photon Factory). Local structure of Sr is the main information the author wants to know from analyzing the XAFS.

An atom absorbs X-ray when the photon energy is large enough to ionize or excite electrons at the core level. The excited photoelectrons will scatter by neighboring atoms and return to the measuring atom. The X-ray absorption coefficient of the measuring atom is affected by the scattered photoelectrons to form an oscillation in the extended range after the X-ray absorption edge energy.

XAFS of Sr in Sr-doped $NaTaO_3$ photocatalysts was measured via transmission or fluorescence method depending on the small or large Sr concentration. The absorption coefficient can be measured depending to the Beer's Law:

$$\text{Transmission method :} \quad \mu(E) = \log(I_0/I)$$

$$\text{Fluorescence method :} \quad \mu(E) \propto I_f/I_0$$

where $\mu(E)$ is the absorption coefficient, I_0 is the incident X-ray intensity, I is the X-ray intensity transmitted through the sample, I_f is the fluorescence X-ray intensity.

Based on the comparison between the photoelectron wavelength and the interatomic distance, the XAFS interpretation is usually divided into two energy regions, that is; X-ray absorption near edge structure (XANES) and extended X-ray absorption fine structure (EXAFS), respectively.[12]

The XANES region ranges a 50-100 eV after the X-ray absorption edge energy. In this regime, the wavelength of the photoelectrons is larger than an interatomic distance. Thus the XANES region is decided by multiple scattering resonances. Key information can be achieved from XANES interpretation are the chemical state of the measuring atom and the size of the atomic cluster of neighboring atoms.

The EXAFS region ranges a 100-1000 eV after the X-ray absorption edge energy. In this regime, a single scattering of the photoelectrons plays a key role to the X-ray absorption spectrum due to the shorter photoelectron wavelength than the interatomic distances. The scattered photoelectrons affect the EXAFS spectrum to be shown as an oscillation. Before analyzing the oscillation, the EXAFS function $\chi(E)$ is defined as:

$$\chi(E) = \frac{\mu(E) - \mu_0(E)}{\Delta\mu_0}$$

where $\mu_0(E)$ is a smooth background function representing the absorption of an isolated atom, $\Delta\mu_0(E)$ is the measured jump in the absorption coefficient at the absorption edge energy (E_0).

The EXAFS can be understood mostly easily in terms of wavenumber of the photoelectron (k), which is defined as:

$$k = \sqrt{\frac{2m(E - E_0)}{\hbar^2}}$$

where E is the incident X-ray energy, and m is the electron mass. EXAFS spectra shown in this thesis indicates the $\chi(k)$. $\chi(k)$ is multiplied with a power of k (k^2 or k^3) to emphasize the EXAFS oscillation. Each donation to EXAFS oscillations in $\chi(k)$ of different coordination shells can be described by Fourier transforming the EXAFS equation, which can be shown as:

$$\chi(k) = S_0^2 \Sigma_j \frac{N_j f_j(k) exp(-2k^2\sigma_j^2)}{kR_j^2} sin[2kR_j + \delta_j(k)]$$

where S_0^2 is amplitude of the oscillation affected by many-body effect, N is the number of neighboring atoms, σ^2 is the disorder in the neighbor distance, R is the distance to the neighboring atom, $f(k)$ and $\delta(k)$ are scattering properties of the neighboring atoms, and j is the number of the coordination shell where the neighboring atoms are located.

EXAFS interpretation offers information about the interatomic distance of the neighboring atom and the coordination of measuring atom to the neighbors.

2.3 REFERENCE

(1) Anthony R. West, “Solid State Chemistry and its Applications”. *Wiley.* **2005**.

(2) Ron Jenkins, “X-Ray Fluorescence Spectrometry”. *Wiley*. **1988**.

(3) 日本表面科学会, “X線光電子分光法”. 丸善. **1998**.

(4) 服部敏明・川口健・纐纈守・吉野明広, “機器分析ナビ”. 化学同人. **2006**.

(5) 日本表面科学会, “ナノテクノロジーのための走査電子顕微鏡”. 丸善. **2004**.

(6) 日本分光学会, “可視・紫外分光法”. 講談社. **2009**.

(7) Siny, I. G.; Tao, R.; Katiyar, R. S.; Guo, R.; Bhalla, A. S. *J. Phys. Chem. Solids* **1998**, *59*, 181-195.

(8) Gregora, I.; Petzelt, J.; Pokomy, J.; Vorlicek, V.; Zikmund, Z.; Zurmiihlen, R.; Setter, N. *Solid Stare Commun.***1995**, *94*, 899.

(9) Tao. R.; Guo, A.R.; Tu, C.S.; Siny, I.; Katiyar, R.S; Guo, R; Bhalla, A.S. *Ferroelectrics Lett.* **1996**, *21*, 79.

(10) 濱口宏夫・岩田耕一, “近赤外分光法”. 講談社. **1996**.

(11) Pennycook, S.J.; Jesson, D.E. *Ultramicroscopy* **1991**, *37*, 14.

(12) 日本分光学会, “X線・放射線の分光”. 講談社. **2009**.

Chapter 3

$NaTaO_3$ doped with Sr via SSM, HTM and STM

3.1 INTRODUCTION

To date, doping metals in host photocatalyst materials have increased quantum efficiencies for water splitting to high levels. Quantum efficiencies of La-doped $NaTaO_3$[1-2] and Zn-doped Ga_2O_3[3] are 56% at 270 nm and 20% at nm, respectively. These studies reveal the metal dopants played a key role in the efficient evolution of hydrogen fuel.

In $NaTaO_3$ photocatalysts, alkaline-earth metals Ca, Sr, or Ba used as dopant presented comparative quantum efficiency as La dopant.[4-5] Electron-hole recombination rate in metal-doped $NaTaO_3$ was studied using time-resolved infrared (TR-IR) absorption.[6-7] As a result, the electron-hole recombination of $NaTaO_3$ was restricted when doped with heterometals. Hence the quantum efficiency increased. However, the mechanism behind the restriction is still unknown. To make the mechanism clear is the primary mission to complete in this thesis.

When $NaTaO_3$ was doped with metals (Sr, Ba, or La), step structures were produced on surface of the photocatalyst particles.[1-2,4] Such a surface reconstruction should be related to structural change induced by metal dopants. Thus the author assumed the restricted recombination attributed to compositional and structural change caused by dopants. Here the perovskite structured $NaTaO_3$ is composed of Na^+ at A-sites, Ta^{5+} at B-sites, and O^{2-} at O-sites. It is necessary to know doping sites of the metals in $NaTaO_3$ for making clear the composition and structure of metal-doped $NaTaO_3$. This chapter mainly depicts the effect of Sr doping sites on electron-hole recombination.

Three different synthesis methods; solid-state method (SSM) and hydrothermal method (HTM), and solvothermal method (STM) were used to prepare Sr-doped $NaTaO_3$. By prepared Sr-doped $NaTaO_3$ photocatalysts were carefully characterized for determining structure and composition. In SSM, Sr substituted simultaneously Na^+ at A-sites and Ta^{5+} at B-sites. Consequently, the population of steady-state excited electrons was enhanced drastically, which means the electron-hole recombination was restricted. In HTM, Sr substituted Na^+ at A-sites alone, and the number of excited electrons did not change before and after doping. In STM, Sr was designed to replace Ta^{5+} at B-sites for determining effect of B-site doping on electron-hole recombination. As expected, the recombination was restricted.

3.2 EXPERIMENTAL SECTION

3.2.1 Synthesis

Sr-doped $NaTaO_3$ photocatalysts were prepared via three methods.

In the solid-state method (SSM), mixtures of Na_2CO_3, Ta_2O_5, and $SrCO_3$ were calcined in an alumina crucible at 1173 K for 1 h and then at 1423 K for 10 h, as the same way of previous studies.[4] The Na/Ta molar ratio in the mixtures was adjusted to 1.05, for compensating Na loss during calcination. Excess Na remaining in the product was washed with purified water.

In the hydrothermal method (HTM), 4 mol L^{-1} aqueous solution of NaOH containing Ta_2O_5 and $SrCO_3$ were well stirred and sealed in a Teflon container. The mixture was heated at 433 K for 24 h in an autoclave, referring to the earlier study.[8] The starting solutions had a Na/Ta molar ratio of 4. The product was centrifuged with purified water until the pH was maintained at 7.

In the solvothermal method (STM), $Sr(OC_3H_7)_2$ and $Ta(OC_2H_5)_5$ were used as suppliers of Sr^{2+} and Ta^{5+}, referring to STM synthesis of $NaTaO_3$.[9] Those metal-alkoxides in liquid were well blended with 3 ml ethanol solvent to form a solution include both Sr^{2+} and Ta^{5+}. The solution was then dripped into Teflon jar containing 10 ml aqueous solution of NaOH (6 mol L^{-1}) under stirring and cooling with ice water. During dripping, a suspension will be formed due to hydrolysis reaction of alkoxide with water. After stirring for 10 mins, the suspension was heated at 473 K for 24 h in an autoclave. The product was centrifuged with purified water until the pH maintained at 7.

Slow dripping and enough cooling are key points for an adequate synthesis.

Hereafter, a Sr-doped $NaTaO_3$ is referred to as Sr-NTO (SSM), Sr-NTO (HTM), or Sr-NTO (STM) when it was prepared through SSM, HTM, or STM, respectively.

3.2.2 Characterization

Concentrations of doped metals in bulk were quantified relative to the number of host Ta cations by EDX (Shimadzu, EDX-720). The crystallographic phase was determined by XRD (Rigaku, SmartLab). Raman scattering was detected with a fabricated Raman spectrometer, which has a He-Cd laser light source (Kimmon, IK4401R-D) with a wavelength of excitation light at 442 nm, grating spectrometer (Horiba Jobin Yvon, iHR320), and charge-coupled device detector (Andor, DU440BU). Band gap energy was obtained by UV-Vis diffuse-reflection spectroscopy (Jasco, V-570). Concentrations of doped metals on the surface were quantified relative to the number of host Ta cations by XPS (Ulvac-Phi, PHI X-tool). The size and shape of the photocatalyst particles were observed by SEM (Hitachi High-Technologies, S-4800). Infrared (IR) light absorption induced by ultraviolet (UV) light irradiation was observed to evaluate the steady-state population of photoexcited electrons that had not recombined in Sr-NTOs. The transmission IR absorption was obtained with a Fourier-transform spectrometer (Jasco, FT/IR610) in the presence and the absence of UV light irradiation. A 200-W Hg–Xe lamp (San-ei Electric, UVS-204S) was used as the UV light source.

3.3 RESULTS AND DISCUSSION

3.3.1 Doping site of Sr in Sr-NTO (SSM)

A series of Sr-NTOs with variable Sr/Ta molar ratio were prepared via SSM. Input Sr concentrations at starting materials were 0, 0.1, 0.3, 0.5, 1, 2, 5, 8, 20, and 50 mol%. Sr concentrations in the Sr-NTO product were investigated by EDX.

Figure 3.1 shows EDX spectra of normalized Sr-Kα emission. Sr/Ta molar ratio was estimated from the intensity of the Sr-Kα emission relative to that of the Ta-Lα emission. Calculated Sr concentrations were 0.1, 0.3, 0.5, 1.0, 2.0, 5.1, 8.3, 20.8, and 49.0 mol%, that was well consistent with input Sr concentrations. Most of Sr left in the product after calcination. Hereafter, Sr-NTO with input Sr concentration of x mol% will be referred to as x%Sr-NTO. For example, Sr-NTO with Sr concentration of 1 mol% will be shown as 1%Sr-NTO.

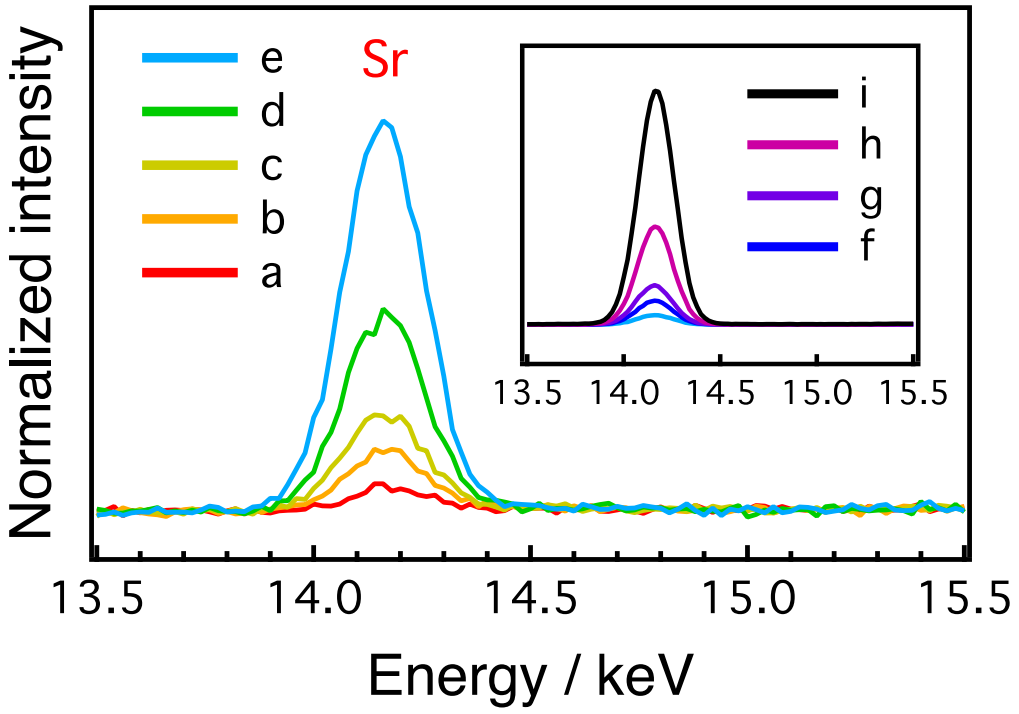

Figure 3.1 X-ray fluorescence spectra of Sr-Kα in Sr-NTOs (SSM) with input Sr/Ta molar ratio at a: 0.1%, b: 0.3%, c: 0.5%, d: 1%, e: 2%, f: 5%, g: 8%, h: 20%, i: 50%.

A single phase of perovskite structure of the photocatalysts was checked and confirmed by XRD. **Figure 3.2(A)** shows X-ray diffraction patterns in a range of 10-80° on NTO and Sr-NTO. NTO showed diffraction peaks referring to single perovskite structure of $NaTaO_3$, which were identical to those reported previously.[10] No impurity phase appeared even in 50%Sr-NTO. Diffraction peaks gradually shifted to lower angles with the increase of Sr concentration, while keeping the XRD patterns referring to perovskite structure. Detailed peak shift induced by Sr dopants is shown in **Fig. 3.2(B)**, which features 32° peaks having highest intensity. The low-angle shifts indicate perovskite lattice expansion upon doping.

To figure out the cause of lattice expansion by Sr doping, a perovskite-structured strontium tantalate, $Sr(Sr_{1/3}Ta_{2/3})O_3$, was synthesized via SSM and compared with Sr-NTOs (SSM). $Sr(Sr_{1/3}Ta_{2/3})O_3$, with already known structure,[11] has fully occupied A-sites and partially occupied B-sites with Sr^{2+} cations. In the present study, a mixture of $SrCO_3$, Ta_2O_5, and Na_2CO_3 was calcined in a manner of SSM. The Sr/Ta and Na/Ta molar ratios in the mixture were adjusted to 2 and 1, respectively. Sr/Ta molar ratio in the product was detected as 1.78 by EDX. $Sr(Sr_{1/3}Ta_{2/3})O_3$ (SSM) showed identical diffraction pattern to the reported one.[11] XRD peaks of NTO is absent, even though the starting material included Na_2CO_3. When a mixture of only $SrCO_3$ and Ta_2O_5 was calcined, complex oxides as impurity phases were detected in addition to $Sr(Sr_{1/3}Ta_{2/3})O_3$. Sodium in the starting material provided nucleation centers for the perovskite framework that is in favor for the growth of the single phase of $Sr(Sr_{1/3}Ta_{2/3})O_3$. Thus, $NaTaO_3$ may have been formed and then converted into $Sr(Sr_{1/3}Ta_{2/3})O_3$.

The diffraction patterns of $Sr(Sr_{1/3}Ta_{2/3})O_3$ and Sr-NTO were qualitatively identical, both attributed to perovskite structure. Each diffraction peak of Sr-NTO (SSM) shifted to lower angles to approach the corresponding peak of $Sr(Sr_{1/3}Ta_{2/3})O_3$ as the Sr concentration increased. The continuous shifts suggest solid solutions between $NaTaO_3$ and $Sr(Sr_{1/3}Ta_{2/3})O_3$ were formed in Sr-NTO (SSM). Considering Sr^{2+} cation has different electrical charge number compared to Na^+ and Ta^{5+} cations in $NaTaO_3$, to form a solid solution is the easiest way to maintain the balance of cationic and anionic charges in Sr-$NaTaO_3$ without producing vacancies of cations or anions. The low-angle shifts are consistent with doping Ta^{5+} with Sr^{2+} that was required in the solid solutions. The ionic radii of 6-fold-coordinated Ta^{5+} and Sr^{2+} are

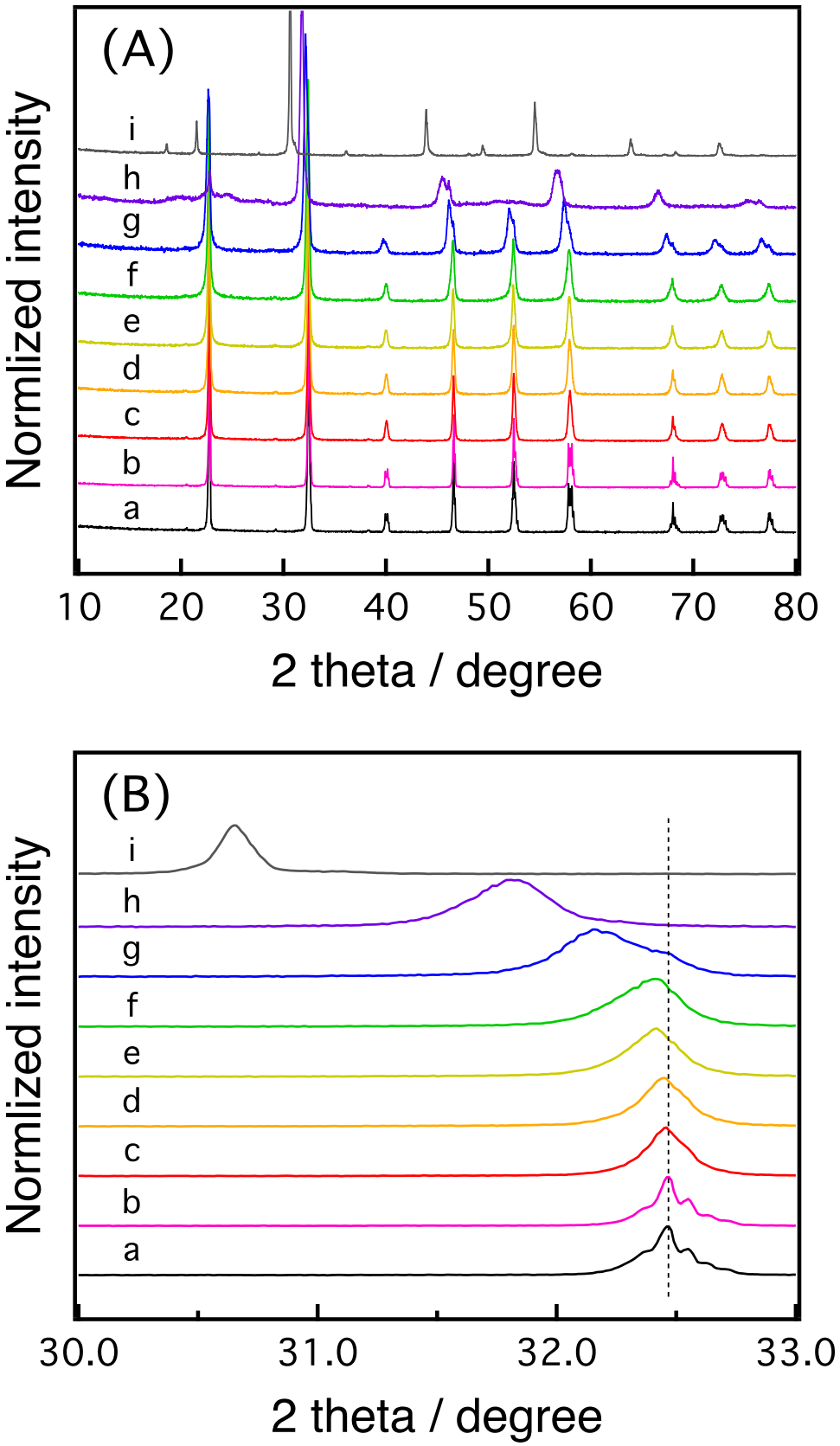

Figure 3.2 XRD patterns of a: NTO, b: 0.1%Sr-NTO, c: 1%Sr-NTO, d: 2%Sr-NTO, e: 5%Sr-NTO, f: 8%Sr-NTO, g: 20%Sr-NTO, h: 50%Sr-NTO, and i: $Sr(Sr_{1/3}Ta_{2/3})O_3$. (A) 10-80°, (B) 30-33°.

0.06 and 0.12 nm, respectively.[12] On the other hand, the ionic radii of 12-fold-coordinated Na^{+} and Sr^{2+} are both 0.14 nm. Therefore, the lattice expansion should be contributed mainly from B-site doping of Sr.

The lattice volume of Sr-NTO (SSM) was calculated from the diffraction results, as shown in **Fig. 3.2(C)**, to find evidence for the proposed solid solutions. The lattice volume is plotted as a function of the Sr/Ta molar ratio. As a result, a straight line is fitted to the observed volumes in the full range from $NaTaO_3$ to $Sr(Sr_{1/3}Ta_{2/3})O_3$. The linear relation between lattice volume and Sr concentration supports the presence of the solid solutions.

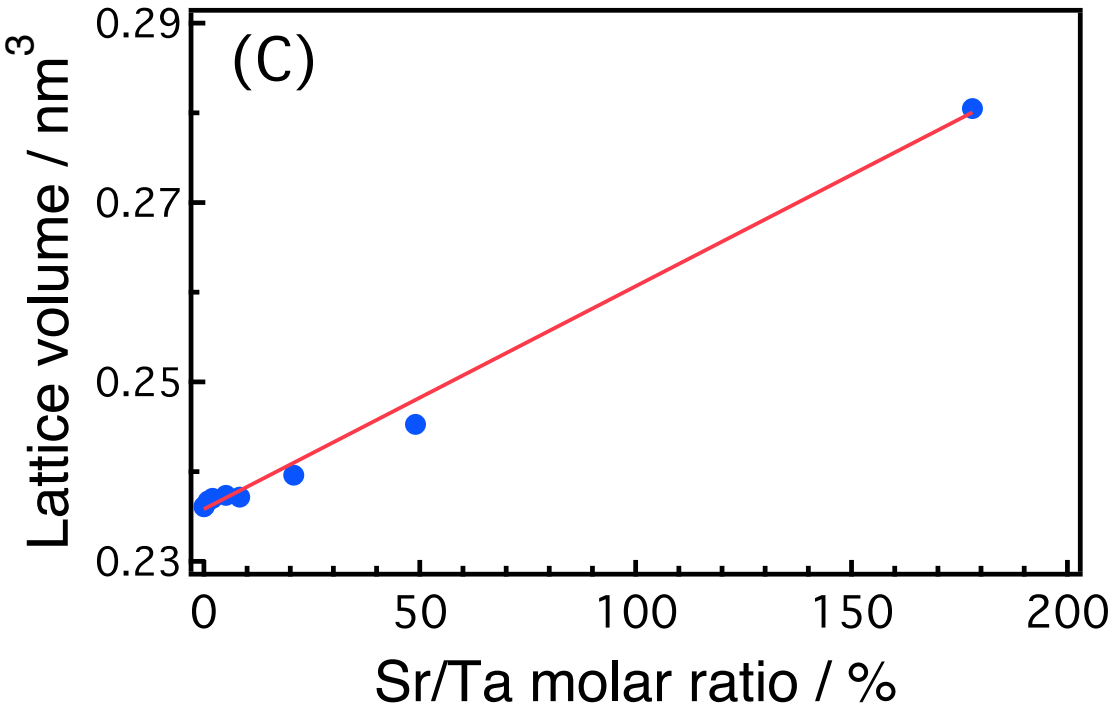

Figure 3.2 (C) Lattice volume of Sr-NTOs plotted as a function of Sr concentration. Lattice volume was calculated based on XRD patterns presented in panel (A).

However, in earlier studies,[4-7,13-14] simple A-site doping was assumed in Sr-doped $NaTaO_3$, due to similar ionic radii of Sr and Na with 12-fold coordination: 0.14 (Sr^{2+}) and 0.14 nm (Na^{+}). In the proposed picture of solid solutions between $NaTaO_3$ and $Sr(Sr_{1/3}Ta_{2/3})O_3$, simultaneous substitution of A- and B-sites in $NaTaO_3$ should be fulfilled. Additional evidence for the B-site doping in Sr-NTO (SSM) was obtained by Raman spectroscopy.

Figure 3.3(A,B) show Raman spectra of Sr-NTO (SSM). In NTO (SSM), major Raman bands appeared at 450, 500, and 620 cm^{-1}, similar to results reported in the earlier study.[15] Sr doping produced additional bands at 860 and 760 cm^{-1}. These bands are assigned to breathing vibrations of BO_6 octahedra in B-site substituted perovskite, $A(B_{1-x}B'_x)O_3$. The BO_6 breathing mode, which possesses A_{1g} symmetry, can not contribute to Raman scattering in an ideal cubic perovskite ABO_3 due to symmetry restriction. Partial substitution of B-site cations with hetero-cations (B') breaks down the restriction. Numerous studies had found strong Raman bands produced in a range of 750-900 cm^{-1} when ABO_3 perovskites were partially doped with B'.[16-18] Indeed, $Sr(Sr_{1/3}Ta_{2/3})O_3$ prepared via SSM produced an intense band at 810 cm^{-1}. The 860 cm^{-1} band of Sr-NTO strengthened with Sr concentration and merged with the 810 cm^{-1} band in $Sr(Sr_{1/3}Ta_{2/3})O_3$. The Raman band at 860 cm^{-1} is, therefore, an indication of B-site doping in Sr-NTO (SSM).

Since the 860 cm^{-1} band is sharp and well separated from the main bands that assigned to pristine NTO, quantitative detection of B-site doping is thus possible by comparing the intensity of the 860 cm^{-1} band. The intensity relative to that of the 620 cm^{-1} band is plotted in **Fig. 3.3(C)**, as a function of Sr concentration. The relative intensity of the 860 cm^{-1} band increased consistently with Sr concentration. The linear relation of them suggests amount ratio of Sr doped at B-sites/A-sites is almost constant in Sr-NTO (SSM), which supports the proposed model of the solid solutions.

According to above assumption, Sr doped at A-sites should not contribute to additional Raman bands. To verify the effect of A-sites doping, the author prepared K-doped $NaTaO_3$ with K concentration of 3.0 mol%. Previous studies reported the K cations occupied the A-sites.[19-21] By keeping the balance of electric charge after doping, it is easy to understand K^+ cations prefer substituting Na^+ at A-sites to Ta^{5+} at B-sites. **Fig. 3.3(D)** shows Raman spectra of K-NTO in addition to undoped NTO. The absence of extra in K-NTO indicates K cations occupy only the A-sites of NTO, as expected. Thus, 860 cm^{-1} Raman band indicate B-site doping.

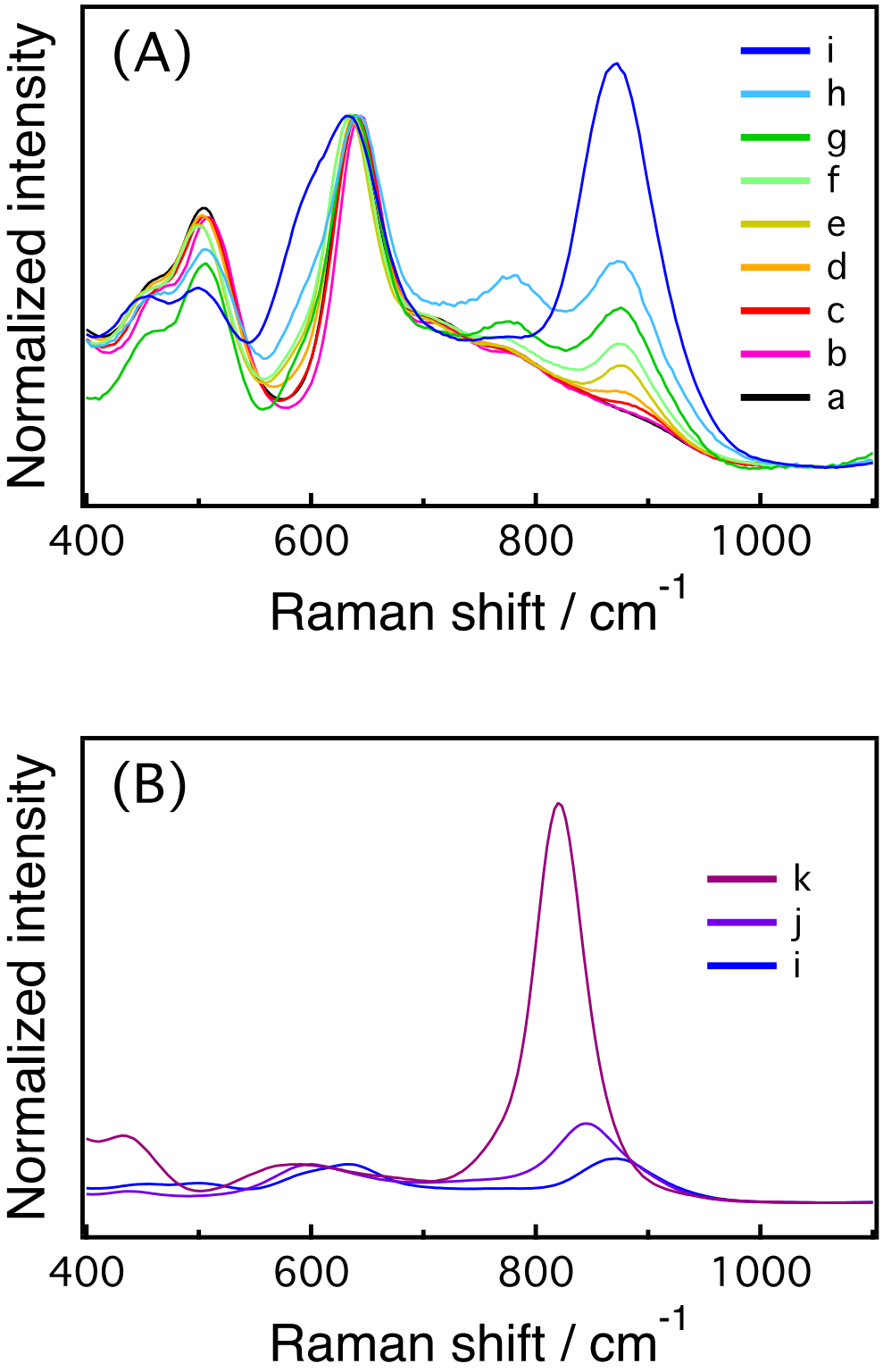

Figure 3.3 (A, B) Raman spectra of a: NTO, b: 0.1%Sr-NTO, c: 0.3%Sr-NTO, d: 0.5%Sr-NTO, e: 1%Sr-NTO, f: 2%Sr-NTO, g: 5%Sr-NTO, h: 8%Sr-NTO, i: 20%Sr-NTO, j: 50%Sr-NTO, and k: $Sr(Sr_{1/3}Ta_{2/3})O_3$.

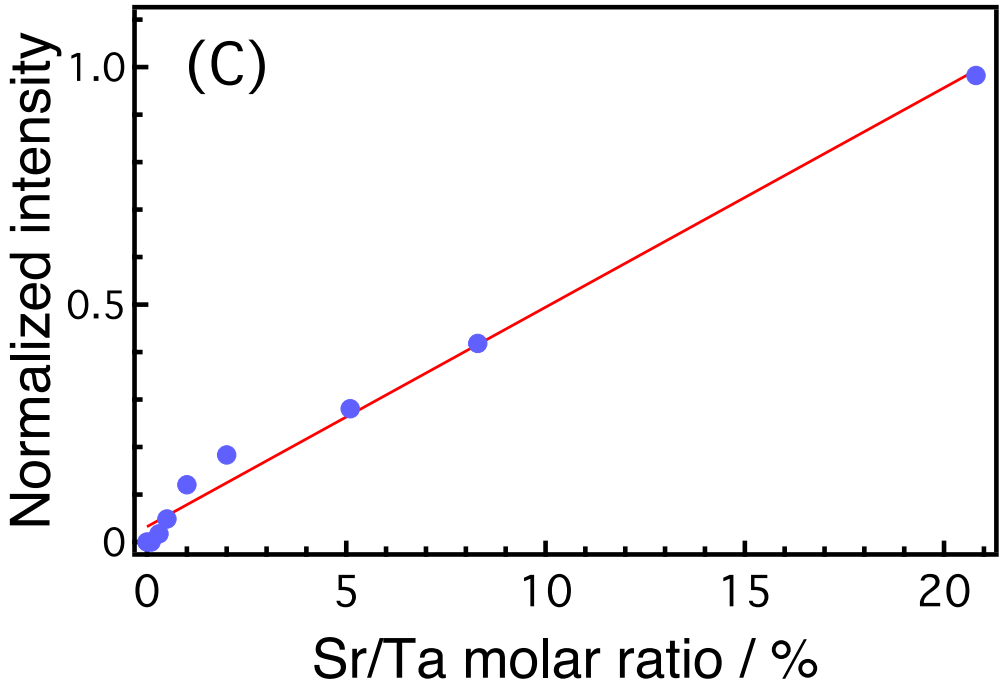

Figure 3.3 (C) Relative intensity of the 860 cm^{-1} band of Sr-NTO as a function of Sr concentration in a range of 0-20 mol%.

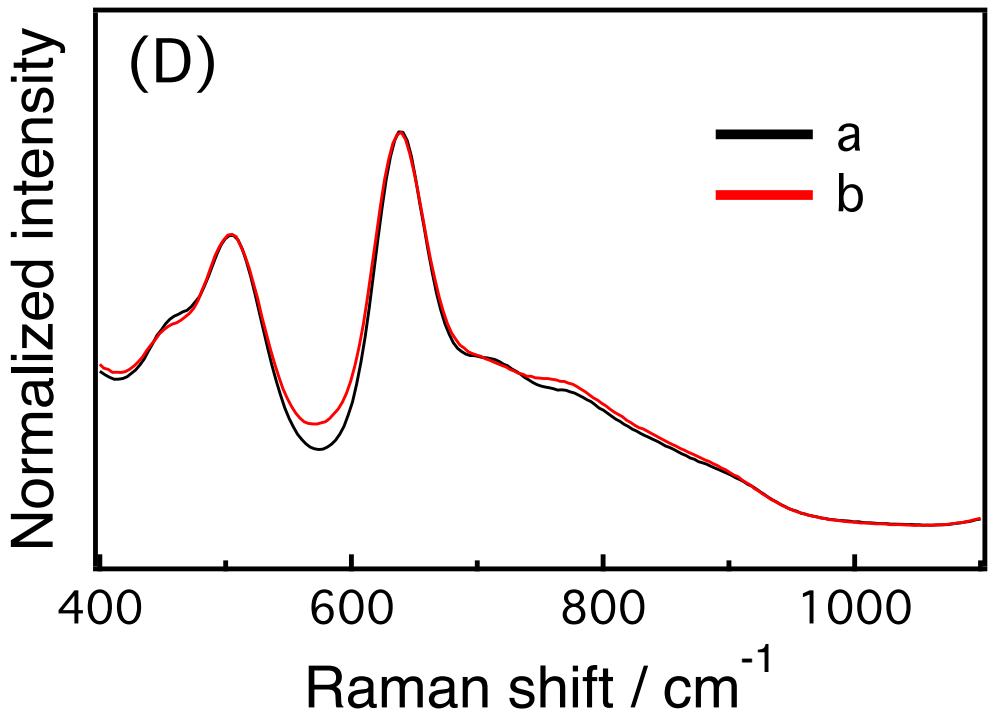

Figure 3.3 (D) Raman spectra of a: NTO (SSM) and b: 3%K-NTO (SSM).

B-site doping of Sr should also affect electronic structure of Sr-NTO (SSM), since the conduction band of NTO is mainly derived from Ta 5d orbitals.[22-24] UV-Vis diffuse-reflection spectra of Sr-NTO (SSM) are shown in **Fig. 3.4**. The central wavelength of the absorption edge of NTO (SSM) was at 305 nm. The edge gradually shifted to shorter wavelength upon doping of Sr at in a range from 0.5 mol% to 20 mol%. It shifted to 280 nm upon excessive doping at 50 mol% and $Sr(Sr_{1/3}Ta_{2/3})O_3$ displayed an edge at an even shorter wavelength. The continuous shift of absorption edge supplied additional evidence to the presence of the $NaTaO_3$-$Sr(Sr_{1/3}Ta_{2/3})O_3$ solid solution and B-site doping of Sr.

One issue to consider here is the confined shift of absorption edge induced by Sr doped at in a range of 0.5-20 mol%. With the increase of Sr concentration till 20 mol%, XRD (110) peak referring to NTO was present, as shown in **Fig. 3.2(B)**, despite the diffraction peaks gradually shifted to a lower angle. Since NTO absorb UV-Vis in a higher wavelength than Sr-NTO, the absorption attributing to Sr-NTO was thus covered by that of NTO. Absence of XRD (110) peak referring to NTO on 50%Sr-NTO and $Sr(Sr_{1/3}Ta_{2/3})O_3$, suggest the Sr cations distributed evenly in the $NaTaO_3$ particles. Therefore, an apparent shift was observed in UV-Vis absorption.

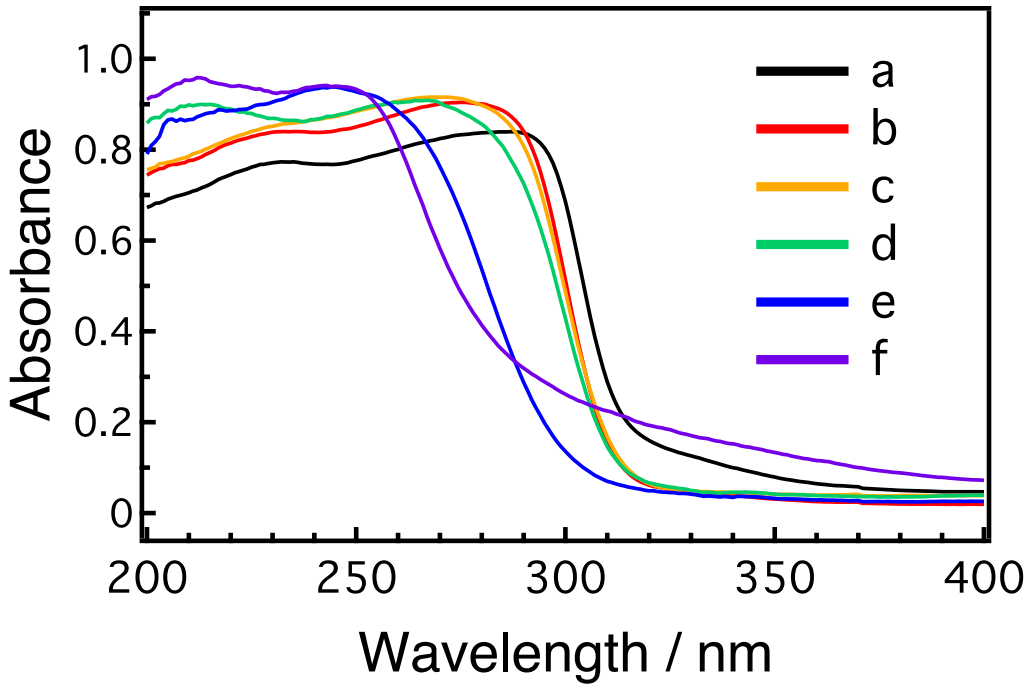

Figure 3.4 UV-vis diffuse-reflection spectra of a: NTO, b: 0.5%Sr-NTO, c: 5%Sr-NTO, d: 20%Sr-NTO, e: 50%Sr-NTO, and f: $Sr(Sr_{1/3}Ta_{2/3})O_3$.

The possible reason of the band gap energy expansion by Sr doping may be attributed to the defect of Ta. Based on the theoretical study,[22] contribution of Ta 5d orbitals to conduction band weekend when the Ta vacancy was considered. Sr doped at B-sites of $NaTaO_3$ in this study will cut the connection of the Ta 5d orbitals, consequently, the conduction band minimum is shifted upward. Meanwhile, the valence band maximum (O 2p) does not change.

Doping site of Sr in $NaTaO_3$ was investigated so far, and simultaneous substitution at A- and B-sites was the case in Sr-NTO prepared by SSM. It led solid solution between $NaTaO_3$ and $Sr(Sr_{1/3}Ta_{2/3})O_3$ to form during synthesis. In XRD, diffraction peak broadening detected upon Sr doping indicates the possibility of inhomogeneous distribution of Sr in $NaTaO_3$. It was also supported by the limited shift of UV-Vis absorption edge detected with Sr less than 20 mol%. The surface Sr concentration was examined by XPS for checking the distribution of Sr.

Figure 3.5(A) represent the Ta-4f emission composed of doublet peaks attributed to 7/2 and 5/2 spin-orbit couplings, respectively. The binding energy of each spectrum was calibrated to the O-1s emission at 530.0 eV for the calibration. The binding energy of the 7/2 peak was 25.6 eV, which is consistent with the energy reported for $Sr_2Ta_2O_7$, that explains the Ta cations have 5+ oxidation state.[25] The spectrum of NTO (SSM) presents peak broadening, possibly because of the charging induced by X-ray irradiation on semiconductor particles.

The Sr-3d emission of Sr-NTO (SSM) is shown in **Fig. 3.5(B)** as double peaks of 5/2 and 3/2 spin-orbit couplings. The binding energy of the 5/2 peak was 132.6 eV, which is consistent with the 2+ oxidation state of Sr cations.[25]

The surface concentration of Sr relative to Ta was estimated from the emission intensity ratio of Sr-3d versus Ta-4f. Since the kinetic energies of photoelectrons on Sr-3d and Ta-4f were 1.3 and 1.4 keV,[26] which were nearly equal, the common escape depth of electrons was assumed to be 2.4 nm. The estimated surface concentration was plotted as a function of the bulk Sr concentration determined via EDX, as shown in **Fig. 3.5(C)**. The Sr concentration on surface rapidly increased up to 10 mol% with a bulk concentration at 2 mol%, suggesting Sr segregation on the surface. Bulk concentration larger than 2 mol% reduced the slope of the surface/bulk concentration relation to near unity. It indicates the surface segregation was saturated and the concentration in the subsurface region accessible by XPS responded to bulk concentration at a one/one ratio.

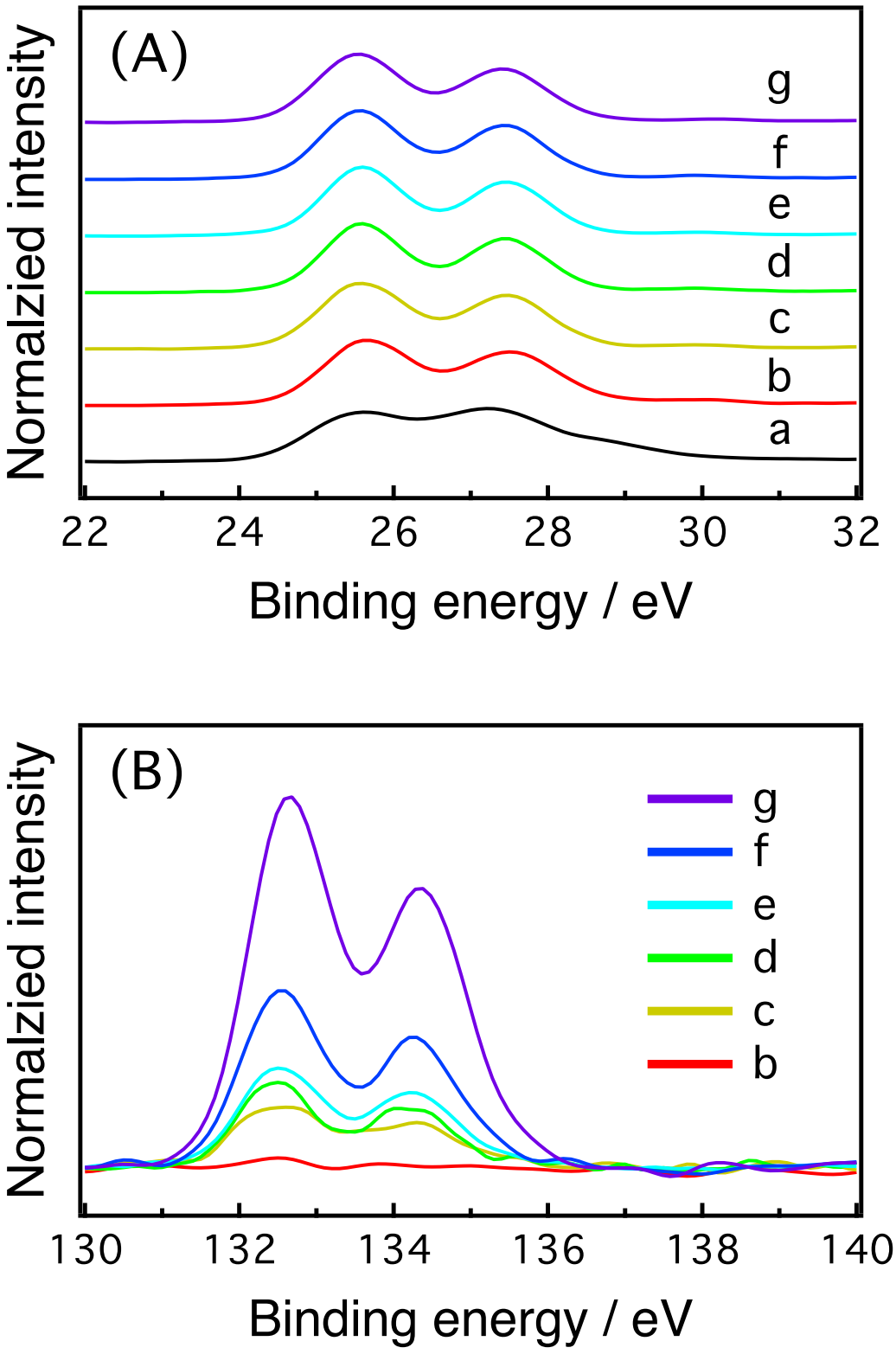

Figure 3.5 X-ray photoelectron spectra of a: NTO, b: 0.1%Sr-NTO, c: 0.5%Sr-NTO, d: 1%Sr-NTO, e: 2%Sr-NTO, f: 5%Sr-NTO, and g: 20%Sr-NTO. In (A) Ta-4f emission and (B) Sr-3d emission, the signal intensity was normalized relative to the Ta-4f level.

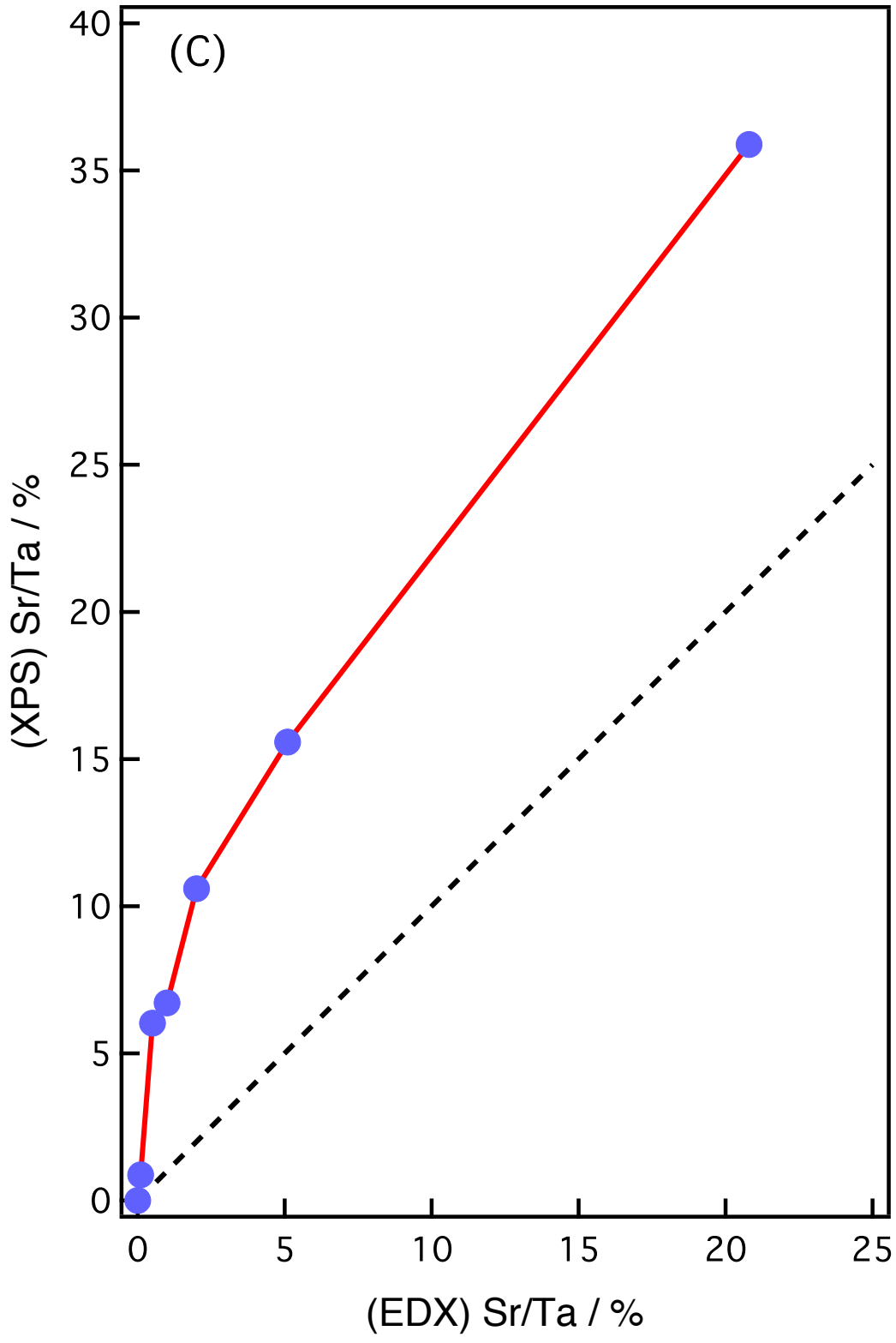

Figure 3.5 (C) The surface Sr concentration estimated from (B) is plotted as a function of the bulk Sr concentration determined from the EDX results. The broken line represents the relationship with a slope of unity.

The Sr segregation on the surface and the $NaTaO_3$-$Sr(Sr_{1/3}Ta_{2/3})O_3$ solid solution formed in Sr-NTO (SSM) also affected the shape of the photocatalyst particles. In the previous studies, [1,2,4] it was found that the size and morphology of $NaTaO_3$ photocatalyst particles were sensitive to the dopant concentration. In the present study, a similar relation between particle shape and Sr doping was found in Sr-NTO (SSM) by SEM, as shown in **Fig. 3.6**. Pristine NTO (SSM) particles were spherical cubes as large as 5 μm in diameter. Doping of Sr at 0.1 and 0.3 mol% reduced the particle size to 500 nm or smaller. The particle size was contracted to accommodate more Sr^{2+} cations on the surface. Simultaneous doping of Sr leads to a formation of $NaTaO_3$-$Sr(Sr_{1/3}Ta_{2/3})O_3$ solid solution. Due to the clear difference of lattice volume between the two materials, doping of Sr in bulk will induce lattice distortion. In nature to keep low energy, Sr tends to segregate on the surface. When Sr increased to in a range of 0.5-2 mol%, parts of Sr were doped into the bulk of the particles. In this case, the lattice mismatch was too strong to reserve in the shape of cubes. As a result, steps and terraces grew on the surface of the particles to release mismatch energy.

Combining the SEM observation with the previous characterization results, the author obtained a picture of Sr-NTO (SSM) in **Fig. 3.7**. Sr doping at less than 0.3 mol% reduced the particle size of NTO (SSM) from 5 μm to 500 nm. As illustrated in **Panel (A)**, the particle contraction attributed to Sr segregated on the surface. When Sr increased to 0.5 mol% or more, steps and terraces began to occur on the surface of the particles. To interpret the surface reconstruction, a core-shell structure was proposed, that is, a Sr-rich $NaTaO_3$-$Sr(Sr_{1/3}Ta_{2/3})O_3$ solid solution formed heteroepitaxially over a $NaTaO_3$ or Sr-poor solid solution core. The steps and terraces are generated to release lattice mismatch at the epitaxial interface, as shown in **Panel (B)**. It provides a simple explanation for the regulated steps.

In Sr-NTO (SSM) with Sr concentration at more than 0.5 mol%, excess Sr that is not able to be accommodated in the solid solution shell penetrated the bulk to produce a solid-solution core with a corresponding Sr concentration. Hence the 860 cm^{-1} Raman band and lattice volume increased proportionally to the particle-averaged Sr concentration detected by EDX. Upon Sr doping in a range of 0.5-2 mol%, the solid-solution shell included more Sr than the core. Therefore, the lattice mismatch was still present at the epitaxial interface, leaving the reconstruction on the surface. Meanwhile, the composition of the Sr-rich shell could not be

$Sr(Sr_{1/3}Ta_{2/3})O_3$ because the A_{1g} Raman band of Sr-NTO (SSM) appeared at 860 cm^{-1} , which is different from that of $Sr(Sr_{1/3}Ta_{2/3})O_3$ at 810 cm^{-1}.

Nanometer-sized steps and terraces on the surface were found in the solid solution of $NaTaO_3$ with $LaIrO_3$,[27] $LaCrO_3$,[28] and $LaFeO_3$[29] even though the mechanism of the reconstruction have not yet been proposed. Production of steps and terraces induced by lattice mismatch at the core-shell interface, which was proposed in Sr-NTO (SSM), can also be applied to those solid-solution photocatalysts for visible-light absorption.

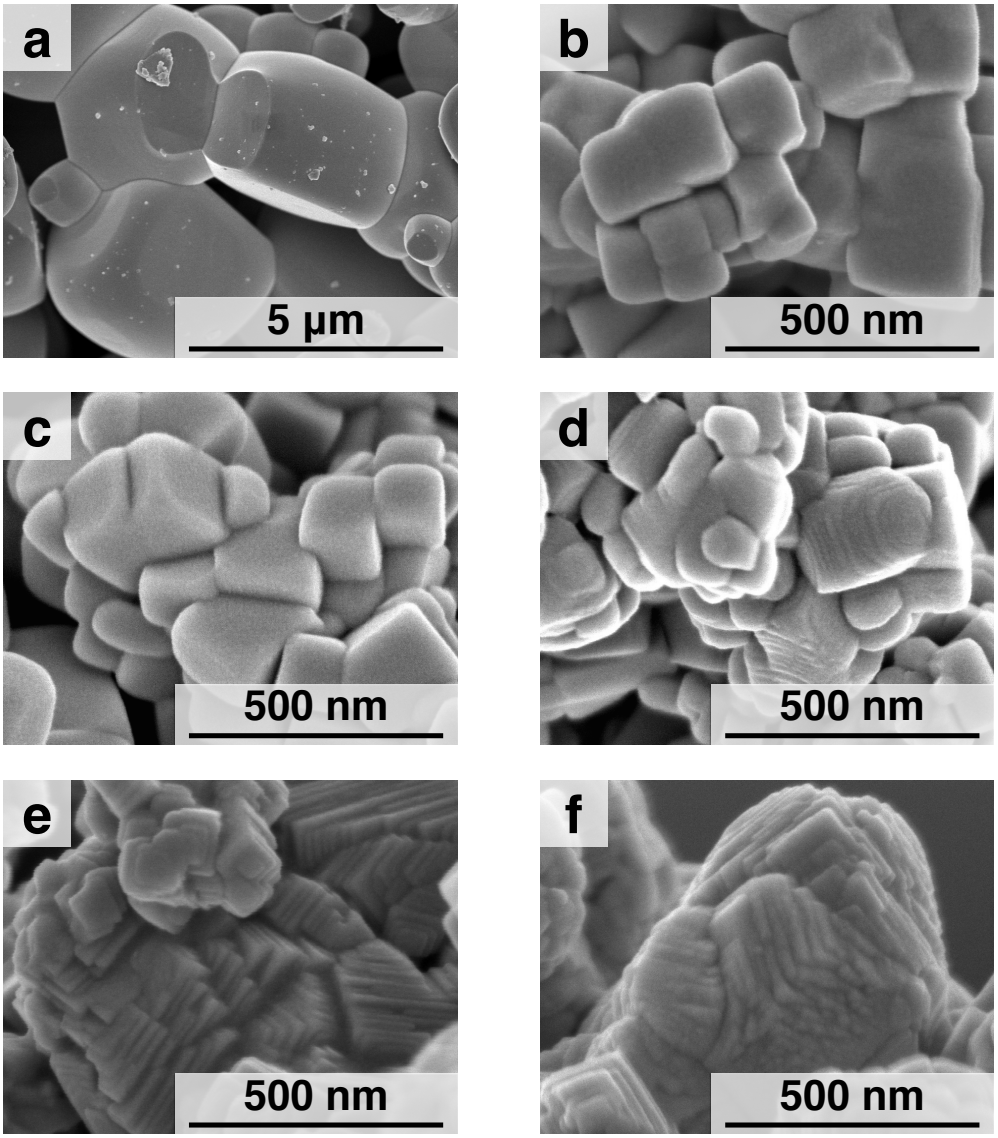

Figure 3.6 Scanning electron micrographs of a: NTO, b: 0.1%Sr-NTO, c: 0.3%Sr-NTO, d: 0.5%Sr-NTO, e: 1%Sr-NTO, and f: 2%Sr-NTO.

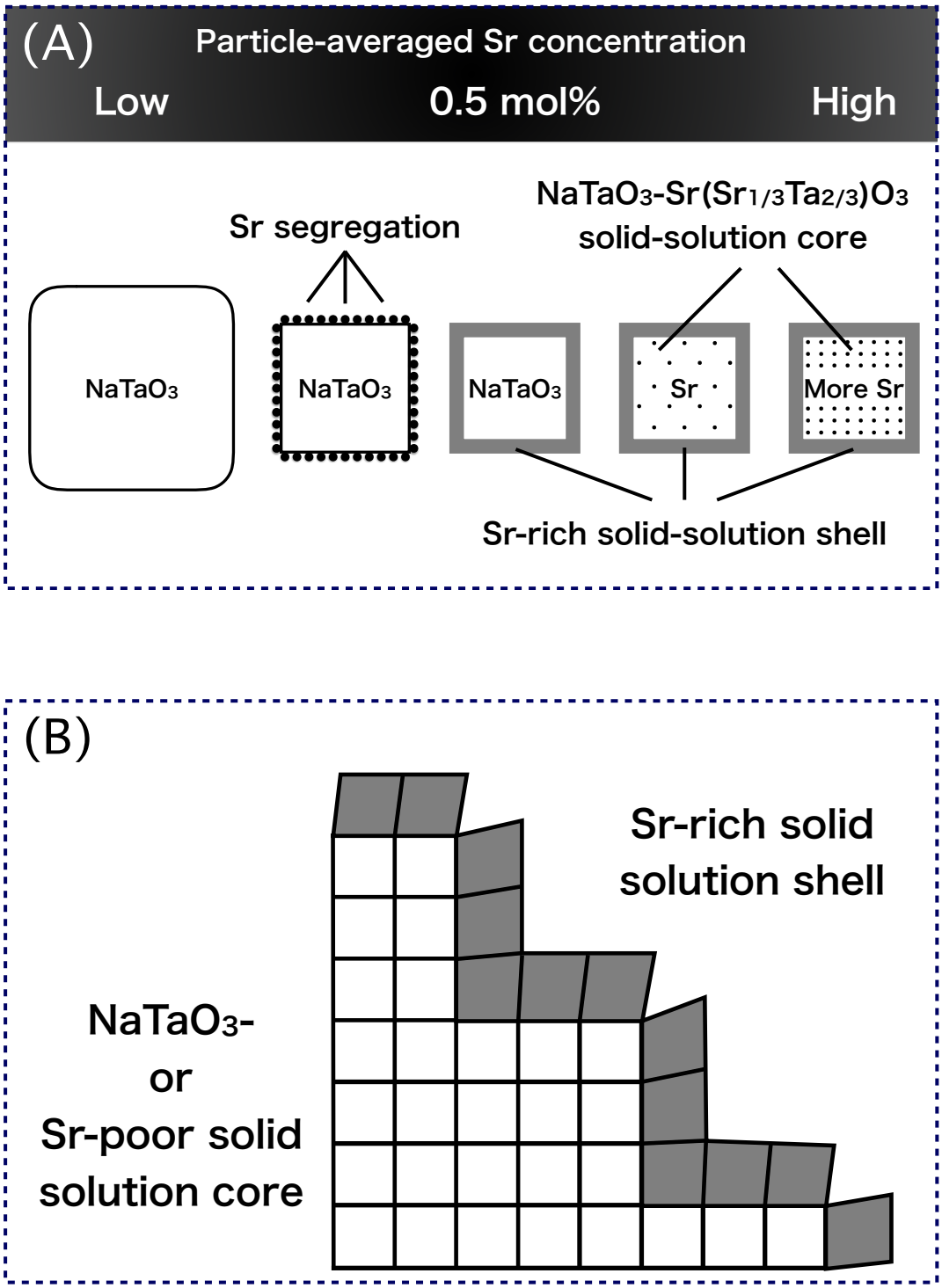

Figure 3.7 Schematic illustration of Sr-NTO structures with various Sr concentration. (A) Cross-sectional composition of particles. (B) Perovskite-structured lattices mismatched at the heteroepitaxial core-shell interface, generating regularly separated steps on the surface. White and gray squares represent unit cells in the core and shell, respectively.

Subsequently, electron-hole recombination in Sr-NTO (SSM) was examined by IR absorption spectroscopy to evaluate the effect of the $NaTaO_3$-$Sr(Sr_{1/3}Ta_{2/3})O_3$ solid solution. IR absorption induced by band gap excitation provides a quantitative measure of excited electrons that had not yet recombined. The change in IR absorbance of Sr-NTO (SSM) before and after UV irradiation are shown in **Fig. 3.8(A,B)**.

UV-induced IR absorbance change increased monotonically from 6000 to 820 cm^{-1}. Each photocatalyst was fixed on a CaF_2 plate and irradiated with the Hg-Xe lamp in a vacuum. Sharp edge at <900 cm-1 attributed to IR absorption of the CaF_2 plate. This monotonic IR absorption was assigned to band gap excited electrons observed in typical photocatalysts, including $NaTaO_3$,[6] $SrTiO_3$,[30] and TiO_2.[31-35] Intraband transitions of electrons in the CB, as well as electron transitions from shallow trap states to the CB, are the origins of the IR absorption. Hence, the steady IR absorption indicates a steady population of excited electrons in the photocatalysts upon UV irradiation. The IR absorbance change was enhanced significantly with Sr concentration. Strong absorbance changes mean a large electron population and, therefore, a restricted electron-hole recombination. Here the photocatalysts were irradiated with UV in a vacuum, that the excited electrons in the Sr-NTO (SSM) particles could not transfer to the environment.

Figure 3.8(C) shows the integrated absorbance change of Sr-NTO (SSM) in a range of 6000-900 cm^{-1}, normalized to that of NTO (SSM), plotted as a function of Sr concentration in Sr-NTOs. Taking into account the number of electrons in proportional to the integrated absorbance, electron population was enhanced by 180 times at maximum in Sr-NTO (SSM) doped at 2 mol% relative to that of NTO (SSM). It represents the solid solution of $NaTaO_3$-$Sr(Sr_{1/3}Ta_{2/3})O_3$ induced by simultaneous doping of Sr at A- and B-sites on NTO somehow restricted electron-hole recombination. Sr doped at B-sites was the new finding in this subsection. Study on the effect of Sr doping site on electron-hole recombination rate was continued.

One more issue to consider is the reduction of electron population with Sr doped at larger than 2 mol%. Doping of Sr with increased concentration did not have a consistent effect on the electron population. The reason was solved and will be presented in detail with following chapters.

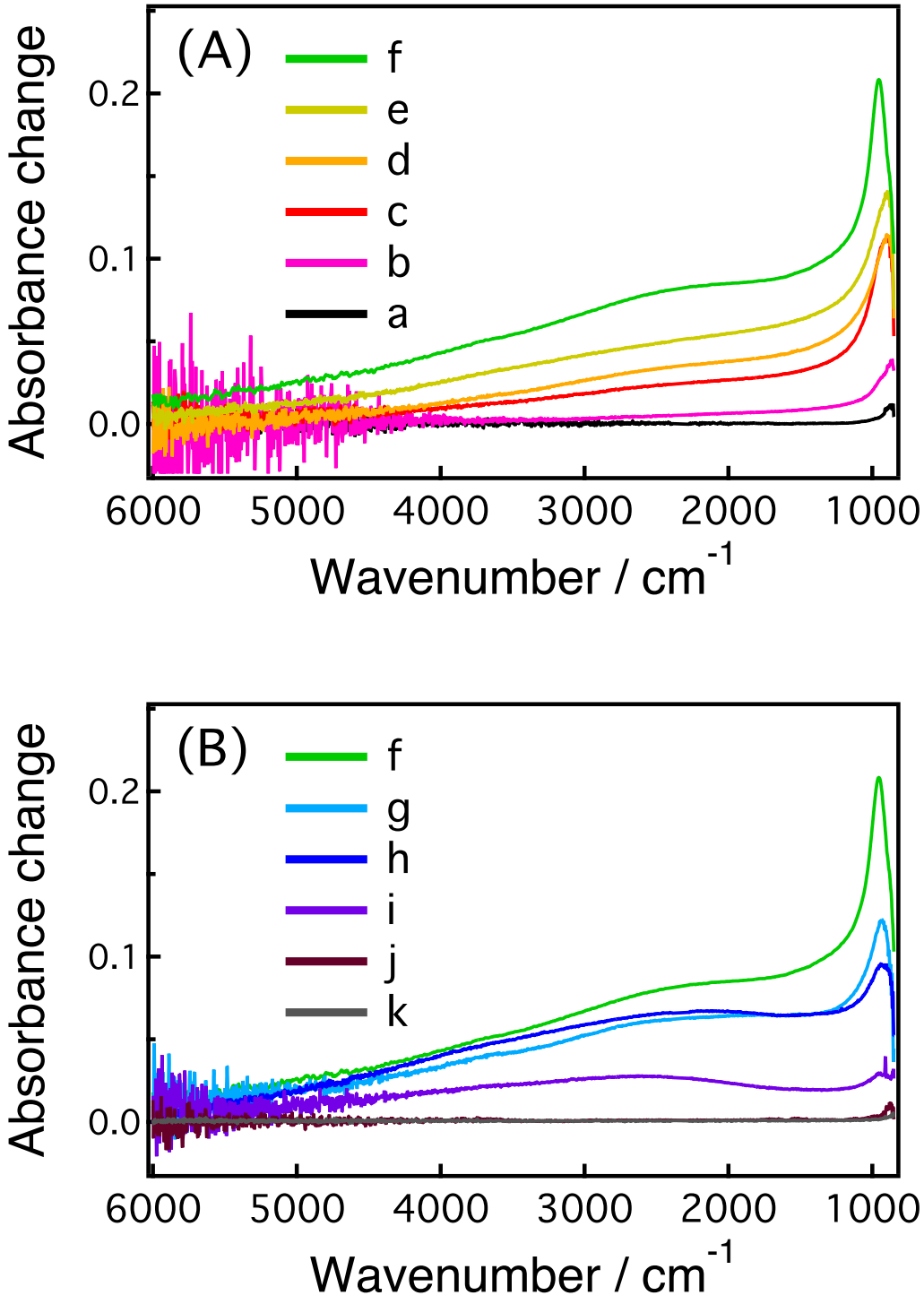

Figure 3.8 (A,B) Change in IR absorbance induced by UV light irradiation of a: NTO, b: 0.1%Sr-NTO, c: 0.3%Sr-NTO, d: 0.5%Sr-NTO, e: 1%Sr-NTO, f: 2%Sr-NTO, g: 5%Sr-NTO, h: 8%Sr-NTO, i: 20%Sr-NTO, j: 50%Sr-NTO, and k: $Sr(Sr_{1/3}Ta_{2/3})O_3$.

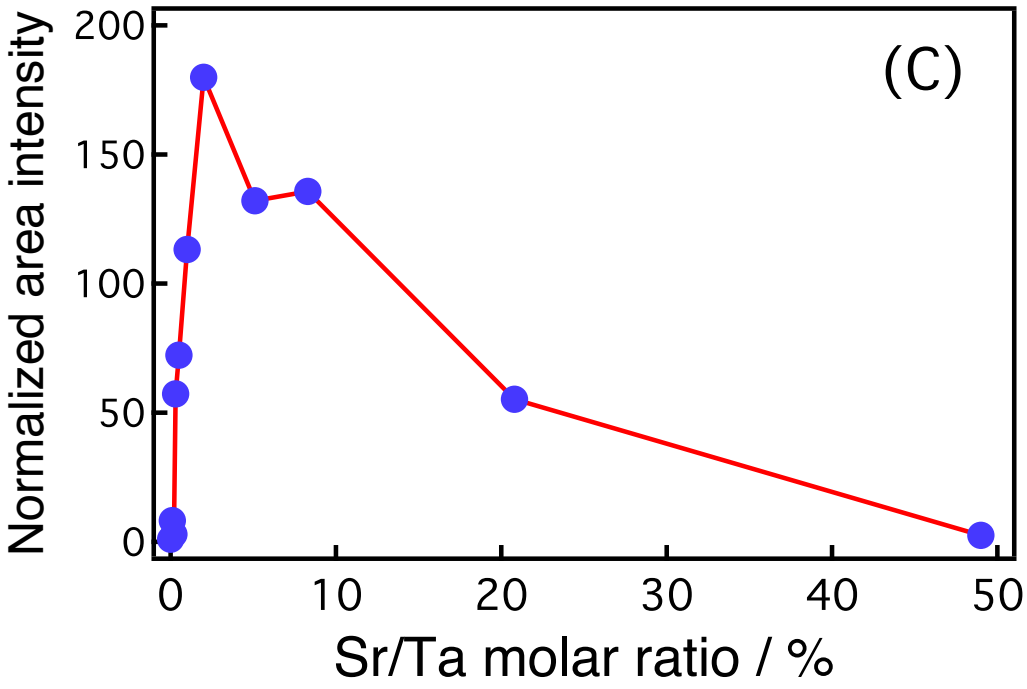

Figure 3.8 (C) Integrated absorbance change is plotted as a function of Sr concentration. The vertical scale is normalized relative to the integrated absorbance of NTO.

3.3.2 Doping site of Sr in Sr-NTO (HTM)

In SSM, Sr substituted A- and B-sites of NTO simultaneously to form a core-shell structured solid solution between $NaTaO_3$ and $Sr(Sr_{1/3}Ta_{2/3})O_3$. In comparison, Sr substituted only A-sites of NTO when synthesized via hydrothermal method (HTM). The effect of doping sites in NTO photocatalysts on electron-hole recombination thus can be studied selectively.

Sr-NTO photocatalysts were prepared by HTM with input Sr concentrations of 0, 1, 2, and 8 mol. Sr/Ta molar ratio was detected by EDX and normalized Sr-Kα emission spectra are shown in **Fig. 3.9**. Calculated Sr concentrations of the Sr-NTOs (HTM) were 1.2, 2.1, and 7.8 mol%, respectively, showing almost the same value as input Sr. Hereafter, Sr-NTO with input Sr concentration of x mol% will be referred to as x%Sr-NTO. For example, Sr-NTO with Sr concentration of 1 mol% will be shown as 1%Sr-NTO.

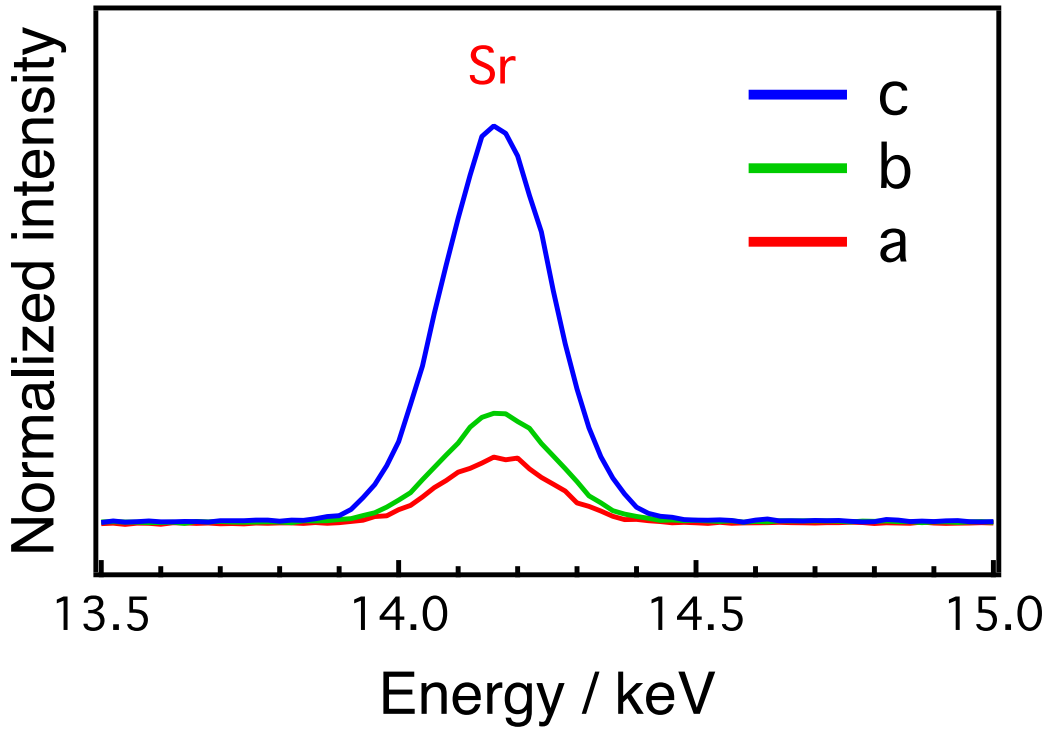

Figure 3.9 X-ray fluorescence spectra of Sr-Kα in Sr-NTOs (HTM). a: 1%Sr-NTO, b: 2%Sr-NTO, and c: 8%Sr-NTO.

Crystallographic structure attributing to $NaTaO_3$ was confirmed by XRD. **Figure 3.10(A)** shows XRD patterns in a range of 10-80° on NTO and Sr-NTOs. Diffraction peaks of the perovskite phase (NTO) were dominant, indicating the synthesis of NTO was successful. Extra peaks appeared at about 28°, 29° and 37° might be assigned to pyrochlore phase, which was common contaminant during synthesis of perovskite phase. In HTM synthesis of $KTaO_3$, [36] a defect pyrochlore, $KTa_2O_5(OH)$, was produced as an intermediate phase that converted to the perovskite product. A Na-containing pyrochlore phase was thus assumed produced in the present study. The pyrochlore phase was minor ingredient compared to the major perovskite phase.

XRD (110) peaks at about 32.4° were compared on Sr-NTOs, as shown in **Fig. 3.10(B)**. In the previous subsection, Sr-NTO (SSM) showed apparent peaks broadening and shifting due to Sr doped at B-sites. On the other hand, peak broadening and shifting were absent on Sr-NTO (HTM). Therefore, the $NaTaO_3$-$Sr(Sr_{1/3}Ta_{2/3})O_3$ solid solutions was not produced in Sr-NTO (HTM). The Sr dopants were assumed to selectively substitute A-sites of NTO.

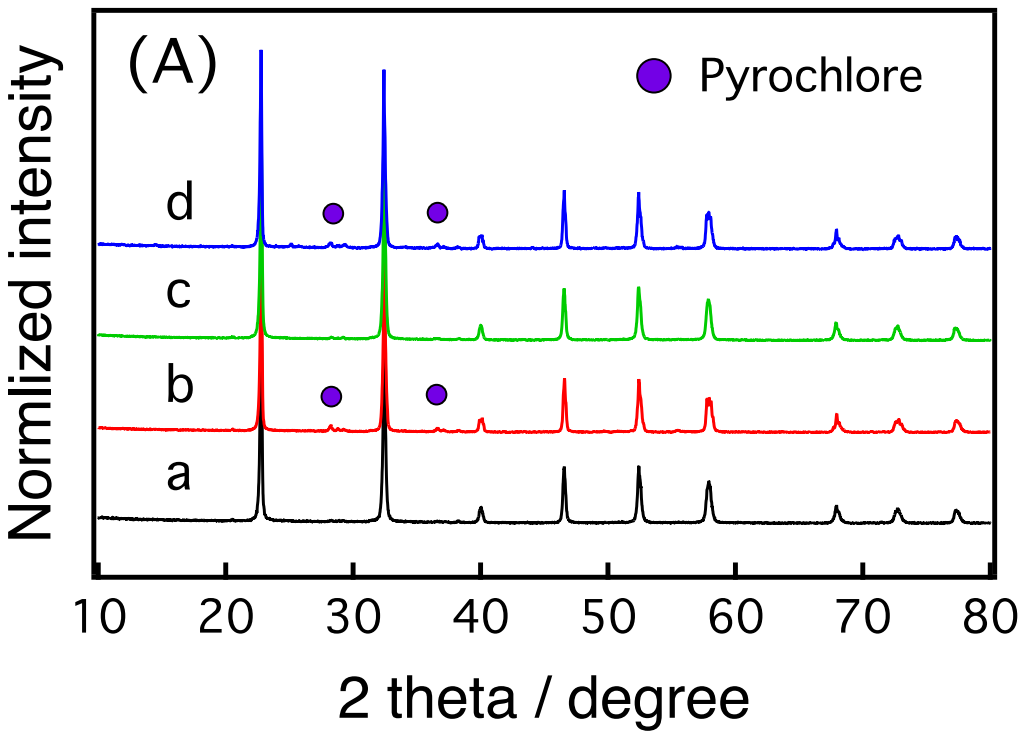

Figure 3.10 (A) XRD patterns (10-80°) of a: NTO, b: 1%Sr-NTO, c: 2%Sr-NTO, and d: 8%Sr-NTO.

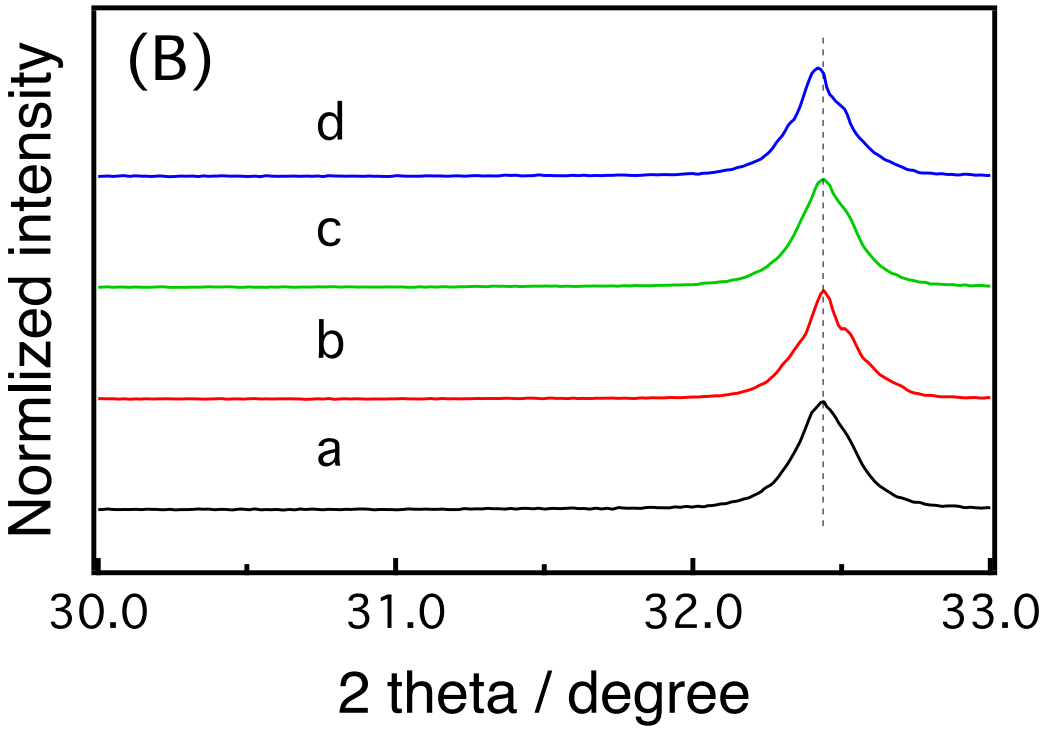

Figure 3.10 (B) XRD patterns (30-33°) of a: NTO, b: 1%Sr-NTO, c: 2%Sr-NTO, and d: 8%Sr-NTO.

The absence of B-sites doping was also supported by Raman scattering on Sr-NTO (HTM). **Figure 3.11** shows Raman spectra of NTO and Sr-NTOs. The Raman band at 860 cm^{-1}, which can indicate B-site-doped NTO, was absent on the Sr-NTO. A-site substitution of NTO did not induce the A_{1g} Raman band (860 cm^{-1}), as was confirmed on K-NTO (SSM) depicted in the previous subsection. The author thus believes the Sr cations selectively occupied A-sites of NTO when doped via HTM.

UV-Vis diffuse-reflection spectra of Sr-NTO are shown in **Fig. 3.12**. UV-Vis absorbance was insensitive to Sr doping. The short-wavelength shift of the absorption edge, which was induced by Sr dopants in Sr-NTO (SSM), was unrecognizable in Sr-NTO (HTM). It is consistent with A-site doping. Since the CB and VB of NTO were mainly composed of Ta 5d (B-site) and O 2p (O-site) orbitals,[24] atomic orbitals of the A-site cations contribute little to the electronic band. A-site doped Sr, hence, should affect much on band gap energy of NTO.

All bulk-sensitive characterization results obtained from XRD, Raman, and UV-Vis spectroscopy support selective doping of Sr at A-sites through HTM.

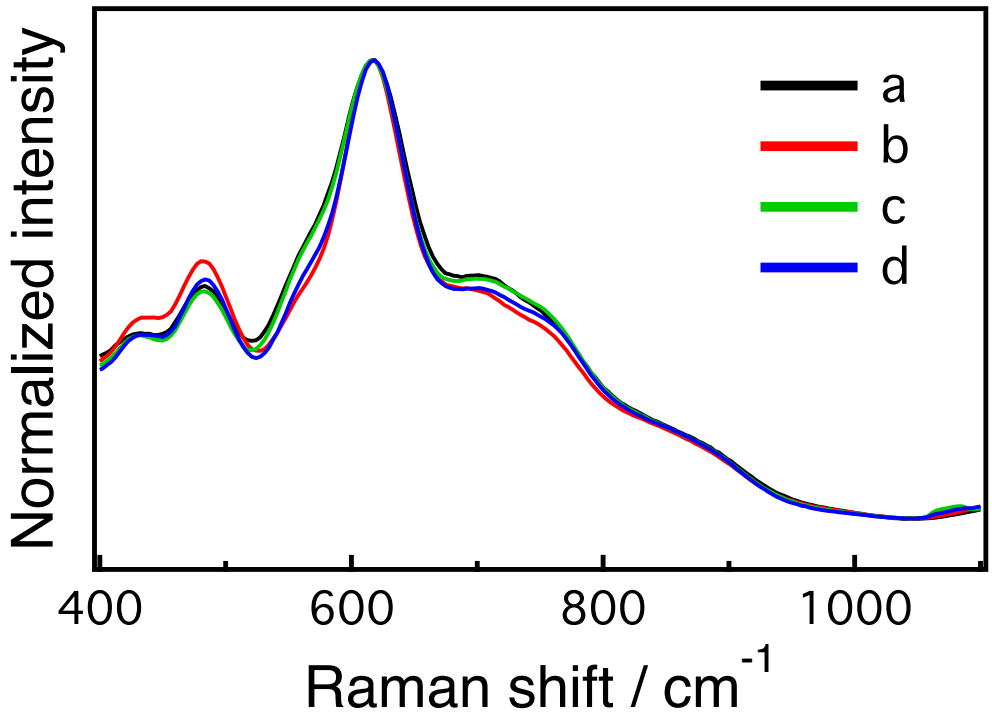

Figure 3.11 Raman spectra of a: NTO, b: 1%Sr-NTO, c: 2%Sr-NTO, and d: 8%Sr-NTO.

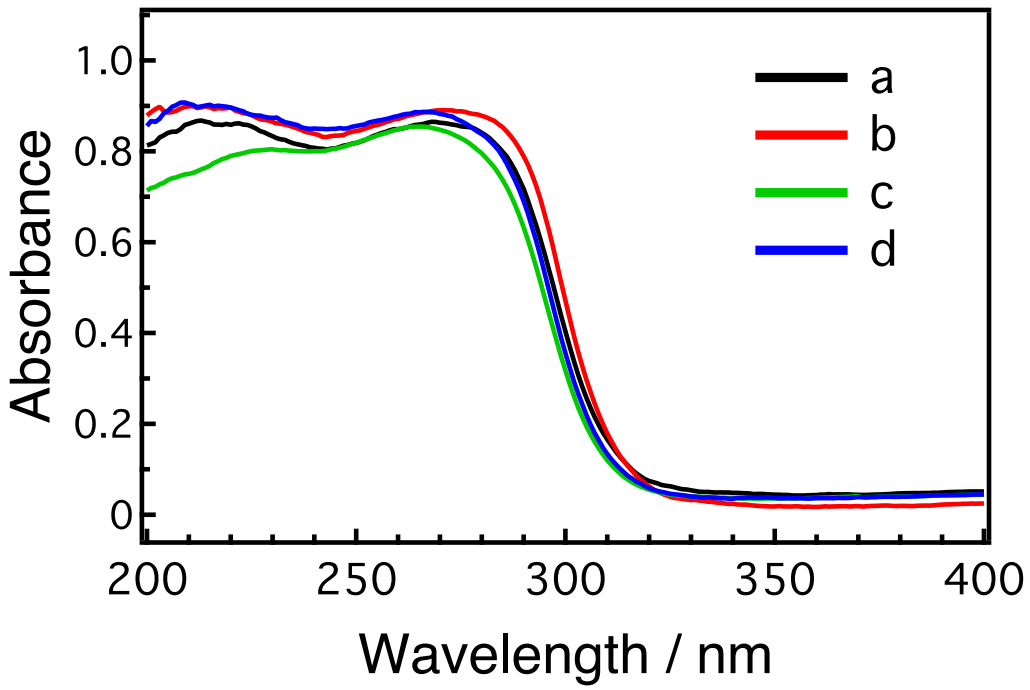

Figure 3.12 UV-vis diffuse-reflection spectra of a: NTO, b: 1%Sr-NTO, c: 2%Sr-NTO, and d: 8%Sr-NTO. The apparent absorbance without Kubelka-Munk transformation is shown.

In an earlier study about $KTaO_3$ synthesized via HTM,[36] finite amounts of OH^- and H_2O remained in the product. Sr-NTO (HTM) prepared in the present study also contained OH^- and H_2O species. **Figure 3.13** shows IR absorbance spectra of NTO and 2%Sr-NTO (before and after calcination). The consistent increase of IR absorbance from 3000 cm^{-1} to 4000 cm^{-1} attributed to IR light scattering on the small photocatalyst particles. IR light with shorter wavenumber (higher wavelength) could be easily scattered by the particles.

NTO and 2%Sr-NTO presented broad IR absorption band corresponding to water-derived species (OH^- and H_2O) appeared at 3000-3600 cm^{-1}. Water-derived species should be sensitive to calcination at high temperature. To remove the species, 2%Sr-NTO was heated at 773 K and 1073 K for 3 h, respectively. IR absorption band at 3000-3600 cm^{-1} remained at 773 K heating but completely removed at 1073 K. Heating at 1073 K was found as an effective way to volatilize water-derived species those were contained in Sr-NTO (HTM).

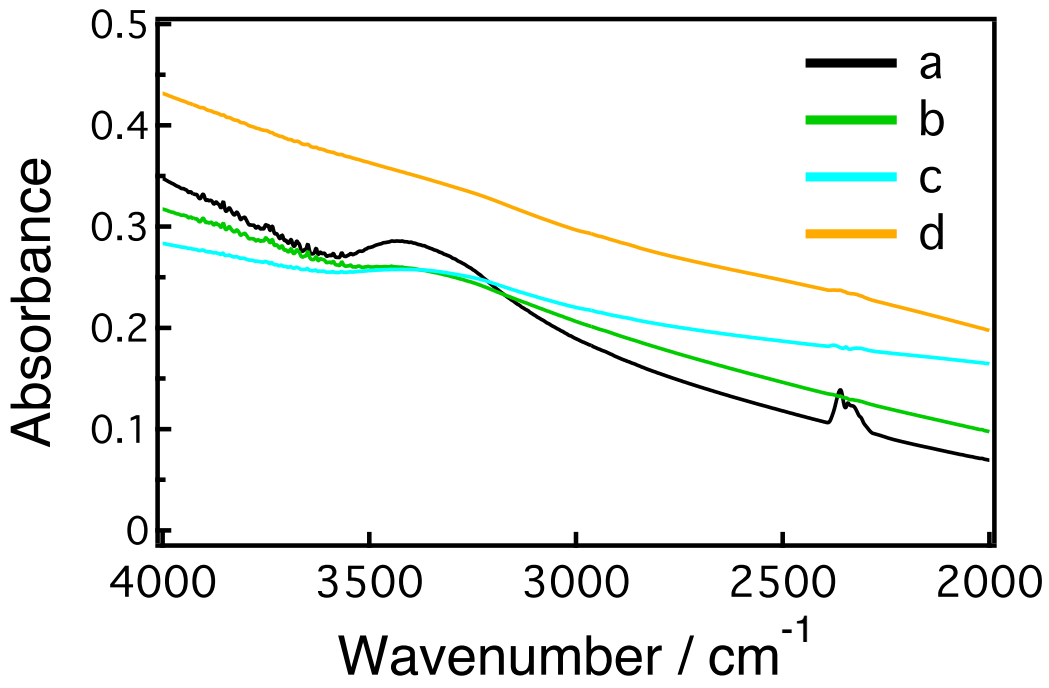

Figure 3.13 IR absorption spectra of a: NTO, and b: 2%Sr-NTO. 2%Sr-NTO was calcined at 773 K and at 1073 K produced curve c and d, respectively.

Effect of selective A-site doping of Sr on electron-hole recombination was interesting to know. UV-induced IR absorption spectroscopy was again applied to study recombination of electrons and holes by quantifying population of photoexcited electrons that were not recombined with holes.

Figure 3.14 shows IR absorbance change induced by UV irradiation. NTO (HTM) produced a weak response with a monotonic absorbance change spectrum similar to that observed with NTO (SSM). The monotonic spectrum is attributed to the optical transitions of band gap excited electrons. The IR absorbance change was remained small in 2%Sr-NTO and 8%Sr-NTO. Weak response to UV irradiation indicates the photoexcited electrons efficiently recombined with holes. Unlike to strong IR absorbance change produced in Sr-NTO (SSM), selective doping of Sr at A-sites failed to restricted electron-hole recombination.

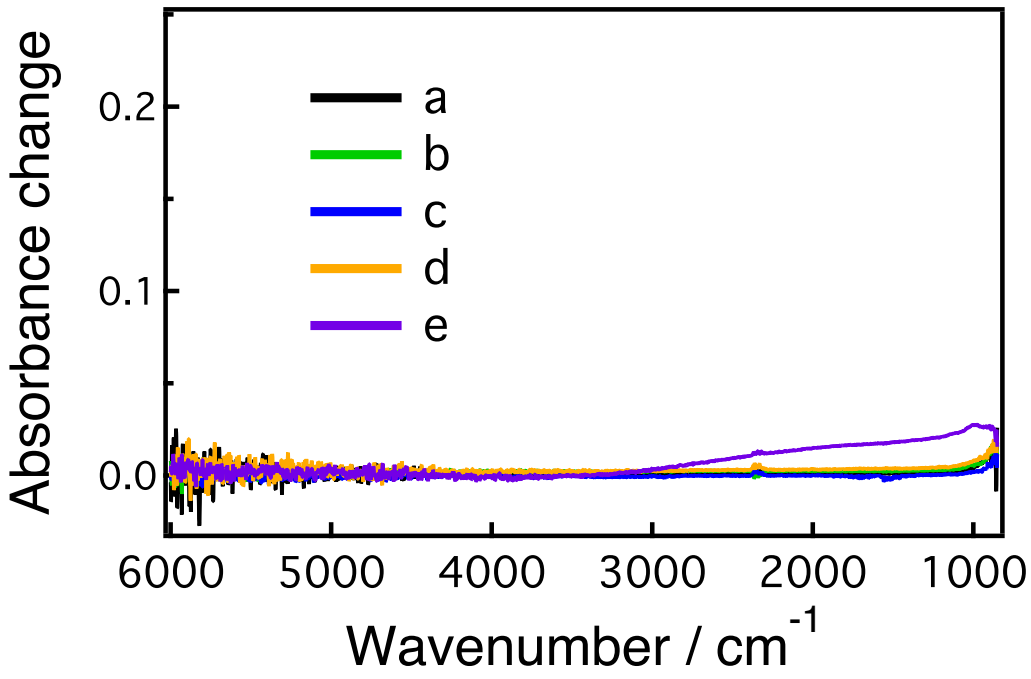

Figure 3.14 Change in IR absorbance induced by UV light irradiation of a: NTO, b: 2%Sr-NTO, and c: 8%Sr-NTO. 2%Sr-NTO was calcined at 1073 K in the absence or presence of Na_2CO_3 produced curve d and e, respectively.

The water-derived species remained in Sr-NTO (HTM) might be the cause of the efficient recombination of electrons and holes. To examine the interpretation, 2%Sr-NTO calcined at 1073 K was detected and it exhibited weak IR absorbance change. It suggests the water-derived species played a limited role in electron-hole recombination in photocatalysts prepared via HTM. Therefore, the effect of water-derived species on electron-hole recombination can be excluded.

Not only the calcination at 1073 K can volatilize water-derived species, but it also may induce structural change to the Sr-NTO (HTM) lattices. In SSM, Sr substituted A- and B-sites of NTO simultaneously when heated at 1423 K, which was much higher than 473 K that was used in HTM. The author assumed a lack of B-site doping in Sr-NTO (HTM) might due to heating at low temperature. Replacement of Sr^{2+} for Ta^{5+} at B-sites should need strong energy to cover the difference in both cationic radii and electric charge. Calcination at 1073 K may provide enough energy for parts of Sr at A-sites to resubstitute Ta at B-sites. However, Sr transferred to B-sites from A-sites should leave vacancies in A-sites. A-site vacancies, if any, will demand extra energy for Sr transition from A-sites to B-sites. To realize B-site doping of Sr, calcination in the presence of Na_2CO_3 at 1073 K was performed on 2%Sr-NTO (curve e). UV-induced IR absorbance change of the A-site resorted 2%Sr-NTO increased relative to the other photocatalysts, although the absorbance was much weaker than Sr-NTO (SSM).

The Raman spectrum of the sample with restored Na is shown in **Fig. 3.15**. The marker band at 860 cm^{-1} appeared to indicate the relocation of some Sr^{2+} cations from A-sites to B-sites. This temperature-induced relocation suggests the Sr doping at A-sites alone is thermodynamically less stable in NTO than solid-solution formation with $Sr(Sr_{1/3}Ta_{2/3})O_3$. A-site doping with HTM is kinetically favorable.

Figure 3.16 shows SEM images of NTO and 2%Sr-NTO. Step structures were absent, but perfect cubes were produced on both NTO and 2%Sr-NTO. The particle size was within 0.2-0.5 μm and remained insensitive to Sr doping. After calcination in the presence of Na_2CO_3, 2%Sr-NTO particles were reconstructed to round corners and stuck together. It suggests the occurrence of structural change during calcination. The reconstruction attributed relocation of Sr from A- to B-sites as was detected by Raman spectroscopy.

In HTM, Sr substituted A-sites alone did not restrict electron-hole recombination. Relocation of some Sr to B-sites restricted recombination more efficiently. Doping site of Sr in NTO was thus believed significant to control electron-hole recombination.

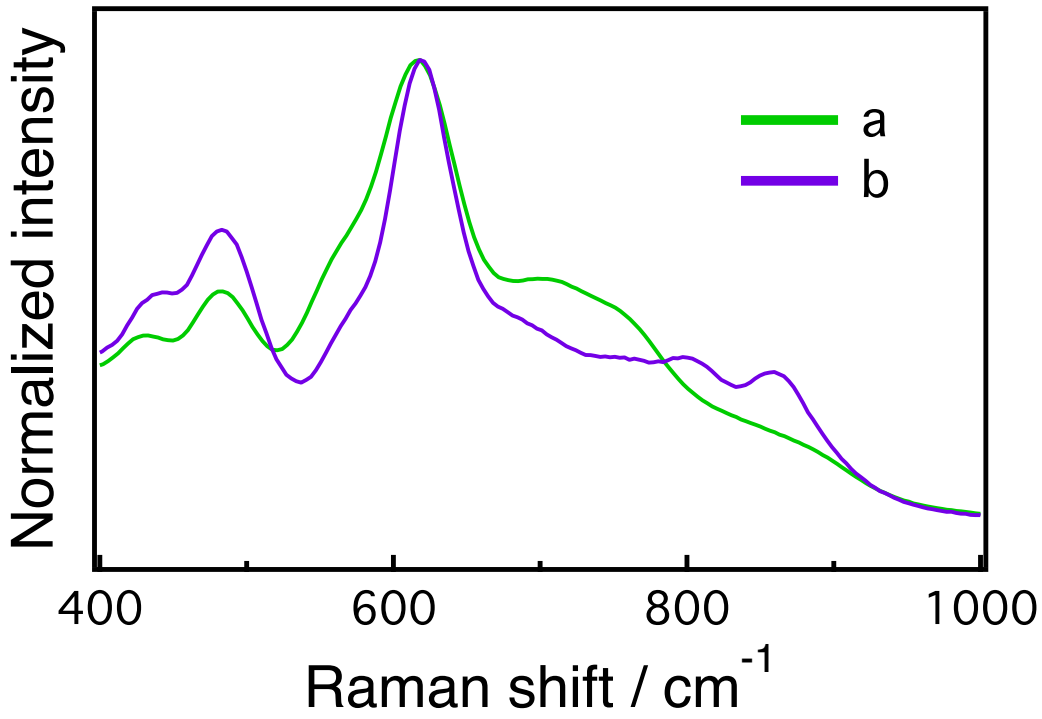

Figure 3.15 Raman spectra of a: 2%Sr-NTO, and b: 2%-Sr-NTO calcined at 1073 K for 3 h in the presence of Na_2CO_3.

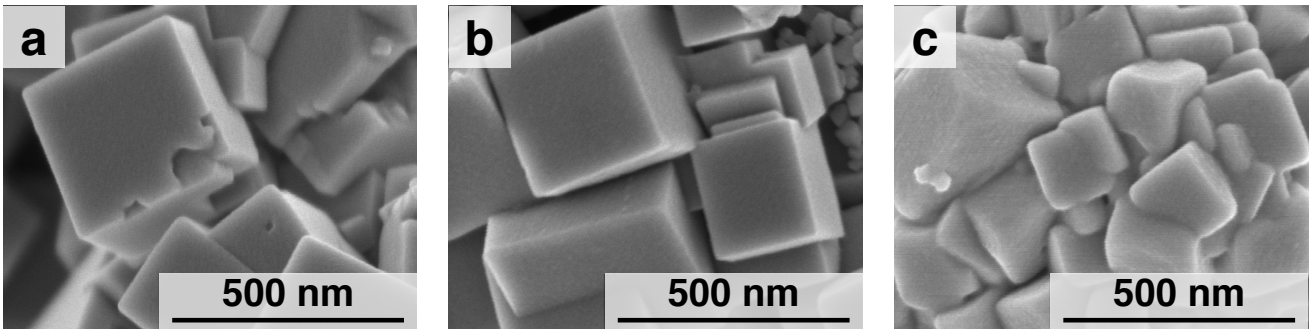

Figure 3.16 Scanning electron micrographs of a: NTO, b: 2%Sr-NTO, and c: 2%Sr-NTO calcined at 1073 K for 3 h in the presence of Na_2CO_3.

3.3.3 Doping site of Sr in Sr-NTO (STM)

As described in the previous subsections, Sr substituted A- and B-sites of NTO simultaneously when doped via SSM, but substituted only A-sites when doped via HTM. The B-site doped Sr restricted the recombination of photoexcited electrons and holes efficiently. Sr failed to substitute B-sites in Sr-NTO (HTM) might be due to low heating temperature. HTM was not able to supply energy high enough for B-site doping. In this subsection, B-site doping of Sr to NTO was tried upon low heating temperature using solvothermal method (STM).

In STM, Sr^{2+} and Ta^{5+} cations were provided from metal alkoxides; $Sr(OC_3H_7)_2$ and $Ta(OC_2H_5)_5$, respectively. Sr- and Ta-alkoxides were blended well in ethanol solvent before dripping the solution into NaOH aqueous solution under cooling with ice water. When meeting NaOH aqueous solution under low temperature, the mixed metal alkoxides were expected to rapidly convert to mixed metal oxides through hydrolysis reaction for generating some Sr-O-Ta bonds. In the B-site doped Sr-NTO, Sr substituted Ta at B-sites to form Sr-O-Ta bonds as bone structure. With Sr-O-Ta bonds already prepared, the author assumed easier synthesis of B-site doped Sr-NTO even under low heating temperature as 473 K.

NTO and Sr-NTO were synthesized via STM. Input Sr concentrations were 0, 2, and 5 mol%. Sr concentrations of the products were detected by EDX as usual, and the Sr/Ta molar ratio was 1.4 mol% in 2%Sr-NTO and was 6.6 mol% in 5%Sr-NTO. With high sensitivity to air conditions, the volume of $Sr(OC_3H_7)_2$ and $Ta(OC_2H_5)_5$ were rapidly measured for adjusting input concentrations of Sr. As a result, a relatively high error occurred to the Sr concentration.

Figure 3.17 shows XRD patterns of NTO and Sr-NTOs prepared via STM. In **Panel (A)**, characteristic XRD peaks referring to perovskite-structured NTO were produced on NTO and Sr-NTO. 5%Sr-NTO showed minor impurity phase might attribute to pyrochlore phase. In **Panel (B)**, XRD (110) peak degree was compared to confirm peak shift induced by Sr doping. The peak gradually shifted from 32.40° in NTO to 32.35° in 5%Sr-NTO with increased Sr concentration. B-site doping should induce the lattice volume to increase. Consequently, XRD peaks will shift to a lower angle. The gradual shift caused by Sr doping indicates parts of Sr doped at B-sites.

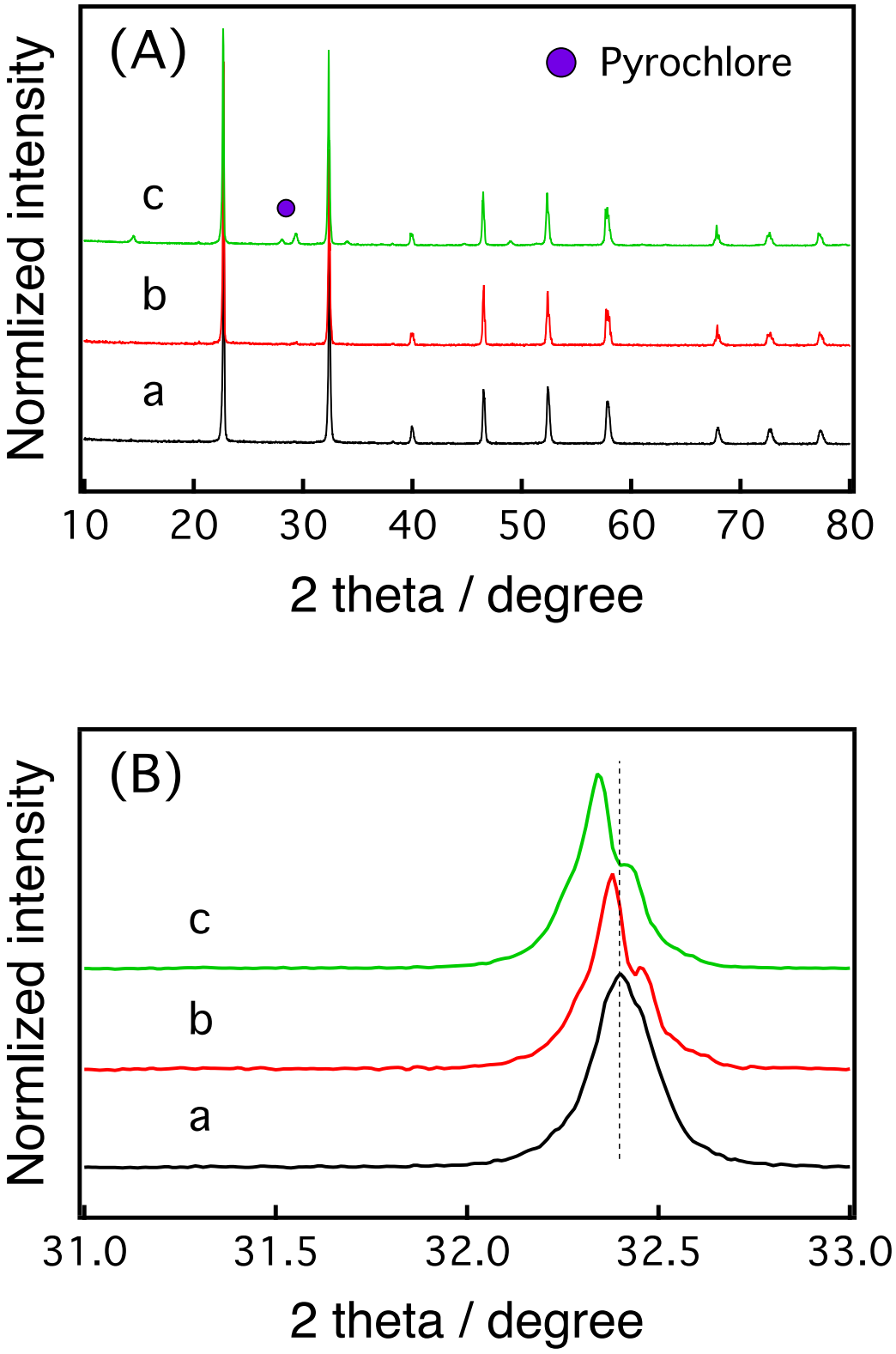

Figure 3.17 XRD patterns of a: NTO, b: 2%Sr-NTO, and c: 5%Sr-NTO. (A) 10-80° and (B) 31-33°.

B-site doping of Sr was supported with Raman scattering. **Figure 3.18** shows Raman spectra of NTO and Sr-NTO. 860 cm^{-1} Raman band, which is a sign of B-site doping, was detected on Sr-NTO. The intensity of the 860 cm^{-1} band increased consistently with Sr concentration. Combined with gradual shift of XRD (110) peak, the Raman scattering results suggest part of Sr substituted B-sites in Sr-NTO prepared via STM. And the concentration of Sr doped at B-sites was related to input Sr concentration.

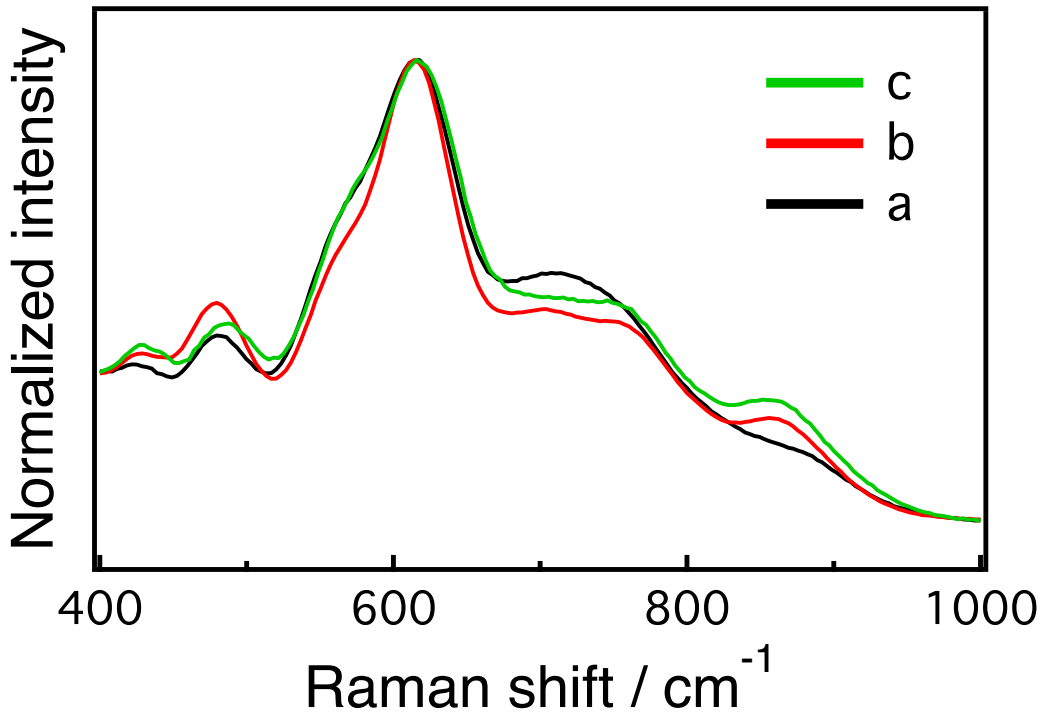

Figure 3.18 Raman spectra of a: NTO, b: 2%Sr-NTO, and c: 5%Sr-NTO.

Figure 3.19 shows SEM images of NTO and Sr-NTO. In NTO, 3-5 μm sized particles were produced to form cube shapes. With doping of Sr at 2 mol%, the particle shape was transformed to perfect cubes. The reason for the formation of the perfect cubes in 2%Sr-NTO is still uncertain, but may be related to B-site doping of Sr. When the Sr concentration increased to 5 mol%, contaminants with blurred form were produced around the cubic particles. In XRD, 5%Sr-NTO presented impurity phases from perovskite phase. The blurred contaminants observed by SEM, hence, was attributed to impurity phase detected by XRD.

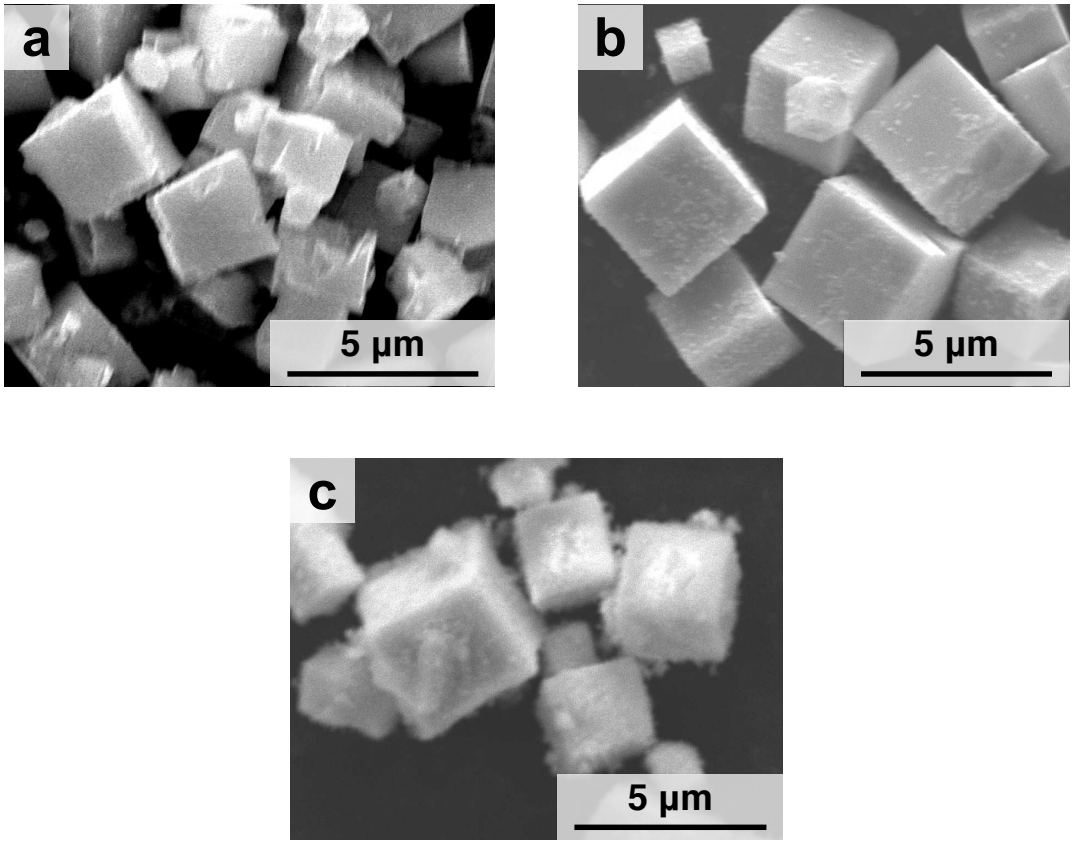

Figure 3.19 Scanning electron micrographs of a: NTO, b: 2%Sr-NTO, and c: 5%Sr-NTO.

B-site doped Sr-NTO was successfully prepared by STM under low heating temperature. The effect of B-site doping on electron-hole recombination was examined by UV-induced IR absorption spectroscopy. IR absorbance changes induced by UV irradiation of NTO and Sr-NTO are shown in **Fig. 3.20**.

Pristine NTO (STM) presented IR absorbance change with similar extent as NTO prepared via SSM or HTM. In 2%Sr-NTO (STM) and 5%Sr-NTO (STM), the absorbance change increased drastically when some Sr were doped at B-sites. Compared to A-site doped Sr-NTO (HTM), the electron-hole recombination was efficiently restricted in Sr-NTO (STM). The most apparent difference between these two series of Sr-NTO (HTM or STM) should be presence or absence of B-site doping.

In summary, electron-hole recombination in Sr-NTO was restricted in the presence of B-site doping (SSM or STM) but was barely restricted in the absence of B-site doping (HTM).

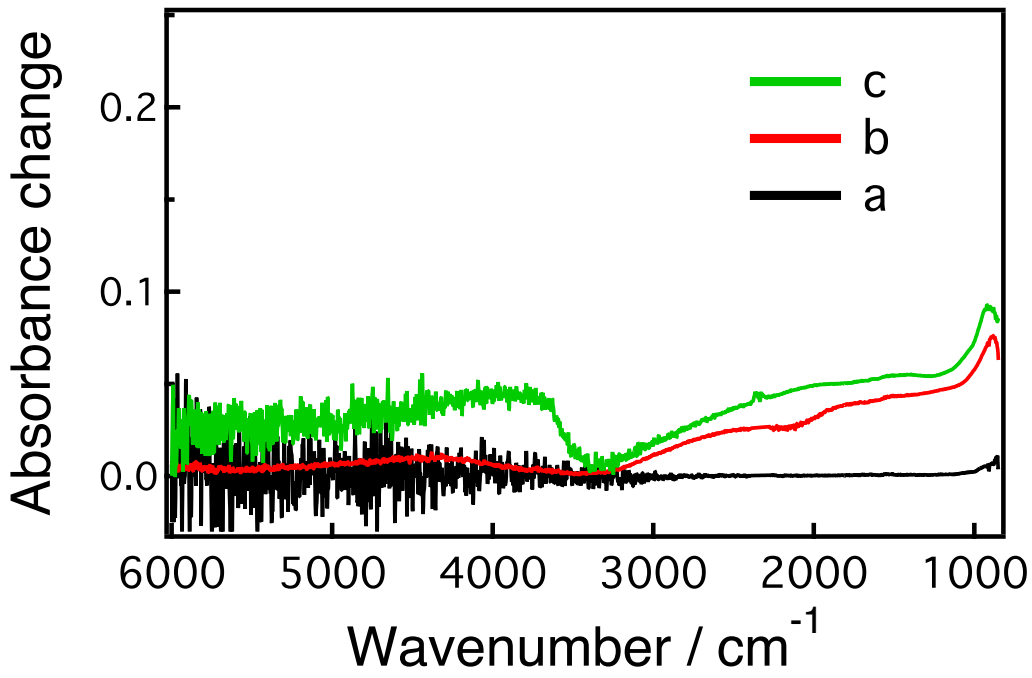

Figure 3.20 Change in IR absorbance induced by UV light irradiation of a: NTO, b: 2%Sr-NTO, and c: 5%Sr-NTO.

3.4 CONCLUSION

1) In the solid-state method, Sr substituted both A- and B-sites of $NaTaO_3$ to form core-shell structured $NaTaO_3$-$Sr(Sr_{1/3}Ta_{2/3})O_3$ solid solutions. $NaTaO_3$ with partial B-site doping caused of BO_6 breathing vibration that was detected by Raman spectroscopy at 860 cm^{-1}. Replacing of smaller Ta^{5+} (0.06 nm) by larger Sr^{2+} (0.12 nm) induced serious lattice expansion in the shell. Lattice mismatch at the core-shell interface produced steps and terraces on the surface. Electron-hole recombination was restricted in the solid solutions. The steady-state population of photoexcited electrons was increased by 180 times at a Sr concentration of 2 mol%. Simultaneous doping of Sr at A- and B-sites in NTO restricted electron-hole recombination.

2) In the hydrothermal method, Sr substituted only A-sites of $NaTaO_3$. BO_6 vibration, lattice expansion or step structures were absent. Electron population was not enhanced, either. Doping of Sr at A-sites alone failed to restrict electron-hole recombination.

3) In the solvothermal method, some Sr substituted B-sites of $NaTaO_3$ despite being synthesized with almost the same heating temperature as the hydrothermal method. Advance preparation of Sr-O-Ta bonds played a key role for successful B-site doping. With B-sites doped, a BO_6 vibration was detected at 860 cm^{-1} and lattices were expanded. Consistently, electron population was enhanced drastically. B-site doping nicely restricted electron-hole recombination.

3.5 REFERENCE

(1) Kudo, A.; Kato, H. *Chem. Phys. Lett.* **2000**, *331*, 373-377.

(2) Kato, H.; Asakura, K.; Kudo, A. *J. Am. Chem. Soc.* **2003**, *125*, 3082-3089.

(3) Sakata, Y.; Matsuda, Y.; Yanagida, T.; Hirata, K.; Imamura, H.; Teramura, K. *Catal. Lett.* **2008**, *125*, 22-26.

(4) Iwase, A.; Kato, H.; Okutomi, H.; Kudo, A. *Chem. Lett.* **2004**, *33*, 1260-1261.

(5) Iwase, A.; Kato, H.; Kudo, A. *ChemSusChem* **2009**, *2*, 873-877.

(6) Yamakata, A.; Ishibashi, T.; Kato, H.; Kudo, A.; Onishi, H. *J. Phys. Chem. B* **2003**, *107*, 14383-14387.

(7) Maruyama, M.; Iwase, A.; Kato, H.; Kudo, A.; Onishi, H. *J. Phys. Chem. C* **2009**, *113*, 13918-13923.

(8) Li, X.; Zang, J. *Catal. Comm.* **2011**, *12*, 1380-1383.

(9) He, Y.; Zhu, Y. *Chem. Lett.* **2004**, *33*, 900-901.

(10) Ahtee, M.; Unonius, L. Acta Crystallogr., Sect. A: Cryst. Phys., Diffr., Theor. Gen. *Crystallogr.* **1977**, *33*, 150-154.

(11) Yoshioka, K.; Petrykin, V.; Kakihana, M.; Kato, H.; Kudo, A. *J. Catal.* **2005**, *232*, 102-107.

(12) Shannon, R. D. Acta Crystallogr., Sect. A: Cryst. Phys., Diffr., Theor. Gen. *Crystallogr*. **1976**, *32*, 751-767.

(13) Shimura, K.; Kato, S.; Yoshida, T.; Itoh, H.; Hattori, T.; Yoshida, H. *J. Phys. Chem. C* **2010**, *114*, 3493-3503.

(14) Sun, J.; Chen, G.; Pei, J.; Jin, R.; Wang, Q.; Guang, X. *J. Mater. Chem.* **2012**, *22*, 5609-5614.

(15) Teixeira, N. G.; Dias, A.; Moreira, R. L. *J. Eur. Ceram. Soc.* **2007**, *27*, 3683-3686.

(16) Siny, I. G.; Tao, R.; Katiyar, R. S.; Guo, R.; Bhalla, A. S. *J. Phys. Chem. Solids* **1998**, *59*, 181-195.

(17) Zheng, H.; Reaney, I. M.; Csete de Györgyfalva, G. D. C.; Ubic, R.; Yarwood, J.; Seabra, M. P.; Ferreira, V. M. *J. Mater. Res*. **2004**, *19*, 488-495.

(18) Smolensky, G. A.; Siny, I. G.; Pisarev, R. V.; Kuzminov, E. G. *Ferroelectrics* **1976**, *12*, 135-136.

(19) Perry, C. H.; Tornberg, N. E. *Phys. Rev.* **1969**, *183*, 595-603.

(20) Hu, C.-C.; Lee, Y.-L.; Teng, H. *J. Mater. Chem.* **2011**, *21*, 3824- 3830.

(21) Sun, J.; Chen, G.; Li, Y.; Jin, R.; Wang, Q.; Pei, *J. Energy Environ. Sci.* **2011**, *4*, 4052-4060.

(22) Choi, M.; Oba, F.; Tanaka, I. *Phys. Rev. B: Condens. Matter Mater. Phys.* **2008**, *78*, 014115 (8 pages).

(23) Kato, H.; Kobayashi, H.; Kudo, A. *J. Phys. Chem. B* **2002**, *106*, 12441-12447.

(24) Modak, B.; Srinivasu, K.; Ghosh, S.K. *Phys. Chem. Chem. Phys.* **2014**, *16*, 17116-17124.

(25) Atuchin, V. V.; Grivel, J.-C.; Zhang, Z. *Chem. Phys.* **2009**, *360*, 74-78.

(26) Ertl, G.; Küppers, *J. Low Energy Electrons and Surface Chemistry; Wiley-VCH Verlag: Weinheim*, **1986**; p 7.

(27) Iwase, A.; Saito, K.; Kudo, A. *Bull. Chem. Soc. Jpn.* **2009**, *82*, 514-518.

(28) Yi, Z.-G.; Ye, J.-H. *J. Appl. Phys*. **2009**, *106*, 074910.

(29) Kanhere, P.; Nisar, J.; Tang, Y.; Pathak, B.; Ahuja, R.; Zheng, J.; Chen, Z. *J. Phys. Chem. C* **2012**, *116*, 22767-22773.

(30) Furuhashi, K.; Qingxin, J.; Kudo, A.; Onishi, H. *J. Phys. Chem. C* **2013**, *117*, 19101-19106.

(31) Yamakata, A.; Ishibashi, T.; Onishi, H. *Chem. Phys. Lett.* **2001**, *333*, 271-277.

(32) Szczepankiewicz, S. H.; Moss, J. A.; Hoffmann, M. R. *J. Phys. Chem. B* **2002**, *106*, 2922-2927.

(33) Yoshihara, T.; Katoh, R.; Furube, A.; Tamaki, Y.; Murai, M.; Hara, K.; Murata, S.; Arakawa, H.; Tachiya, M. *J. Phys. Chem. B* **2004**, *108*, 3817-3823.

(34) Warren, D. S.; McQuillan, A. J. *J. Phys. Chem. B* **2004**, *108*, 19373-19379.

(35) Panayotov, D. A.; Burrows, S. P.; Morris, J. R. *J. Phys. Chem. C* **2012**, *116*, 4535-4544.

(36) Goh, G. K. L.; Haile, S. M.; Levi, C. G.; Lange, F. F. *J. Mater. Res.* **2002**, *17*, 3168-3176.

Chapter 4

HF etching on Sr-doped $NaTaO_3$ (SSM)

4.1 INTRODUCTION

In chapter 3 of this thesis, Sr-doped $NaTaO_3$ photocatalysts were synthesized via solid-state method (SSM), hydrothermal method (HTM), and solvothermal method (STM). Characterization results suggested Sr dopants substituted B-sites of $NaTaO_3$ via SSM and STM, consequently, electron-hole recombination was restricted. On the other hand, Sr substituted A-sites alone via HTM played a little effect on electron-hole recombination. In a comparison of Sr-NTOs prepared via SSM and STM, the population of photoexcited electrons was much larger in Sr-NTO (SSM) than in Sr-NTO (STM) with fixed Sr concentration.

In Sr-NTO (SSM), electron population increased to a maximum with Sr concentration at 2 mol% but then decreased gradually with Sr concentration larger than 2 mol%. The consistent increase of 860 cm^{-1} Raman band intensity (sign of B-site doping) explains gradual increment of Sr concentration at B-sites. The decreased population of photoexcited electrons with excessive Sr larger than 2 mol% is, therefore, not controlled by B-site doping alone. A factor beyond B-site doping is affecting electron-hole recombination here.

In chapter 4, the reason for the decreased electron population induced by excessive doping of Sr in Sr-NTO (SSM) was mainly studied. Sr-NTO particles were assumed to form a core-shell structured $NaTaO_3$-$Sr(Sr_{1/3}Ta_{2/3})O_3$ solid solutions. A Sr-rich shell might form in a heteroepitaxial manner over a Sr-poor core. In this chapter, the core-shell structured Sr-NTO (SSM) particles were chemically etched with hydrofluoric acid (HF) aqueous solution to investigate the different roles of the core and shell on electron-hole recombination.

In 5%Sr-NTO (SSM), particles were confirmed by etching to be composed of a core-shell structure. Sr segregated seriously in the shell and a Sr concentration gradient was formed in the core. Electrons and holes were excited in the Sr-poor core and recombined in the Sr-rich shell. In the shell, complex structures might contribute to the acceleration of electron-hole recombination. While in the core, the recombination was restricted due to the concentration gradient of Sr doped at B-sites, which induced a formation of a potential gradient of conduction band (CB) minimum of $NaTaO_3$. Electron-hole separation was driven by potential gradient. As a result, electron-hole recombination was restricted in the core.

4.2 EXPERIMENTAL SECTION

4.2.1 HF etching

Sr-NTOs (SSM) were used as etching materials. Each Sr-NTO (1 g) was stirred in Teflon jar containing an aqueous HF solution (10 wt%, 3 ml, Wako) for a certain period of time at room temperature. Then washed with purified water until the pH was maintained at about 7. According to earlier study about HF etching on Ta-containing minerals,[1] possible stoichiometric reaction for etching on $NaTaO_3$ should be; $NaTaO_3 + 8HF \rightarrow NaF + H_2TaF_7 + 3\ H_2O$.

4.2.2 Characterization

The size and shape of photocatalyst particles were observed by SEM (Hitachi High-Technologies, S-4800). The composition of Sr-NTOs in bulk and on the surface was quantified by EDX (Shimadzu, EDX-720) and XPS (Ulvac-Phi, PHI X-tool), respectively. The crystallographic lattice was determined by XRD (Rigaku, SmartLab). Raman scattering was detected in the air with a spectrometer (Jasco, NRS-7100) using laser light with an excitation wavelength of 532 nm. Infrared (IR) light absorption induced by ultraviolet (UV) light irradiation was observed was obtained with a Fourier-transform spectrometer (Jasco, FT/IR610) in the presence and in the absence of UV light irradiation. A 200-W Hg-Xe lamp (San-ei Electric, UVS-204S) was used as the UV light source. Light power at wavelengths of less than 370 nm was 60 mW cm^{-2} in the full spectrum of radiation.

4.3 RESULTS AND DISCUSSION

4.3.1 Response to HF etching on 5%Sr-NTO

5%Sr-NTO was etched with HF aqueous solution for 5, 10, 30, 120, 300, and 480 m (minutes), respectively. Hereafter, 5%Sr-NTO etched for x m is referred to like 5%Sr-NTO/ xm, for example, 5%Sr-NTO/10m represents 5%Sr-NTO etched with HF for 10 m. The particle size, bulk and surface composition, Raman-active lattice vibrations, and crystallographic lattices were detected as a function of etching time to evaluate the core-shell structure. The effect of core and shell on electron-hole recombination was examined by UV-induced IR absorption spectroscopy.

Figure 4.1 shows SEM images of 5%Sr-NTO particles before and after etching. Before etching, 5%Sr-NTO (image a) with a particle size larger than 0.5 μm also produced the ten-nanometer-length steps on the surface. The steps could be attributed to lattice mismatch between $NaTaO_3$ and $Sr(Sr_{1/3}Ta_{2/3})O_3$ solid solutions. As the etching increased from 10 to 480 m, particle size of 5%Sr-NTO decreased consistently, as can be observed in images b-f. The reduced particle size by etching indicates the surface layer of 5%Sr-NTO particles was successfully dissolved with HF solution. With etching times of 10 and 30 m (b and c), ten-nanometer-length steps were observed on the surface of particles, whereas with etching times of 120, 300, and 480 m (d, e, and f, respectively), these steps were absent on the particles.

Etching should reduce the bulk and the surface Sr/Ta molar ratio as Sr segregates on the surface of Sr-NTO particles. The bulk composition was detected by EDX. **Figure 4.2(A)** shows Sr-Kα emission spectra, with intensity normalized to that of Ta-Lα emission, of etched 5%Sr-NTO. The Sr/Ta molar ratios estimated from the intensity of the Sr-Kα emission relative to that of Ta-Lα emission was plotted as a function of etching time, as shown in **Fig. 4.2(B)**.

Before etching, calculated Sr/Ta ratio in 5%Sr-NTO was 5.1 mol%. During etching till 10 m, the Sr/Ta ratio rapidly decreased to 4.6 mol%. This fast reduction of Sr concentration supports the core-shell structure that was proposed in chapter 3. Sr segregated seriously in the shell. In contrast, Sr/Ta ratio decreased gradually with etching for a longer period than 10 m. The Sr concentration 4.6 mol% (5%Sr-NTO/10m) was eventually reduced to 3.4 mol% (5%Sr-NTO/

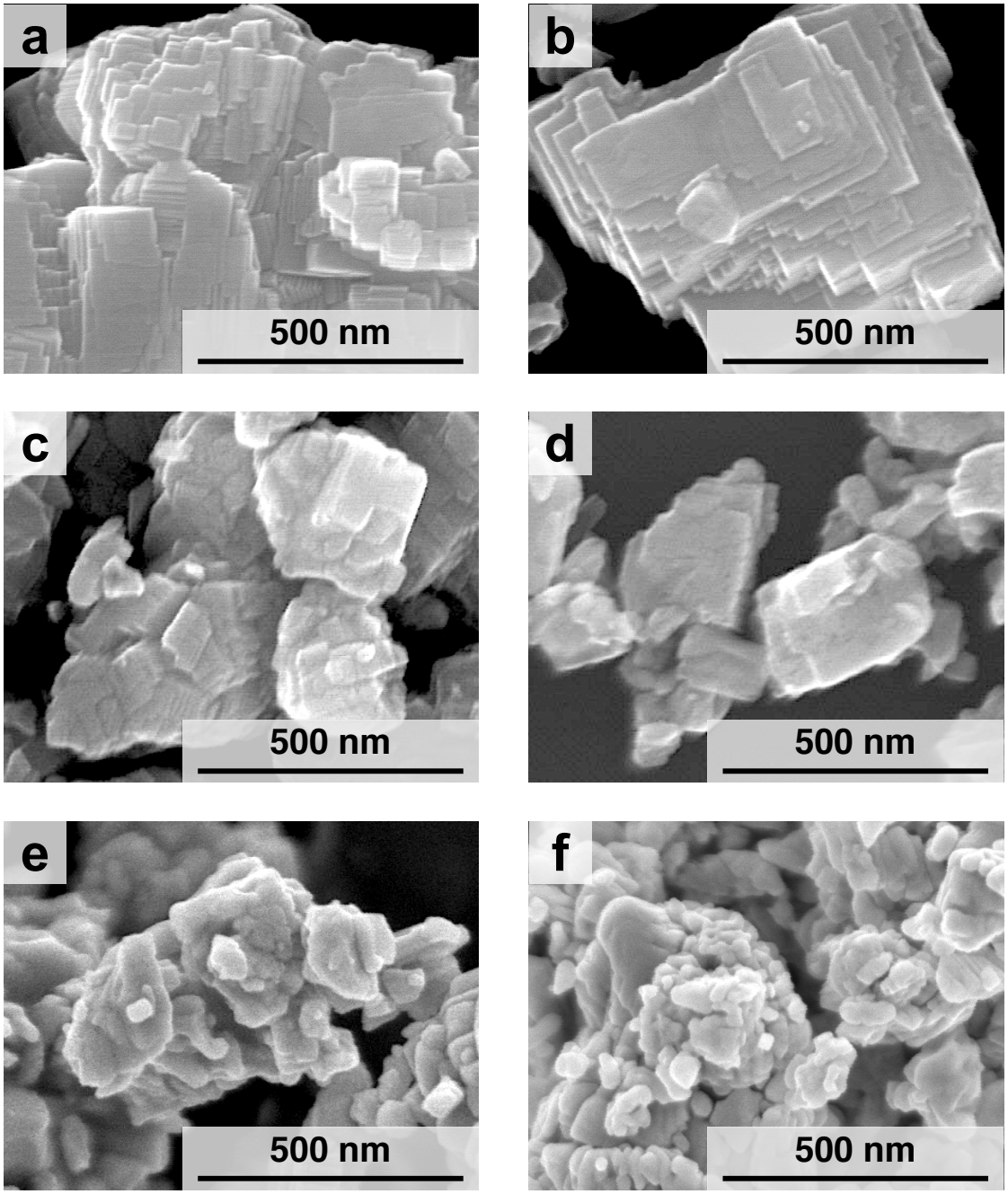

Figure 4.1 Scanning electron micrographs of 5%Sr-NTO etched with HF for a: 0, b: 10 m, c: 30 m, d: 120 m, e: 300 m, and f: 480 m.

480m) under etching for 470 m. This gradual but finite response to etching time indicates the presence of Sr concentration gradient in the core. The two-step response to the Sr/Ta ratio by etching, a rapid decrease followed with a gradual reduction, evidenced an interface between Sr-rich shell and Sr-poor core.

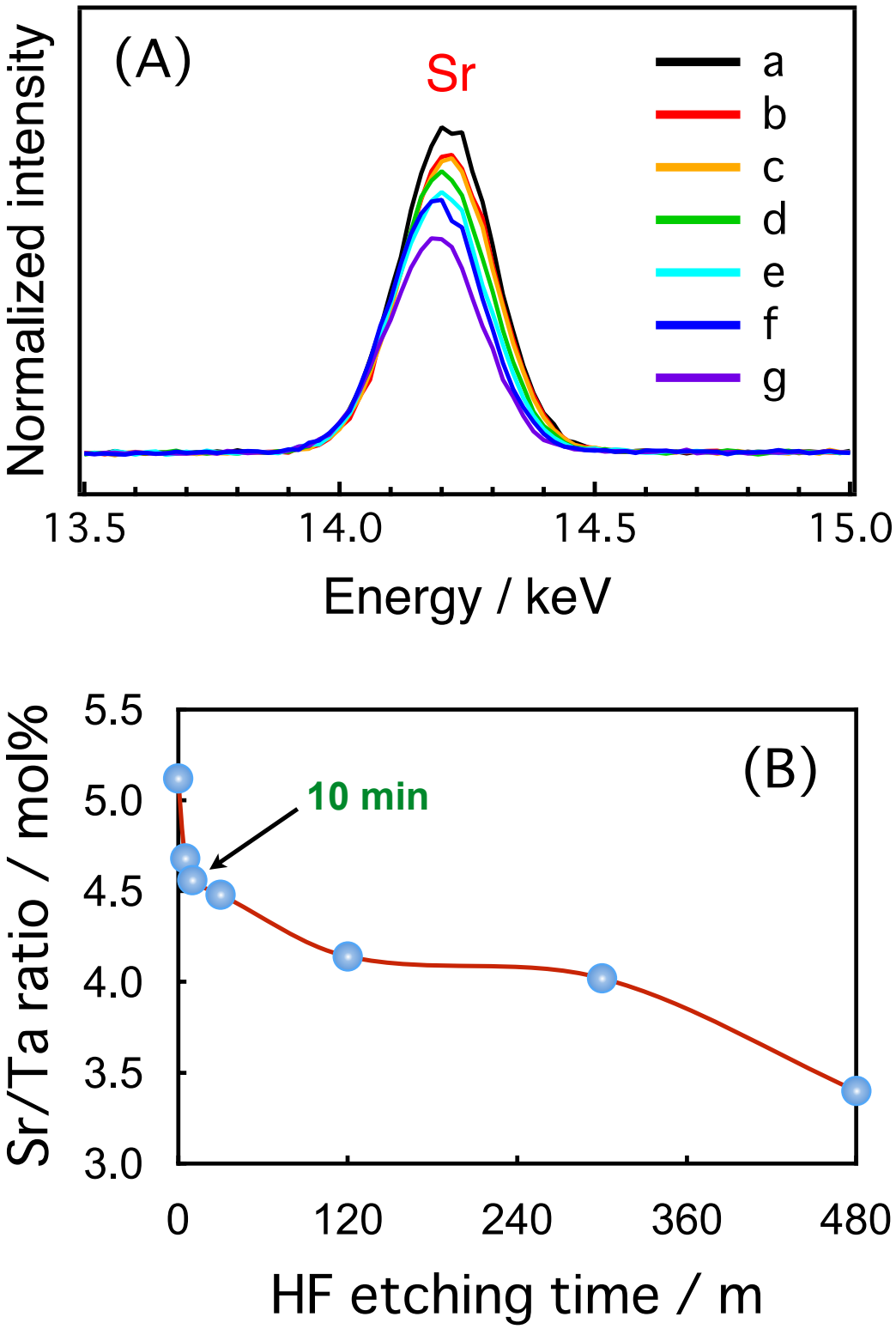

Figure 4.2 (A) X-ray fluorescence spectra of Sr-Kα emission in 5%Sr-NTO etched with HF for a: 0, b: 5 m, c: 10 m, d: 30 m, e: 120 m, f: 300 m, and g: 480 m. (B) Sr/Ta ratio was plotted as a function of etching time.

Surface composition was examined by XPS. **Figure 4.3(A,B)** show XPS spectra corresponding to Ta 4f and Sr 3d emissions. Before etching, 5%Sr-NTO produced double peaks with different spin-orbit couplings both in Ta 4f and Sr 3d emissions. The binding energies of the Ta 4f 7/2 and Sr 3d 5/2 states appeared respectively at 25.6 and 132.6 eV, which are consistent with results reported earlier.[2] As normalized to Ta 4f 7/2 emission intensity, Sr 3d emission was relatively reduced gradually with extended etching time in a range of 5-480m. Surface segregation of Sr thus was supported. Doublet peaks of Sr 3d emission lost the original feature and produced one broad band. It might be related to F^- anions adsorption on the surface.

Figure 4.3(C) shows XPS spectra corresponding to F 1s emission. Etched 5%Sr-NTOs presented fluorine peaks at 684.2 eV, as the same energy assigned to F 1s emission reported in earlier study.[3] It evidenced F adsorption on the surface of etched 5%Sr-NTOs particles. The intensity of F 1s emission increased by etching time was attributed to the increased surface/ bulk ratio on particles with reduced size because of etching, as observed by SEM in **Fig. 4.1**.

As F^- anions are more electronegative than O^{2-} anions, Sr^{2+} or Ta^{5+} cations bound to the F^- anions should present binding energies higher than those bound to the O^{2-} anions, as reported in the earlier study for fluorinated carbon[4] and silicon.[5] Deformation of Sr 3d emission with doublet peaks induced by etching was caused by surface adsorbed F bound to Sr. On a contrary, Ta 4f emission kept doublet peaks even when etched for 480 m. It explains most F anions were bound to Sr rather than Ta. With a lower electronegativity of Sr (1.0) than Ta (1.5), it is reasonable for F to be quickly bound to Sr before Ta.

To quantify Sr concentration on the surface during etching, Sr/Ta ratio was estimated from relative emission intensity of Sr 3d to Ta 4f. With average escape depth at 2.4 nm for Sr 3d and Ta 4f photoelectrons,[6] the kinetic energies of electrons at the two levels were similar at 1.3 and 1.4 keV, respectively. Thus estimated Sr concentration was plotted as a function of HF etching time, as shown in **Fig. 4.3(D)**. As a result, Sr concentration was reduced rapidly from 19.9 mol% to 17.0 mol% in 10 m-etching, and then gradually decreased to 12.4 mol% in 480 m-etching. The rapid and gradual reduction of Sr concentration exhibited a similar pattern to EDX results. Sr-rich shell was removed in etching for 10 m, leaving a core with Sr concentration gradient.

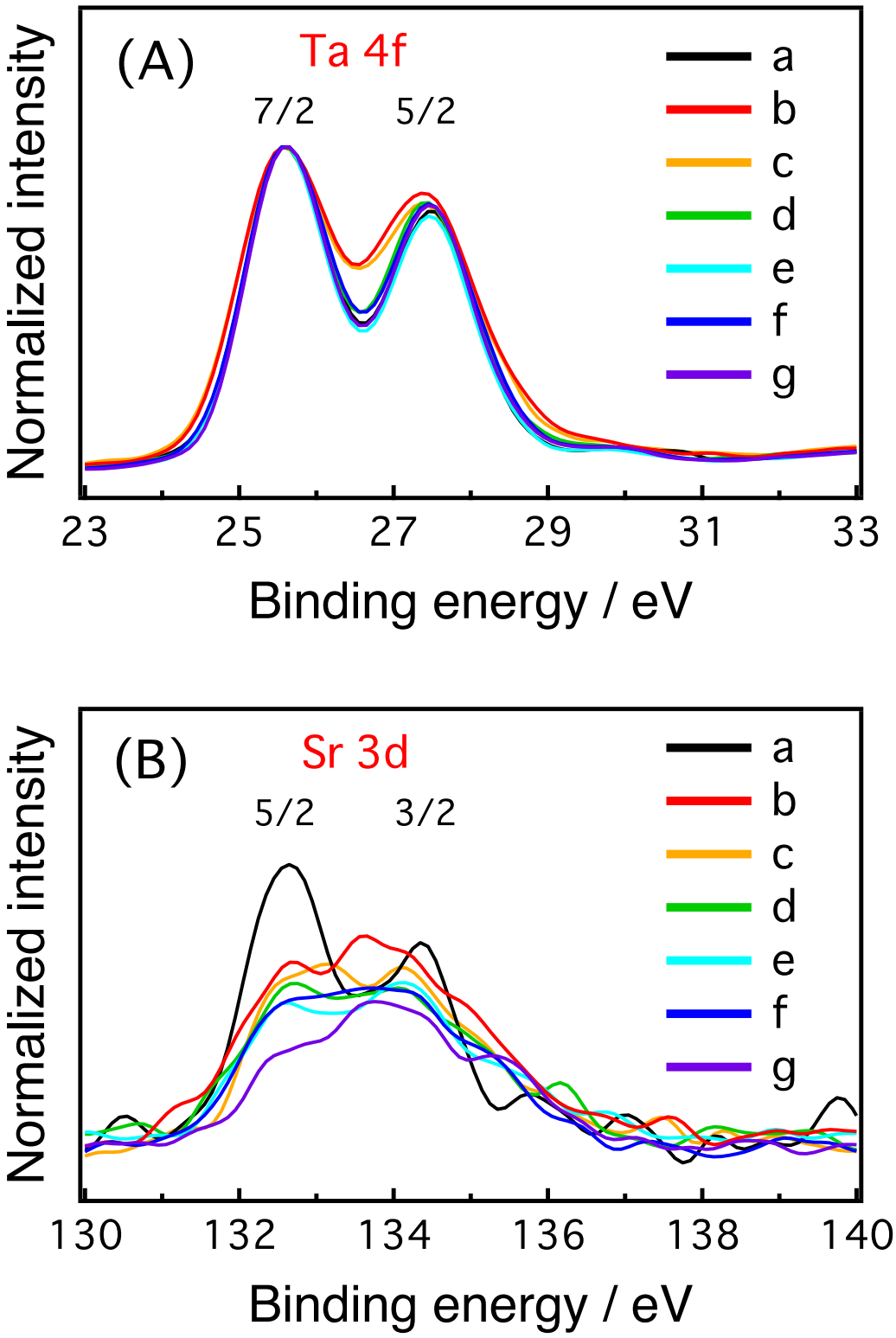

Figure 4.3 X-ray photoelectron spectra of 5%Sr-NTO etched for a: 0, b: 5 m, c: 10 m, d: 30 m, e: 120 m, f: 300 m, and g: 480 m. (A) Ta 4f emission, and (B) Sr 3d emission. The signal intensity was normalized relative to the Ta 4f 7/2 state.

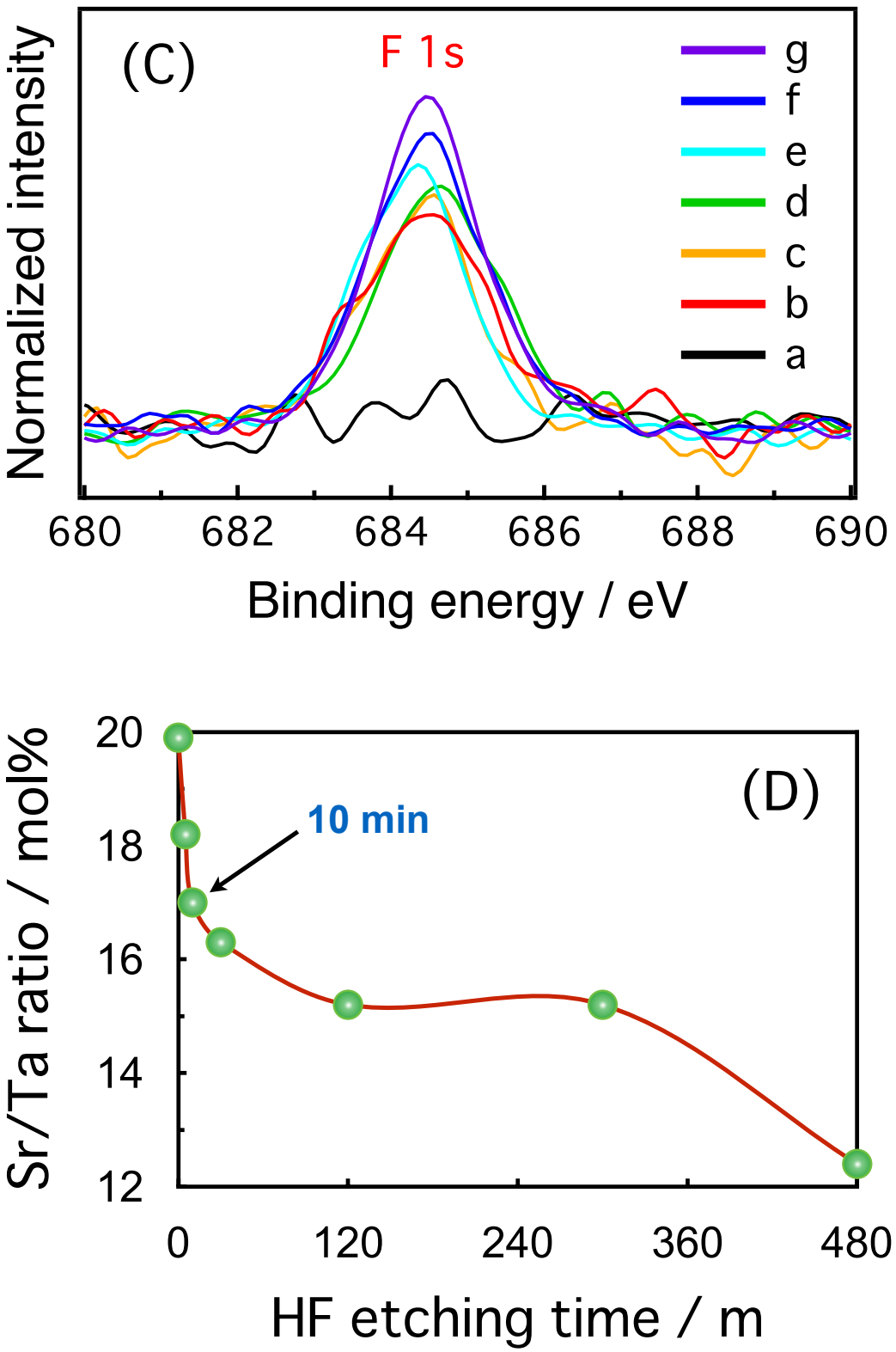

Figure 4.3 (C) F-1s emission spectra. (D) Sr/Ta ratio was plotted as a function of etching time.

In chapter 3, the presence of $NaTaO_3$-$Sr(Sr_{1/3}Ta_{2/3})O_3$ solid solution was proposed in Sr-NTO (SSM) in addition to core-shell structure model. The solid solution will lead to B-site doping of Sr. Change in concentration of Sr doped at B-sites induced by HF etching was examined by Raman spectroscopy.

Figure 4.4(A) shows Raman spectra of 5%Sr-NTO before and after etching. Unetched 5%Sr-NTO produced major Raman bands at 450, 500, and 620 cm^{-1}, being assigned to pristine NTO,[7] in addition to Raman bands at 760 and 860 cm^{-1}. All the spectra were normalized at 620 cm^{-1}. The intensities of the two bands at 760 and 860 cm^{-1} exhibited different sensitivities to etching time. The band at 760 cm^{-1} weakened for 5 m-etching (spectrum b) and completely disappeared for 10 m-etching (spectrum c). On the other hand, 860 cm^{-1} band intensity showed about 30 % reduction for 10 m-etching, followed with a gradual reduction for longer etching, as intensity ratio of 860/620 cm^{-1} band is shown in **Fig. 4.4(B)**. Even after etching for 480 m (spectrum g), the band was clearly visible.

Such a different response to etching time for the two bands are caused by the proposed core-shell structure in 5%Sr-NTO. The shell, removed upon etching for the first 10 m, contained two species; one species mainly produced Raman band at 760 cm^{-1}, and the other one resulted in the 860 cm^{-1} band. The core remained after removal of the shell contained only the latter species, producing 860 cm^{-1} band alone.

Here the two Raman bands should be assigned to the breathing vibrations of TaO_6 octahedra in $NaTaO_3$-$Sr(Sr_{1/3}Ta_{2/3})O_3$ solid solutions. Earlier studies about B-site doped perovskites $A(B_{1-x}B'_x)O_3$ reported the usual appearance of BO_6 breathing vibrations in a range of 780-850 cm^{-1}.[8,9] The two separated Raman bands at 760 and 860 cm^{-1} indicate that the TaO_6 octahedra were located in different environments, although their chemical identities are no clear. The peak wavenumber of the TaO_6 vibration may be sensitive to the local concentration of Sr doped at B-sites. As depicted in chapter 3, $Sr(Sr_{1/3}Ta_{2/3})O_3$, having extreme Sr concentration, produced intense Raman band at 810 cm^{-1}, which is -50 cm^{-1} different from 860 cm^{-1} band. In Sr-NTO (SSM), the 860 cm^{-1} band shifted to lower wavenumber with increased Sr concentration in, finally merged with 810 cm^{-1} band in $Sr(Sr_{1/3}Ta_{2/3})O_3$. Therefore in 5%Sr-NTO, the Sr-rich shell provided two different environments for TaO_6 octahedra induced by

different concentration of Sr at B-sites, and the core supplied unique environments with relatively small concentration of Sr at B-sites.

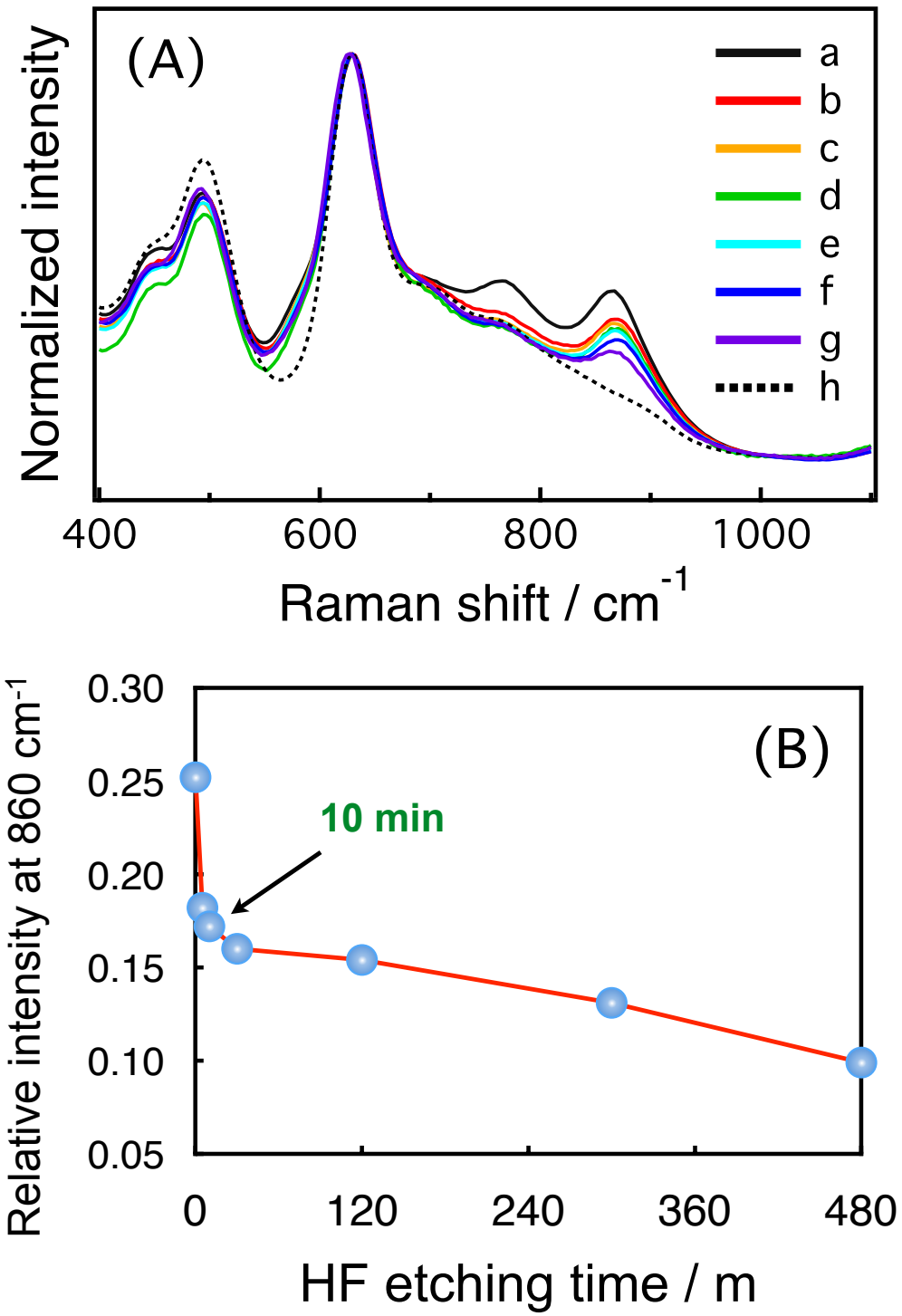

Figure 4.4 (A) Raman spectra of 5%Sr-NTO etched for a: 0, b: 5 m, c: 10 m, d: 30 m, e: 120 m, f: 300 m, and g: 480 m. The reference spectrum of NTO is shown as curve h. (B) Relative intensity of the band at 860 cm^{-1} as a function of etching time.

Etching induced reduction of B-site doped Sr concentration was also detected by XRD. **Figure 4.5** shows the shifts of a diffraction peak at 32.4°, corresponding to (110) peak of perovskite structured NTO.[10] Compared to pristine NTO (curve f), 5%Sr-NTO presented the peak smaller by 0.1° due to lattice expansion induced by B-site doping of Sr. As described in chapter 3, substitution of small Ta^{5+} with large Sr^{2+} resulted in gradual peak shift to small angels when NTO doped with Sr at B-sites.Increased etching time of 10-480 m induced peak shift to a higher degree by about 0.05°. It can be attributed to a smaller Sr concentration at B-sites in the inner core remaining in 5%Sr-NTO particles after etching.

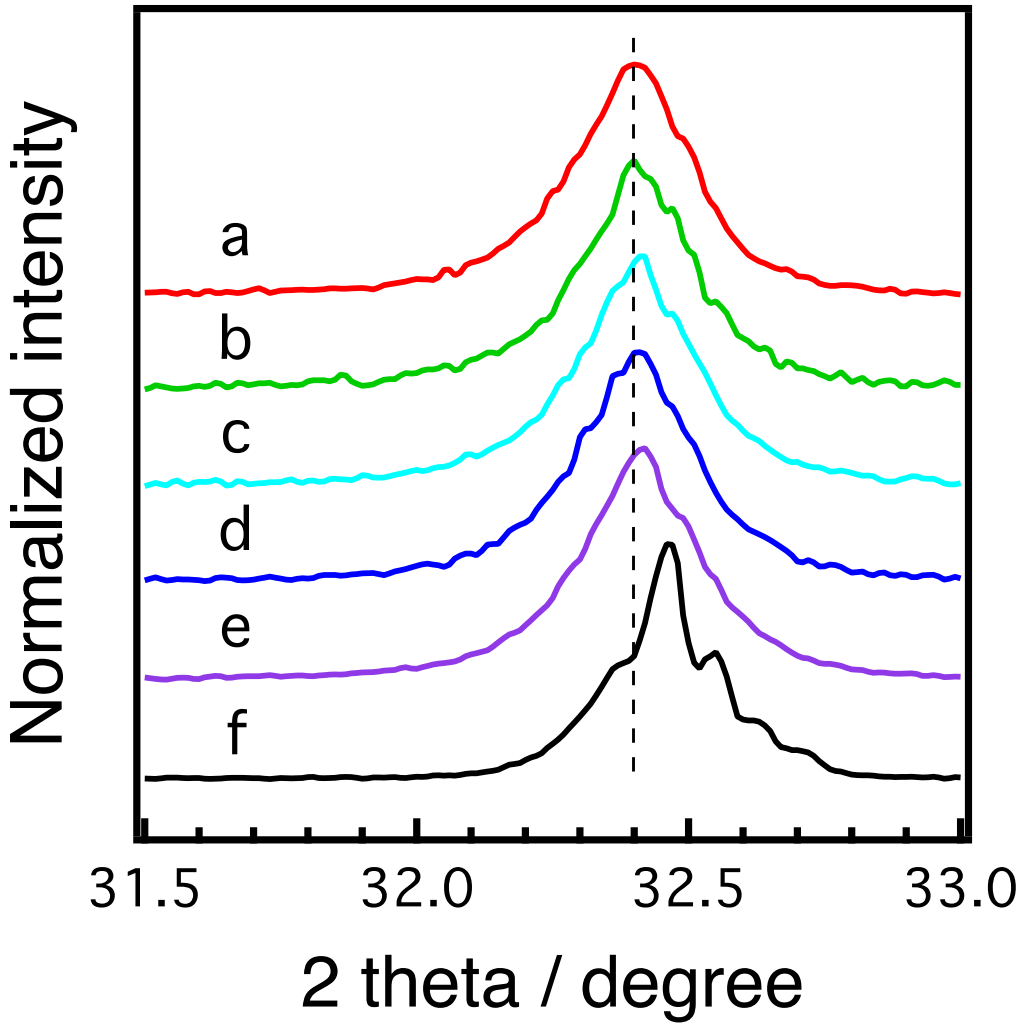

Figure 4.5 XRD (110) peaks of 5%Sr-NTO etched for a: 0, b: 10 m, c: 120 m, d: 300 m, and e: 480 m. The peak of reference NTO is shown as curve f.

Based on the results obtained from SEM, EDX, XPS, Raman, and XRD, the manner of Sr distribution in 5%Sr-NTO is pictured in **Fig. 4.6**. As discussed in chapter 3, 5%Sr-NTO was composed of $NaTaO_3$-$Sr(Sr_{1/3}Ta_{2/3})O_3$ solid solutions as well as Sr-NTO (SSM). Lattice mismatch between the two materials induced intense Sr segregation on particle surface to keep NTO lattices away from collapse. Ten-nanometer-length steps and terraces were formed on particle surface to correct lattice mismatch. The surface segregated Sr produced an interface of the Sr-poor core and Sr-rich shell. Simultaneous Raman bands appeared at 760 and 860 cm^{-1} due to intense Sr segregation provided complex environments for TaO_6 breathing vibration. The relatively small Sr concentration in the core induced single band at 860 cm^{-1}.

Etching for the first 10 m removed the shell, leaving the core exposed on the surface. The bulk and surface Sr concentration decreased accordingly. The fast reduction of Sr concentration suggests intense Sr concentration in the shell. Steps and terraces remained on particle surface indicate the correction of lattice mismatch began in the core. Etching for 120 m was required to eliminate steps and terraces completely. During etching of the core, bulk and surface Sr concentration decreased gradually, as well as 860 cm^{-1} Raman band intensity. The concentration gradient of Sr (total and B-site doped) was thus present in the core. Limited

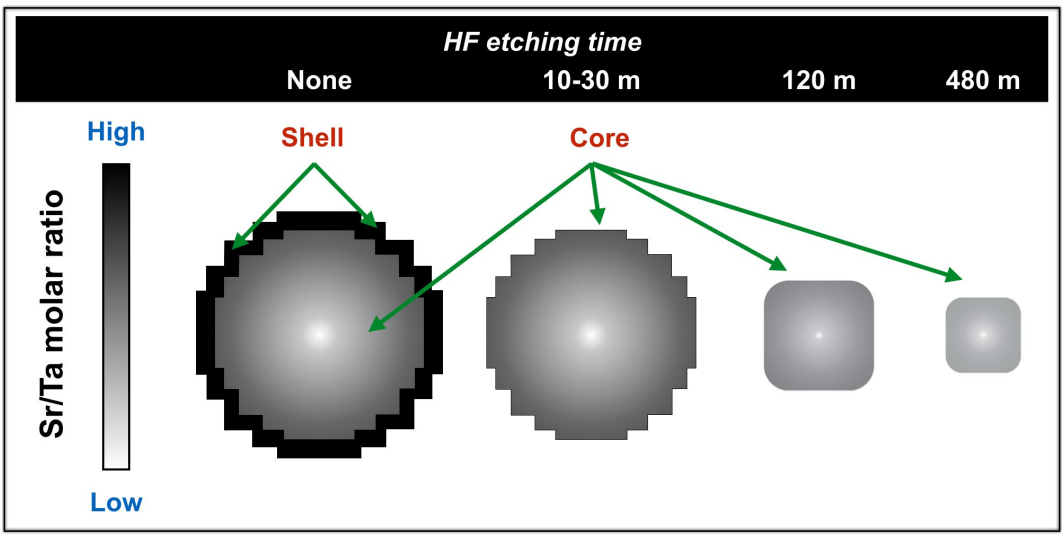

Figure 4.6 Schematic illustration of spatial distribution of Sr in 5%Sr-NTO is shown in combination of effect of etching

but true XRD shift to lower angle induced by etching supported the concentration gradient of Sr at B-sites.

Each role of the core or the shell in electron-hole recombination was investigated by UV-induced IR absorption spectroscopy. The change in IR absorbance induced by UV light has been used to evaluate the number of photoexcited electrons not yet recombined with holes in typical photocatalysts and photoelectrodes, such as $NaTaO_3$,[11,12] $SrTiO_3$,[13] TiO_2,[14-22] $LaTiO_2N$,[23] Ga_2O_3,[24] GaN,[25] $K_3Ta_3B_2O_{12}$,[26] Bi_2WO_6.[27]

Figure 4.7(A) shows UV-induced IR absorbance change of 5%Sr-NTO before and after etching. Unetched 5%Sr-NTO presented two components of absorbance; one showed a monotonic increase from 6000 cm^{-1} to 900 cm^{-1}, while the other is a broad band with a peak at 2000-2500 cm^{-1}. These two components are attributed to electron transitions in the conduction band (CB) and from shallow trap states to the CB, respectively.

The relative population of excited electrons in 5%Sr-NTO during etching was quantified by integrating IR absorbance change in a range of 6000-900 cm^{-1}. **Figure 4.7(B)** shows a plot of the integrated absorbance change of etched 5%Sr-NTO relative to that of pristine NTO as a function of etching time. Unetched 5%Sr-NTO showed integrated absorbance change, which is proportional to the steady-state population of photoexcited electrons, 132 times as NTO. During etching on the shell for 10 m, relative population of excited electrons increased by 40% to 185 times. On the other hand, longer etching mainly on the core reduced the electron population gradually, eventually, reaching to 16.1 times in 5%Sr-NTO/480m. It indicates the electrons and holes were excited in the core but recombined in the shell. With the shell removed from the core in 10 m etching, the recombination rate decreased, thereby the electron population increased accordingly.

According to Raman scattering, two components showing 760 and 860 cm^{-1} Raman bands were detected in the shell. Excessive Sr in the shell induced unexpected component referring to 760 cm^{-1}. With a thin depth of the shell, which was removed by etching for only 10 m, it is difficult to determine the structure producing 760 cm^{-1} band. However, the component indeed reduced electron population in the shell.

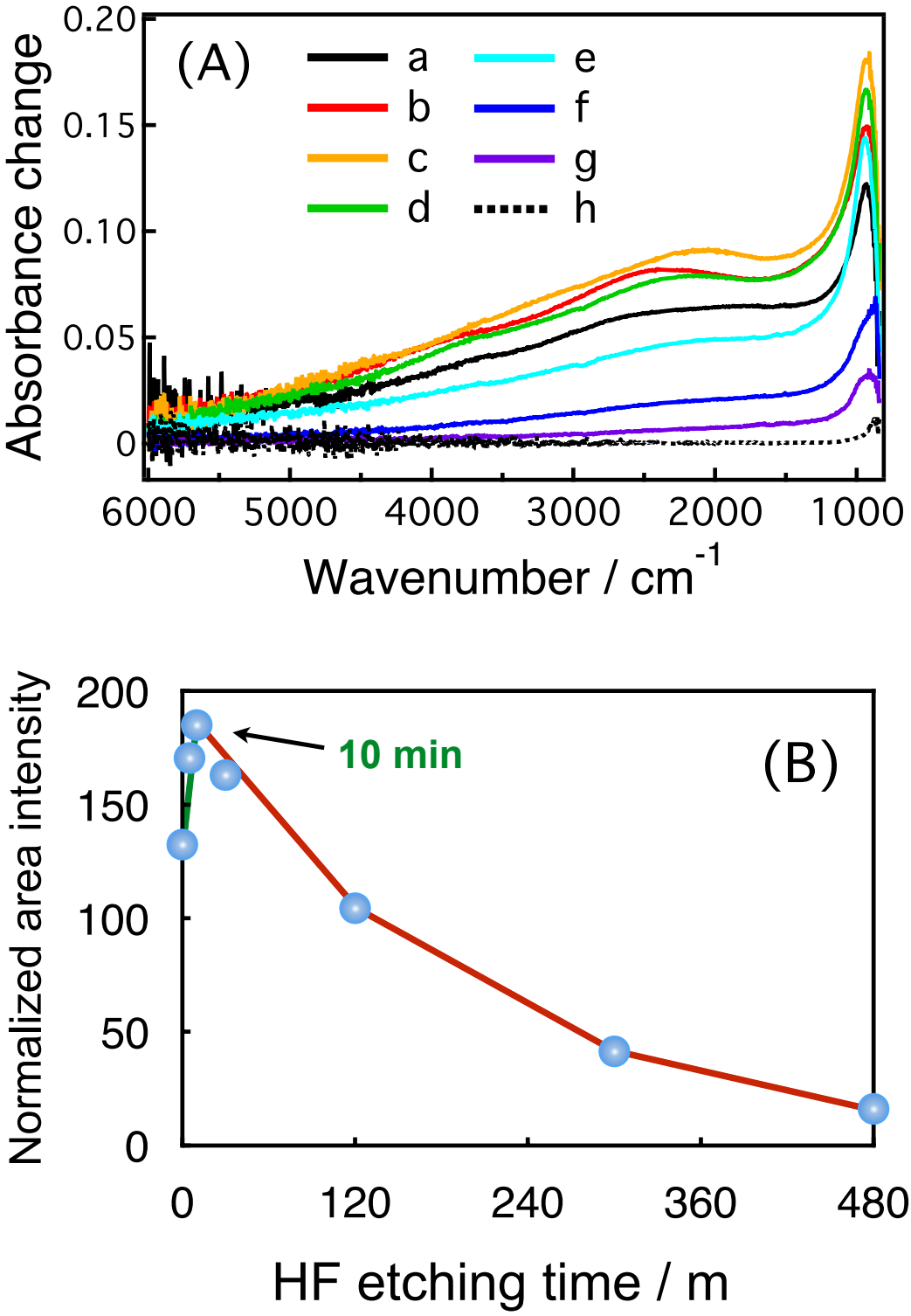

Figure 4.7 (A) Change in IR absorbance induced by UV irradiation of 5%Sr-NTO etched for a: 0, b: 5 m, c: 10 m, d: 30 m, e: 120 m, f: 300, and g: 480 m. The NTO spectrum is shown as dashed curve f. (B) Integrated absorbance change relative to that of NTO as a function of etching time.

Another issue with the effect of etching is the monotonic decrease of electron population during etching for 10-480 m. With the shell removed, the bare and unetched core, which appeared at an etching time of 10 min, exhibited the largest IR absorbance change. It is essential to investigate the decrease in electron population caused by the etching on the core.

On a possible reason for the reduced population of electrons during etching on the core is the accordingly decreased Sr concentration. However, the possibility was excluded. As presented in **Fig.4.2**, the bulk Sr concentration was 3.4 mol% in 5%Sr-NTO/480m. In chapter 3, the integrated IR absorbance change induced upon UV irradiation was plotted as a function of Sr concentration for Sr-NTO (SSM). Based on the plot, 3.4 mol% Sr-NTO directly prepared via SSM should produce electron population at about 150 times as that of pristine NTO. On the other hand, 5%Sr-NTO/480m with Sr concentration at 3.4 mol% produced only 16 times electron population. This apparent difference explains the Sr concentration reduced by etching played a limited role to the decreased electron population during etching on the core.

Here the author proposes that the concentration gradient of Sr doped at B-sites controls electron population in the core. As confirmed by EDX, XPS, and Raman scattering, the concentration of Sr doped at B-sites gradually decreased from outer core to inner core. The length of the concentration gradient is decided by the size of the core to grow. The Sr concentration gradient can lead to energy gradient of conduction band minimum. In an ideal $NaTaO_3$-$Sr(Sr_{1/3}Ta_{2/3})O_3$ solid solution, one out of four Sr cations should be located at B-sites to eliminate any vacancy defect. As the CB of NTO derives from Ta 5d orbitals,[28-30] the energy of CB minimum is sensitive to the concentration of Sr that replace Ta at B-sites. In Sr-NTO (SSM), indeed, the band gap energy was expanded by doping Sr at B-sites, as depicted in chapter 3.

Figure 4.8 shows possible electronic band structure of the core modified by Sr doping. The CB at the inner core was mainly derived from Ta 5d orbitals due to relatively low Sr concentration. With increased concentration of Sr doped at B-sites, CB minimum of the outer core was blue shifted to energy at less than -1 eV. The potential gradient formed in the core drives excited electrons transferring in a particular direction, probably from outer core to inner core. Meanwhile, energy of the valence band (VB) of the NTO should be maintained at 3 eV with or without Sr doping, since it is derived from O 2p orbitals.[28-30] The excited

electrons transferred via potential gradient were, hence, separated from holes that left in the VB. Consequently, the electron-hole recombination was restricted. Electron-hole separation prompted by potential gradient in crystal can also be seen in $SrTiO_3$,[31] $KTiO_3$,[32] and TiO_2.[33]

With this interpretation, the population of excited electrons reached a maximum at 2%Sr-NTO (SSM), as the reason was unknown in chapter 3, can also be explained. Until doping of Sr at 2 mol%, the core was mainly produced. Increased Sr concentration in a range of 0-2 mol% contributed to the more steep degree of concentration gradient of Sr at B-sites. The steep gradient degree raised potential energy gradient degree of CB minimum to drive more efficiently the electron-hole separation. Accordingly, electron population increased with Sr concentration. On the other hand, excessive doping of Sr at more than 2 mol% not only produced the shell on top of the core but also reduce the degree of Sr concentration gradient in the core. With enough amount, the Sr naturally distributed evenly in the core to weaken the degree of gradient. The limited potential gradient of CB drives little separation of electrons and holes. The separation was also hindered by the growing shell. Consequently, the excited-electron population decreased gradually with Sr concentration in this range.

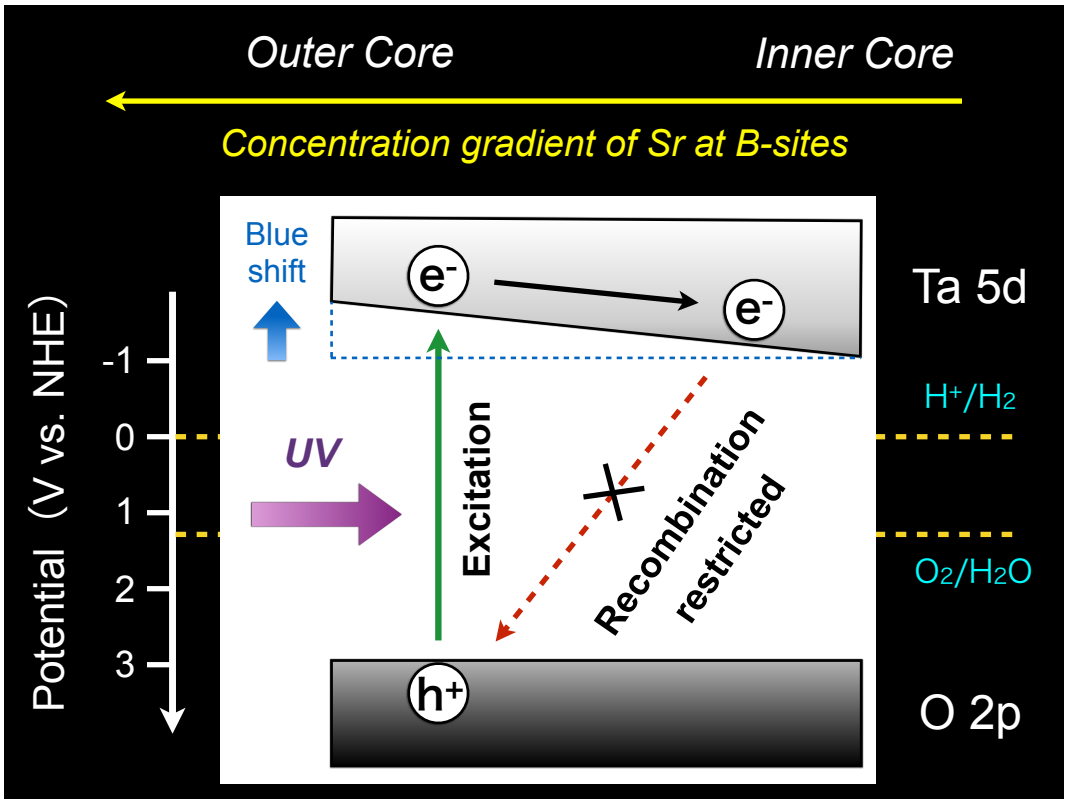

Figure 4.8 Mechanism of electron-hole separation driven by potential energy gradient of conduction band.

4.3.2 Effect of surface adsorbed F^- on electron-hole recombination

To supports the proposed assumption that electrons and holes were excited in the core and recombined in the shell, the effect of F^- anions adsorbed on the surface should be made clear. This subsection introduces two methods that used to examine possible roles of adsorbed F to photoexcited electrons. As one method, heating was applied to vaporize absorbed F^- anions into F_2 to check the change in electron-hole recombination before and after F^- removal. Like the other one, pristine NTO was etched with HF solution to examine the effect of surface adsorbed F^- anions.

In an earlier study about F-adsorbed anatase TiO_2, a fluorine-free surface was obtained when heated at 873 K.[34] In the present study, 5%Sr-NTO/30m was heated at 773 K for 10 h in the air trying to remove F^- anions adsorbed on the surface. Presence or absence of F on the surface was confirmed by XPS. **Figure. 4.9(A)** shows XPS spectra corresponding to F 1s emission of 5%Sr-NTO/30m before and after heating. After heating, surface adsorbed F^- anions disappeared completely, as expected.

Figure 4.9(B) shows UV-induced IR absorbance change of 5%Sr-NTO/30m presence or absence of F. With F removal, 5%Sr-NTO/30m presented an abrupt decrease in IR absorbance change, showing almost the same level as pristine NTO added as a reference. On the other hand, 5%Sr-NTO with etching showed much stronger IR absorbance change than NTO. The unexpected decrease induced by heating in 5%Sr-NTO/30m may be due to lattice structure change occurred during heating.

Figure 4.9(C) shows Raman spectra of 5%Sr-NTO/30m with or without F. The band at 860 cm^{-1} weakened when heated, producing a new band at 810 cm^{-1}. This spectral transformation evidenced modification of lattice structure under heating. Considering the 5%Sr-NTO was synthesized via SSM at 1423 K, the 773 K used to remove F was not able to provide enough energy for lattice structure change. However, F removal may be the reason. The broad spectrum of the Sr 3d emission shown in **Fig. 4.3(B)** suggests F^- anions were mainly bound to Sr^{2+} cations. Desorption of F^- in the form of F_2 should leave excess Sr^{2+} cations and electrons on the surface. Under heating, these excess Sr produced a structure similar to $Sr(Sr_{1/3}Ta_{2/3})O_3$, which also presented 810 cm^{-1} Raman band. Thus the reduced IR absorbance change upon

heating, was not only related to desorption of F but also related to lattice structure change. As a result, the single role of F to excited electrons was not clarified in this way.

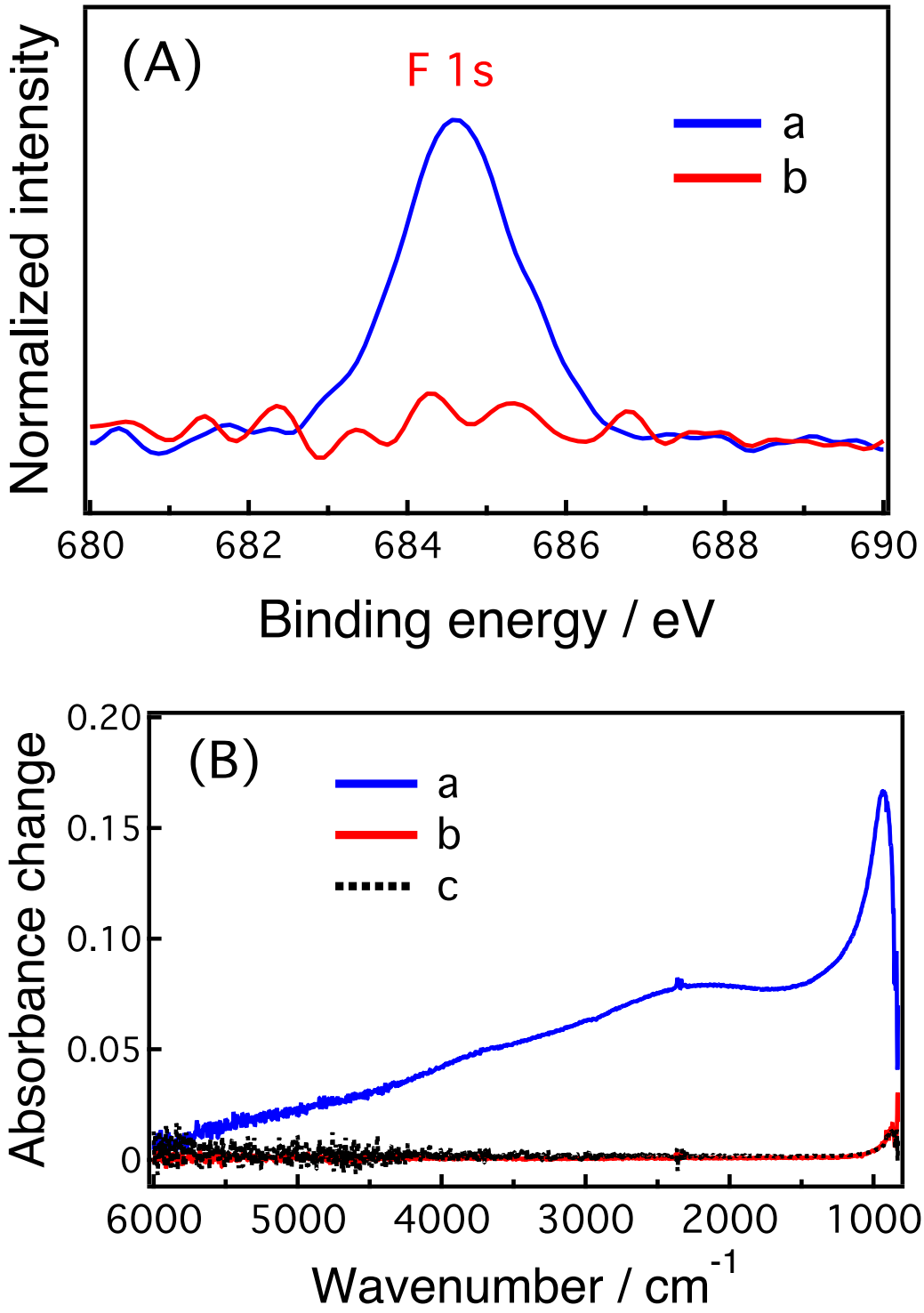

Figure 4.9 Characterization result of a: 5%Sr-NTO/30m, b: 5%Sr-NTO/30m heated at 773 K for 10 h, and c: NTO. (A) XPS spectra. (B) UV-induced IR absorbance change.

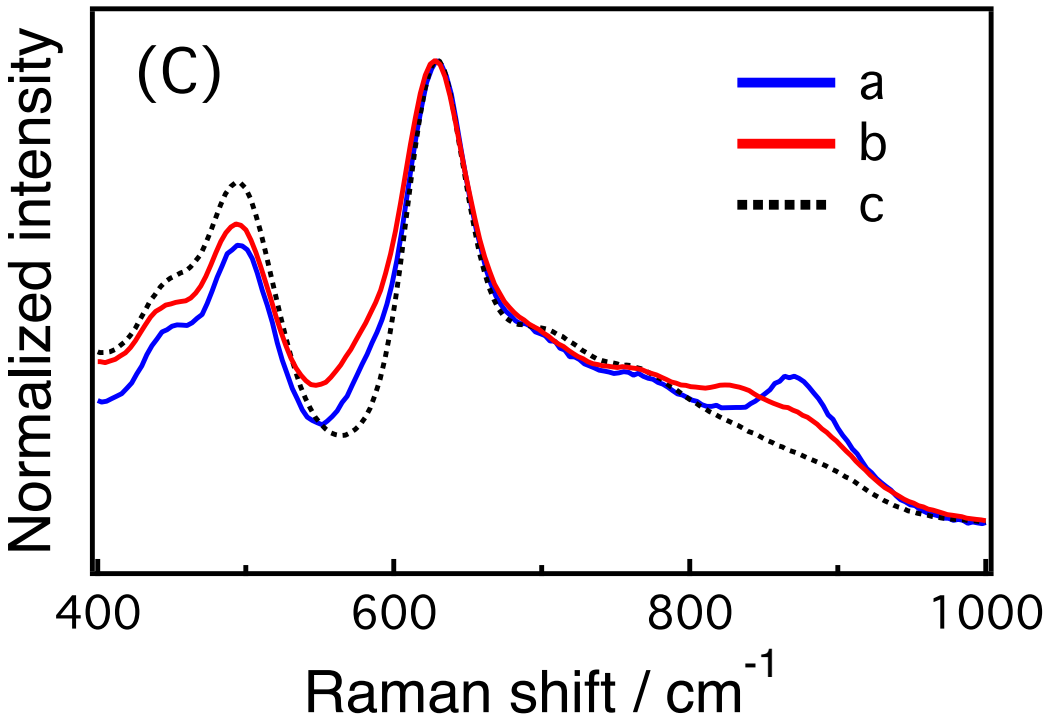

Figure 4.9(C) Raman spectra.

Since the removal of F^- anions accompanied structural change, heating is not an efficient method to study the effect of F. With HF etching, Sr segregation on the surface of Sr-NTO particles was dissolved, thereby the Sr concentration fluctuated. Instead of Sr-NTO, which has inhomogeneous distribution, pristine NTO was used at base etching material. Without Sr distribution, the etching should not change the composition of NTO particles.

NTO (SSM) was etched with HF for 10 and 300 m. **Figure 4.10(A)** shows XPS spectra of NTO before and after etching. F 1s emission intensity increased drastically after etching. Successful F adsorption on the surface was thus obtained by etching.

The population of photoexcited electrons was detected by UV-induced IR absorption spectroscopy, as shown in **Fig. 4.10(B)**. The IR absorbance change was insensitive to the presence or absence of F adsorption. Hence, the effect of F^- anions on photoexcited electrons is limited. The increase and decrease of IR absorbance detected in 5%Sr-NTO during etching were intrinsic property of Sr-NTO.

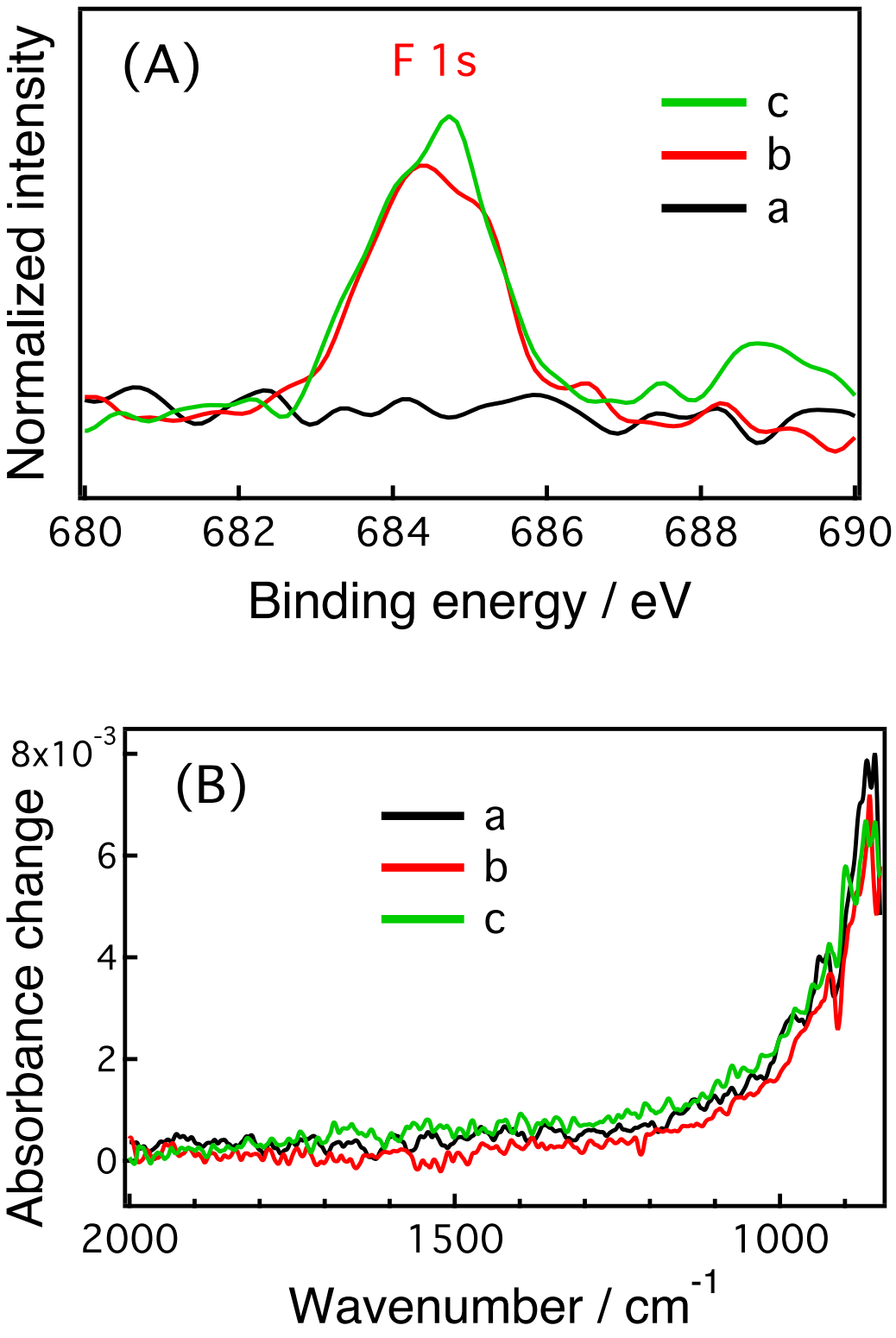

Figure 4.10 (A) XPS spectra, (B) UV-induced IR absorbance change of a: NTO, b: NTO/10m, and c: NTO/300m.

4.3.3 Response to HF etching on 1%Sr-NTO and 8%Sr-NTO

In 5%Sr-NTO, the shell was removed at 10 m-etching. Sr concentration and population of excited electrons decreased consistently with the removal of the shell. Hence the electrons and holes were believed recombined in the shell. The supposition was supported in this subsection by etching 1%Sr-NTO and 8%Sr-NTO. Since the electron population increased monotonically with Sr concentration in a range of 0-2 mol%, the shell was probably not formed yet in 1%Sr-NTO. On the other hand, the shell should grow on top of the core in 8%Sr-NTO, which has even higher Sr concentration than 5%Sr-NTO. In these two photocatalysts, the effect of the presence or absence of the shell can be separately examined. 8%Sr-NTO and 1%Sr-NTO were etched with HF solution for 10 m., respectively.

In 8%Sr-NTO, the presence of the shell was confirmed by EDX and Raman spectroscopy. **Figure 4.11(A)** shows EDX of Sr-Kα emission, whose intensity was normalized to that of Ta-Lα emission. During etching for 10 m, Sr concentration decreased from 8.3 to 7.5 mol%. This sharp reduction in Sr concentration suggests Sr segregation in the shell was dissolved. **Figure 4.11(B)** shows Raman spectra of 8%Sr-NTO before and after etching in addition to pristine NTO shown as a reference. 760 cm^{-1} Raman band, corresponding to the Sr-rich shell disappeared after etching. 8%Sr-NTO was thus composed of core-shell structure. With the shell removed by etching, the UV-induced IR absorbance change increased by about 20%, as shown in **Fig. 4.11(C)**. It supports the electrons and holes were recombined in the shell.

On the other hand, bulk Sr concentration in 1%Sr-NTO was almost the same at 1.0 mol% before and after etching, as shown in **Fig. 4.12(A)**. In Raman scattering as shown in **Fig. 4.12(B),** the absence of 760 cm^{-1} band in unetched 1%Sr-NTO indicates the absence of the shell. The core was mainly dissolved by etching. With smooth Sr concentration gradient in the core, etching did not dissolve so much Sr. Consequently, the bulk Sr concentration was insensitive to etching. In **Fig.4.12(C)**. The decreased electron population by 30% during etching on the core supports the electrons and holes were excited in the core, as proposed for 5%Sr-NTO.

Selective study about roles of the shell and core to electron-hole recombination in 8%Sr-NTO and 1%Sr-NTO led to the same conclusion as obtained from etching of 5%Sr-NTO that the electrons and holes were excited in the core and recombined in the shell.

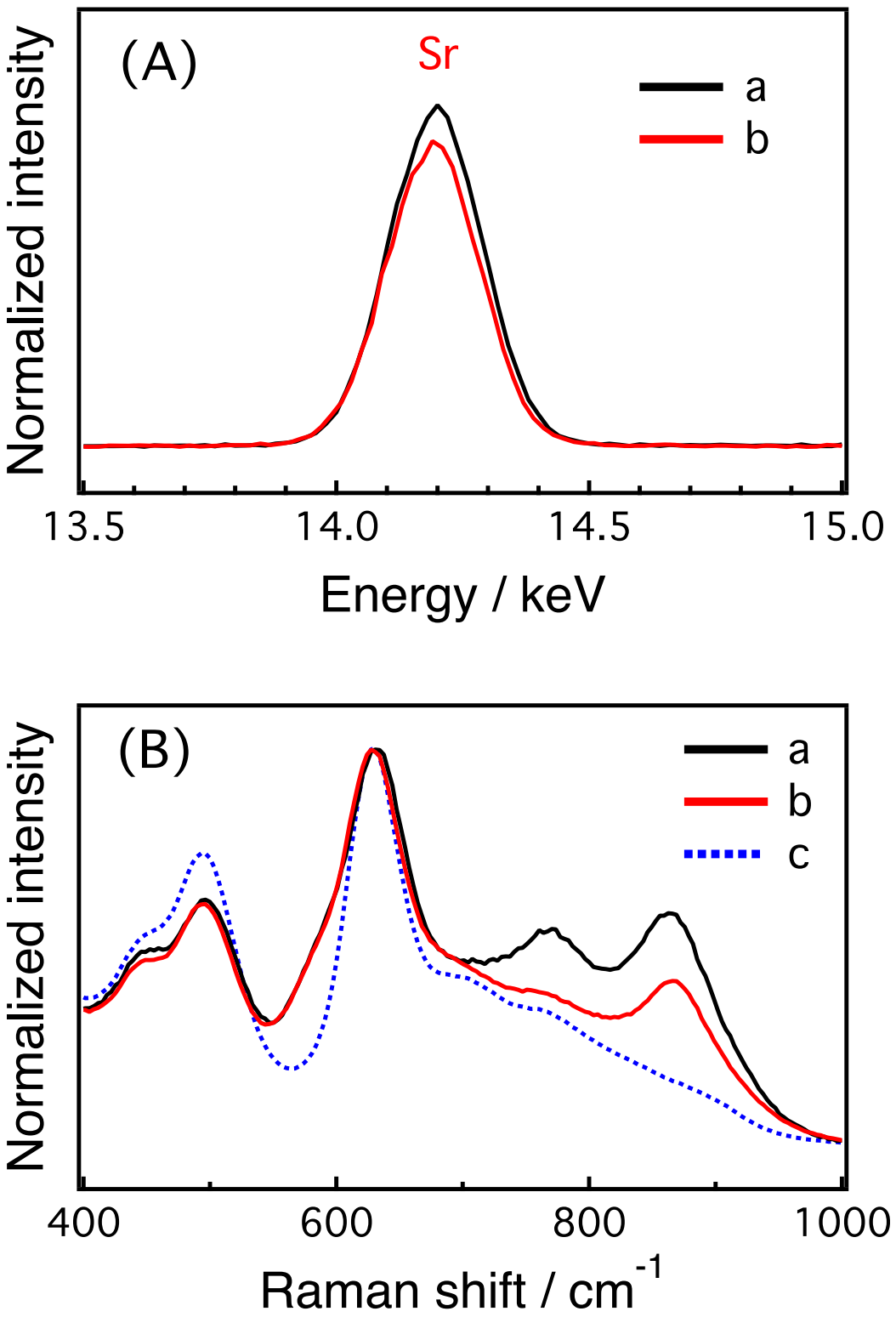

Figure 4.11 Characterization results of a: 8%Sr-NTO, b: 8%Sr-NTO/10m, and c: NTO. (A) X-ray fluorescence spectra of Sr-Kα emission, (B) Raman spectra.

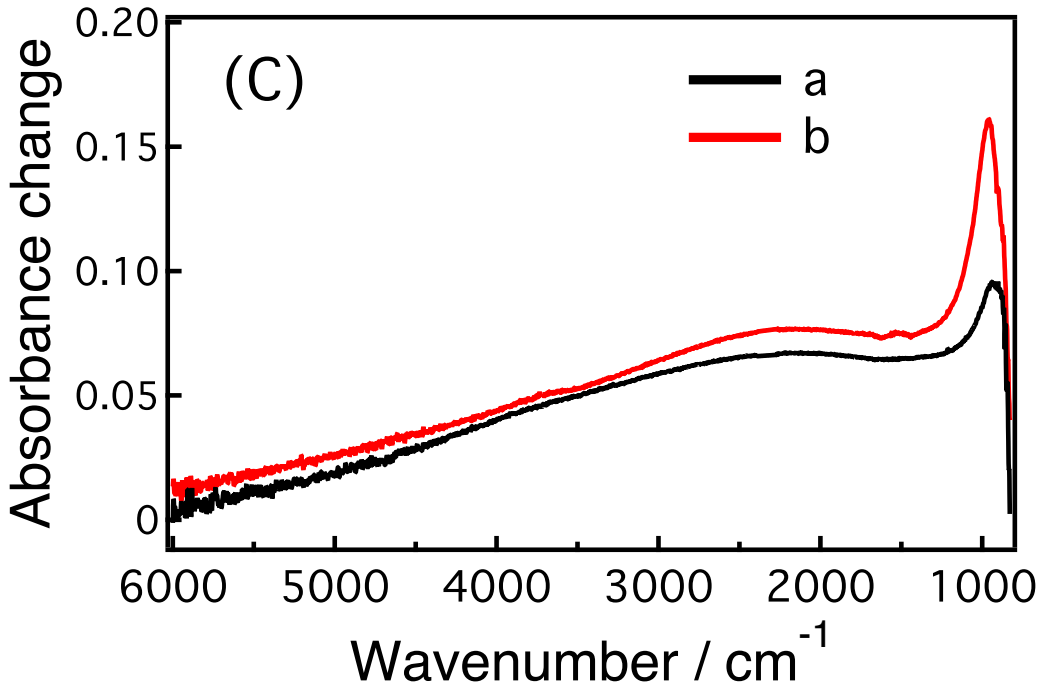

Figure 4.11 (C) UV-induced IR absorbance change of a: 8%Sr-NTO, and b: 8%Sr-NTO/10m.

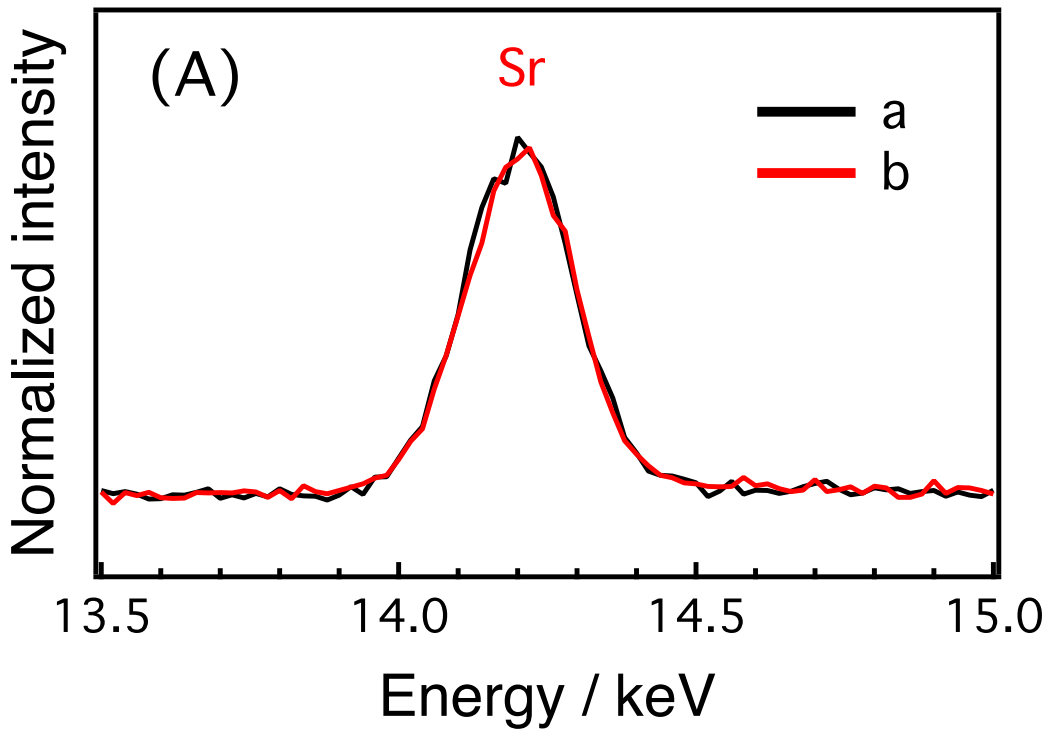

Figure 4.12 (A) X-ray fluorescence spectra of Sr-Kα emission of a: 8%Sr-NTO, b: 8%Sr-NTO/10m.

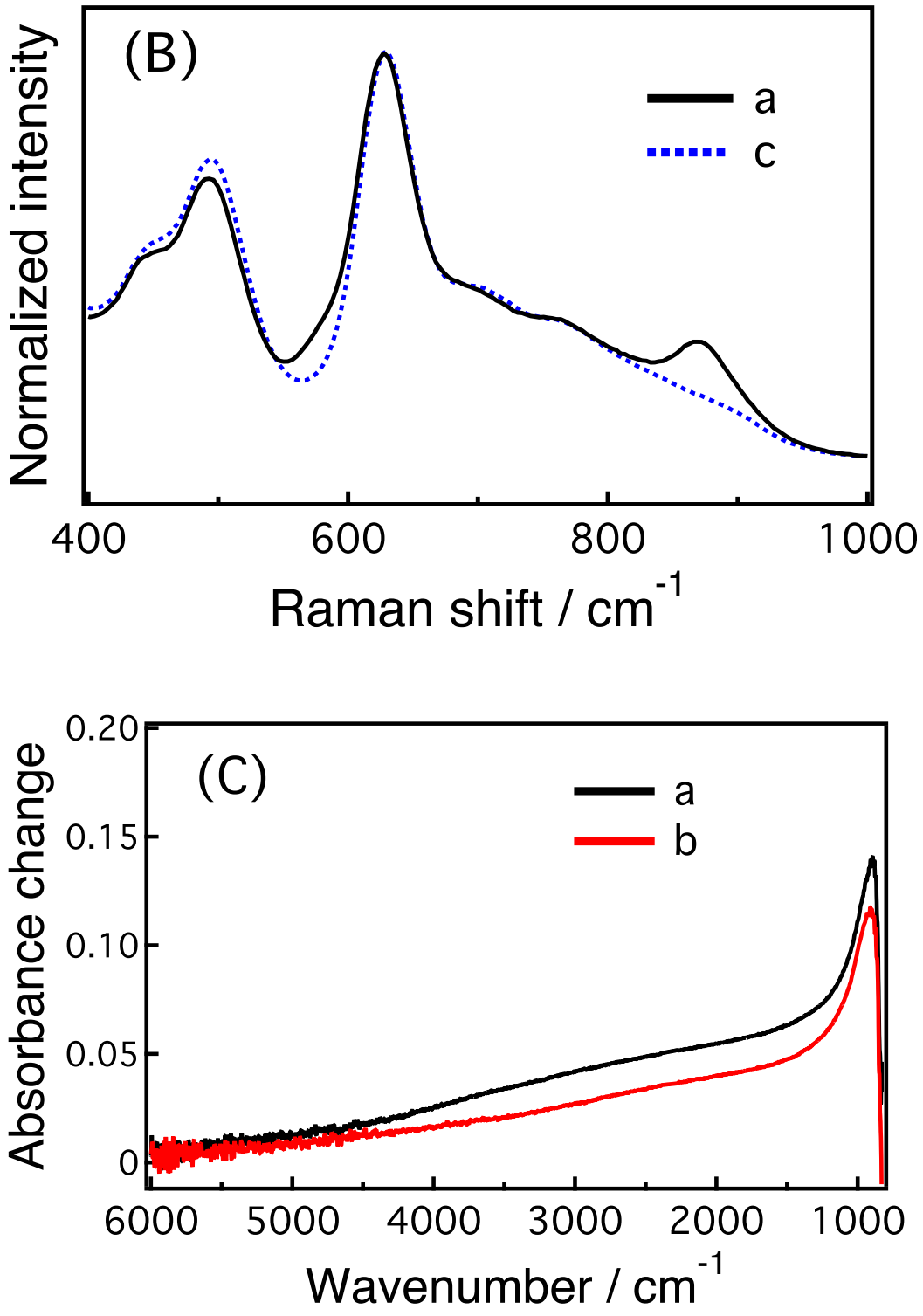

Figure 4.12 Characterization results of a: 1%Sr-NTO, b: 1%Sr-NTO/10m, and c: NTO. (B) Raman spectra, (C) UV-induced IR absorbance change.

4.4 CONCLUSION

1) In $NaTaO_3$ doped with 5 mol% Sr, a Sr-rich shell formed on top of a Sr-poor core. The shell, which produced two extra Raman bands at 760 and 860 cm^{-1}, was removed by HF etching for 10 m. Sr concentration decreased abruptly with the removal of the shell. The population of photoexcited electrons increased by 40% accordingly. On the other hand, during etching on the core for 10-480 m, the Sr concentrations in the bulk and on the surface both decreased gradually. Both the 860 cm^{-1} Raman band, representing Sr doped at B-sites, and the population of photoexcited electrons decreased accordingly. These results indicate the electrons and holes were excited in the core and recombined in the shell. In core, concentration gradient of Sr doped at B-sites was assumed to restrict recombination of electrons and holes. While in the shell, complex patterns of Sr doping at B-sites induced by serious Sr concentration might accelerate electron-hole recombination.

2) F^- anions were adsorbed on the surface of the photocatalysts during etching. The possible contribution of the adsorbed fluorine to the electron-hole recombination was examined and excluded by comparison of the properties of pristine $NaTaO_3$ etched with HF solution.

3) Each role to electron-hole recombination of the shell and core was studied by etching $NaTaO_3$ doped with Sr at 8 mol% and 1 mol%, respectively. With Sr doped at 1 mol%, the shell was not formed yet. Etching mainly dissolved the core layer and the electron population was reduced consistently. On the other hand, doping of 8 mol% Sr induced the shell to grow. Removal of the shell by etching enhanced electron population. Again, electrons and holes were excited in the core and recombined in the shell.

4.5 REFERENCE

(1) Rodriguez, M. H.; Rosales, G. D.; Pinna, E. G.; Suarez, D.S. *Hydrometallurgy* **2015**, *156*, 17-20.

(2) Atuchin, V. V.; Grivel, J-C.; Zhang, Z. *Chem. Phys.* **2009**, *360*, 74-78.

(3) Osaka, A.; Himei, Y.; Nanba, T.; Miura, Y. *Bull. Inst. Chem. Res.* **1994**, *72*, 153-159.

(4) Schmidt, S.; Greczynski, G.; Goyenola, C.; Gueorguiev, G.K.; Czigany, Zs.; Jensen, J.; Ivanov, I.G.; Hultman, L. *Surf. Coat. Technol*. **2011**, *206*, 646-653.

(5) Pereira, J.; Pichon, L.E.; Dussart, R.; Cardinaud, C.; Duluard, C.Y.; Oubensaid, E.H.; Lefaucheux, P.; Boufnichel, M.; Ranson, P. *Appl. Phys. Lett*. **2009**, *94*, 071501.

(6) Ertl, G.; Küppers, J. *Wiley-VCH Verlag.* **1986**, p. 7.

(7) Teixeira, N. G.; Dias, A.; Moreira, R. L. *J. Euro. Ceram. Soc.* **2007**, *27*, 3683-3686.

(8) Siny, I. G.; Tao, R.; Katiyar, R. S.; Guo, R.; Bhalla, A. S. *J. Phys. Chem. Solids* **1998**, *59*, 181-195.

(9) Zheng, H.; Reaney, I. M.; Csete de Györgyfalva, G. D. C.; Ubic, R.; Yarwood, J.; Seabra, M. P.; Ferreira, V. M. *J. Mater. Res.* **2004**, *19*, 488-495.

(10) Ahtee, M.; Unonius, L. Acta Crystallogr., Sect. A: Cryst. Phys., Diffr., Theor. Gen. *Crystallogr.* **1977**, *33*, 150−154.

(11) Yamakata, A.; Ishibashi, T.; Kato, H.; Kudo, A.; Onishi, H. *J. Phys. Chem. B* **2003**, *107*, 14383-14387.

(12) Maruyama, M.; Iwase, A.; Kato, H.Kudo, A.Onishi, H. *J. Phys. Chem. C* **2009**, *113*, 13918-13923.

(13) Furuhashi, K.; Qingxin, J.; Kudo, A.; Onishi, H. *J. Phys. Chem. C* **2013**, *117*, 19101-19106.

(14) Yamakata, A.; Ishibashi, T.; Onishi, H. *Chem. Phys. Lett.* **2001**, *333*, 271-277.

(15) Szczepankiewicz, S. H., Moss, J. A., Hoffmann, M. R. *J. Phys. Chem. B* **2002**, *106*, 2922-2927.

(16) Yoshihara, T.; Katoh, R.; Furube, A.; Tamaki, Y.; Murai, M.; Hara, K.; Murata, S.; Arakawa, H.; Tachiya, M. *J. Phys. Chem. B* **2004**, *108*, 3817-3823.

(17) Warren, D. S.; McQuillan, A. J. *J. Phys. Chem. B* **2004**, *108*, 19373-19379.

(18) Panayotov, D. A.; Burrows, S. P.; Morris, J. R. *J. Phys. Chem. C* **2012**, *116*, 4535-4544.

(19) Amano, F.; Nakata, M.; Asami, K.; Yamakata, A. *Chem. Phys. Lett.* **2013**, *579*, 111-113.

(20) Maeda, A.; Ishibashi, T. *Chem. Phys.* **2013**, *419*, 167-171.

(21) Shen, S.; Wang, X.; Chen, T.; Zhaochi, F.; Li, C. *J. Phys. Chem. C* **2014**, *118*, 12661-12668.

(22) Sezen, H.; Buchholz, M.; Nefedov, A.; Natzeck, C.; Heissler, S.; Di Valentin, C.; Wöll, C. *Sci. Rep.* **2014**, *4*, 3808.

(23) Yamakata, A.; Kawaguchi, M.; Nishimura, N.; Minegishi, T.; Kubota, J.; Domen, K. *J. Phys. Chem. C* **2014**, *118*, 23897-23906.

(24) Wang, X.; Xu, Q.; Li, M.; Shen, S.; Wang, X.; Wang, Y.; Feng, Z.; Shi, J.; Han, H.; Li, C. *Angew. Chem. Int. Ed.* **2012**, *51*, 13089-13092.

(25) Yamakata, A.; Yoshida, M.; Kubota, J.; Osawa, M.; Domen, K. *J. Am. Chem. Soc.* **2011**, *133*, 11351-11357.

(26) Ikeda, T.; Fujiyoshi, S.; Kato, H.; Kudo, A.; Onishi, H. *J. Phys. Chem. B* **2006**, *110*, 7883-7886.

(27) Amano, F.; Yamakata, A.; Nogami, K.; Osawa, M.; Ohtani, B. *J. Phys. Chem. C* **2011**, *115*, 16598-16605.

(28) Choi, M.; Oba, F.; Tanaka, I. *Phys. Rev. B* **2008**, 78, 014115 (8 pages).

(29) Kato, H.; Kobayashi, H.; Kudo, A. *J. Phys. Chem. B* **2002**, *106*, 12441-12447.

(30) Wang, H.; Wu, F.; Jiang, H. *J. Phys. Chem. C* **2011**, *115*, 16180-16186.

(31) Ueno, K.; Inoue, I.H.; Akoh, H.; Kawasaki, M.; Tokura, Y.; Takagi, H. *Appl. Phys. Lett.* **2003**. *83*. 1755-1758.

(32) Ueno, K.; Inoue, I.H.; Yamada, T.; Akoh, H.; Tokura, Y.; Takagi, H. *Appl. Phys. Lett.* **2004**. *84*. 3726-3728.

(33) Li, Ailong.; Wang, Z.; Yin, H.; Wang, S.; Yan, P.; Huang, B.; Wang,X.; Li, R.; Zong, X.; Han, H.; Li, C. *Chem. Sci.* **2016**, *7*, 6076-6082.

(34) Yang, H. G.; Sun, C. H.; Qiao, S. Z.; Zou, J.; Liu, G.; Smith, S. C.; Cheng, H. M.; Lu, G. Q. *Nature* **2008**, *453*, 638-641.

Chapter 5

$NaTaO_3$ doped with Sr via MSM

5.1 INTRODUCTION

As carefully stated in chapter 4, radial distribution of Sr in $NaTaO_3$ played a key role to separating photoexcited electrons from holes. The Sr-doped $NaTaO_3$ prepared via SSM was composed of a core-shell structure. Electrons and holes were excited in the core and recombined in the shell. In the core, Sr concentration gradient was believed to drive electron-hole separation, since the electron population decreased gradually during etching on the core.

However, etching on the core also reduced Sr concentration. During etching on the core, the Sr concentration and the Sr concentration gradient length (radial distribution of Sr) were both changed. With coexistence of these two parameters, it is not strict to say the radial distribution alone controls the electron-hole recombination. Therefore, in this chapter, a deeper study was designed to selectively examine the effect of the radial distribution of Sr on the electron-hole recombination.

In Sr-doped $NaTaO_3$ prepared via SSM, as described in the previous chapters, Sr tended to segregate on the surface of photocatalyst particles. If there is a way to distribute Sr homogeneously in $NaTaO_3$ particles with fixed Sr concentration, it is possible to study the effect of the radial distribution of Sr alone. A main breakthrough of this chapter was the successful synthesis of various Sr-doped $NaTaO_3$ photocatalysts with fixed Sr concentration but having the different radial distribution of Sr.

During SSM synthesis of Sr-doped $NaTaO_3$ with heating at 1423 K, starting materials providing needed cations and anions are in the form of Na_2O (m.p. = 1,405 K), Ta_2O_5 (m.p. = 2,145 K), and SrO (m.p. = 2,804 K). Relatively high melting point (m.p.) of SrO made Sr^{2+} cations difficult to penetrate into the bulk of $NaTaO_3$ particles upon heating at 1423 K, due to the incomplete melting of SrO. The three ways to realize homogeneous distribution of Sr in $NaTaO_3$ are to increase the heating temperature, extend the periods of heating time, and reduce the m.p. of SrO. Considering overheating temperature brings defects of oxygen anions in the metal oxide, it is more reasonable to reduce the m.p. of SrO and extend the heating time.

The author came up with another synthesis method, which is the molten salt method (MSM), to realize the two conditions. In MSM, salt with low melting point is usually used as a flux

(molten salt) to help starting materials transferring easier than before. Consequently, the materials were molten easily. In another word, the m.p. of SrO might be reduced in this method. Combined with extended heating time to 60 h, a homogeneous distribution of Sr will be possible.

Sr-doped $NaTaO_3$ photocatalysts with Sr/Ta ratio fixed at 2 mol% were synthesized via MSM upon 1423 K for 1-60 hours. The combination of fluctuating heating time from 1 hour to 60 hours, radial distribution of Sr was successfully controlled. For 1 hour heating, Sr distributed inhomogeneously through the $NaTaO_3$ particles and population of photoexcited electrons were produced 159 times as that of undoped $NaTaO_3$. For 60 hours, on the other hand, Sr distributed homogeneously in the particles. As a result, electron population was only 9 times as that of $NaTaO_3$. Inhomogeneous distribution of Sr, indeed, restricted electron-hole recombination. Excited electrons transferred to bulk from holes left on the surface. These excited electrons required extra energy to move to the surface for reducing H_2O into H_2. Accordingly, the water spitting activity did not increase as well as efficiently restricted electron-hole recombination. A design of an appropriate Sr distribution is required to separate electrons from holes that eventually contribute to efficient water splitting.

5.2 EXPERIMENTAL SECTION

5.2.1 Synthesis and HF etching

Sr-doped $NaTaO_3$ photocatalysts were synthesized via the molten salt method (MSM), referring to an earlier study.[1] Na_2CO_3 (99.8%, Kanto), Ta_2O_5 (99.99%, Rare Metallic) and $SrCO_3$ (99.9%, Kanto) were mixed with NaCl (99.5%, Wako), which works as flux. Sr/Ta ratio in the mixture was adjusted to be 2 mol% with the Na_2CO_3/Ta_2O_5 molar ratio being 1.05. Weight concentration of NaCl flux was fixed at 50 wt% relative to the whole mixture. The mixture was separately put in four alumina crucibles and heated at 1423 K for 1, 10, 20 or 60 h to produce Sr-doped $NaTaO_3$ with different heating times. Another mixture without $SrCO_3$ was heated at 1423 K for 10 h to produce pristine $NaTaO_3$. The heated mixture was washed with purified water to remove excess NaCl to acquire final product: $NaTaO_3$ doped with Sr at 2 mol%. Hereafter, Sr-doped $NaTaO_3$ prepared via MSM upon heating for x h will be referred to as xh-Sr-NTO. For example, 1 h heated Sr-NTO is shown as 1h-Sr-NTO.

Sr-NTOs thereby prepared were chemically etched when necessary. Each Sr-NTO (0.25 g) was stirred in Teflon jar containing an aqueous HF solution (10 wt%, 3 ml, Wako) for 10 mins at room temperature and then washed with purified water until to get a neutral fluid.

5.2.2 Characterization

The composition of Sr-NTOs was quantified by an energy-dispersive X-ray fluorescence spectrometer (Shimadzu, EDX-720). The crystallographic phase and lattice volume were determined by an X-ray diffractometer (Rigaku, SmartLab). Raman scattering was observed in the air with a spectrometer (Jasco, NRS-7100) using laser light with an excitation wavelength of 532 nm. The size and shape of photocatalyst particles were imaged by a scanning electron microscope (Hitachi High-Technologies, S-4800). Measurement of TEM-EDX was operated by Dr. Mitsunori Kitta (AIST). Infrared (IR) light absorption induced by ultraviolet (UV) light irradiation was observed to evaluate the steady-state population of photoexcited electrons that had not recombined in Sr-NTOs. Each photocatalyst was suspended in water to a weight concentration of 3 g l^{-1}. 0.5 ml of the suspension was transferred to a CaF_2 plate and dried at 293 K for 20 hours in air. The transmission IR absorption spectrum of the dried plate was obtained under a vacuum of 10 Pa with a Fourier-

transform spectrometer (Jasco, FT/IR610) in the presence and in the absence of UV light irradiation. A 200-W Hg-Xe lamp (San-ei Electric, UVS-204S) was used as the UV light source. Light power at wavelengths of less than 370 nm was 60 mW cm^{-2} in the full spectrum of radiation. Measurement of H_2 and O_2 evolution from water splitting was conducted by Professor Dr. Akihide Iwase (Tokyo University of Science).

5.3 RESULTS AND DISCUSSION

5.3.1 Radial distribution of dopant

Four Sr-NTOs were synthesized via MSM with heating time at 1 h, 10 h, 20 h, and 60 h, respectively, in addition to undoped NTO heated for 10 h. Input Sr/Ta molar ratio was adjusted to 2 mol% in each Sr-NTO.

The composition of the four Sr-NTOs was examined by energy-dispersive X-ray spectroscopy (EDX). EDX results are summarized in **Fig. 5.1**. **Panel (A)** shows Sr-Kα emission spectra of Sr-NTOs. The intensity of each Sr-Kα emission was normalized to that of Ta-Lα emission to evaluate Sr/Ta molar ratio. The calculated ratio was in a range of 2.0±0.1 mol%, indicating Sr concentration insensitive to heating time. All the input Sr amount was believed left in the products.

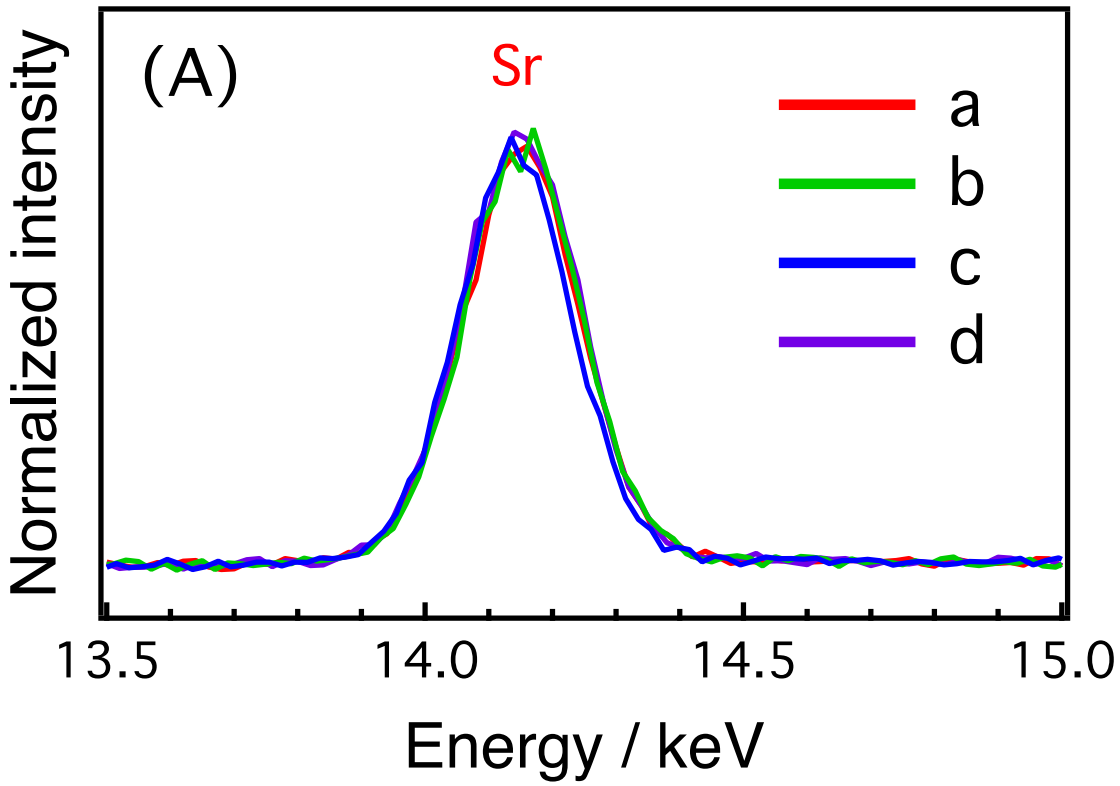

Figure 5.1 X-ray fluorescence spectra of Sr-NTOs. Panel (A) shows Sr-Kα spectra of a: 1h-Sr-NTO, b: 10h-Sr-NTO, c: 20h-Sr-NTO, and d: 60h-Sr-NTO.

During synthesis of Sr-NTOs through MSM, NaCl was used as flux reagent. To exclude the possibility of Cl contamination, Cl-Kα emission was examined. As shown in **Panel (B)** , the Sr-NTOs (spectrum a and d) presented weak peaks at 2.70, 2.83, and 2.95 keV. The NaCl (spectrum e) used as a reference showed a major peak at 2.62 keV, which is referred to Cl-Kα emission. The similar energy of Cl-Kα emission can also be found in the earlier study.[2] The different positions of the triple-peaked spectra of Sr-NTOs from that of NaCl depict absence of Cl contamination in Sr-NTOs prepared via MSM with NaCl.

Also, undoped NTO (spectrum f) prepared via solid-state method (SSM), where Na_2CO_3 and Ta_2O_5 were heated at 1173 K for 1 h followed by 1423 K for 10 h without the flux, showed the same triple peaks as shown in the Sr-NTOs (MSM). The result supports the triplet-peaks spectra are not attributed to Cl-Kα but may be from sample holder films or devices of EDX machine.

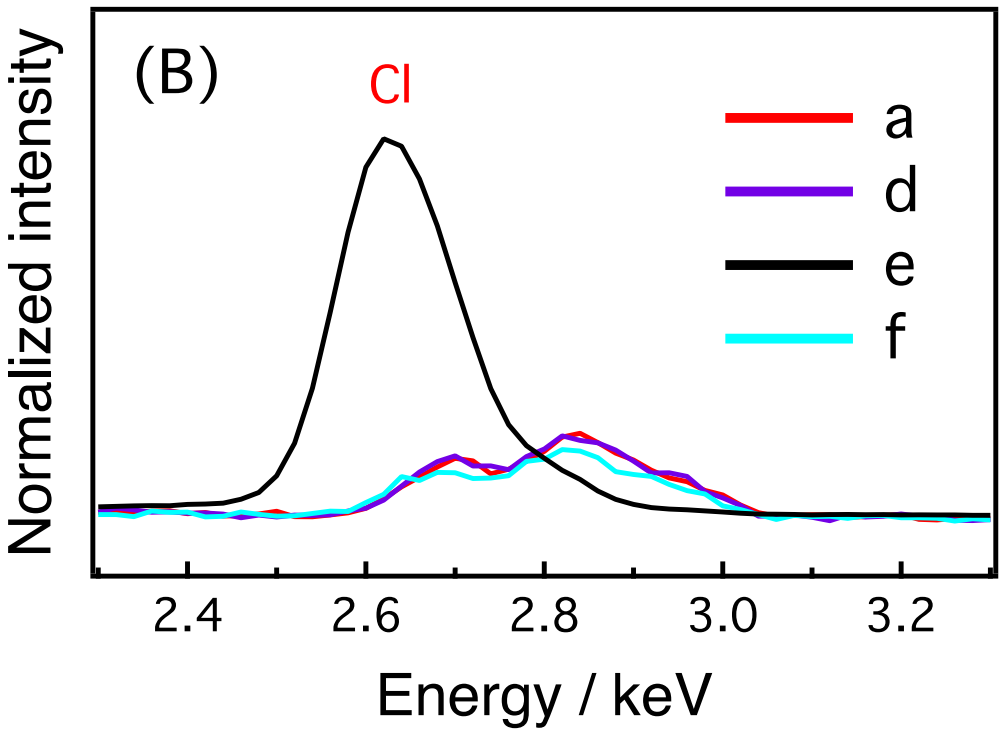

Figure 5.1. Panel (B) presents spectra appearing in the energy range of 2.3-3.3 keV. e: NaCl. Signal intensity was normalized to that of Ta-Lα emission in each object, and f: $NaTaO_3$ synthesized via the solid-state method.

Crystallographic lattices of Sr-NTOs were then detected by XRD. **Figure 5.2** shows X-ray diffraction patterns of NTO and Sr-NTOs. XRD patterns in a range of 10-80° are shown in **Panel (A)**. The peak positions of the five photocatalysts were similar and consistent with the diffraction patterns of perovskite-structured $NaTaO_3$ observed in the earlier study.[3] It clarifies Sr-NTOs are composed of a single phase of the perovskite structure. The absence of impurity phases proves the all input Sr amount, detected by EDX, took part in the doping reaction.

As described in chapter 3 of this thesis, substitution of Ta^{5+} cations (0.06 nm) with Sr^{2+} cations (0.12 nm) will lead XRD peak shifting to lower 2θ angle combined with peak broadening. Thus the width and position of the XRD peak provide a valuable information for a deeper understanding of the structure of Sr-NTOs. **Panel (B)** shows the XRD (110) peaks, referring to NTO with perovskite structure, of Sr-NTOs in addition to NTO. 1h-Sr-NTO produced a broadened peak relative to that of NTO, which appeared at 32.45°. Extended heating time from 1-60 h induced the broadened peak gradually shifted to lower 2θ angle. Eventually, in 60h-Sr-NTO, a relatively sharp peak was observed at 32.40°.

Comparison of the (110) peak width is shown in **Panel (C)**. In four Sr-NTOs, 60h-Sr-NTO produced the sharpest peak while 1h-Sr-NTO presented the broadest one. Based on the peak shifting and broadening, the author assumes part of Sr substituted Ta at B-sites in Sr-NTOs (MSM) as well as in Sr-NTOs (SSM) to form $NaTaO_3$-$Sr(Sr_{1/3}Ta_{2/3})O_3$ solid solutions.

One more important issue to consider here is the attribution to peak shifting and broadening. With the same Sr concentration at 2 mol%, four Sr-NTOs presented different response to change in XRD peaks, shifting or broadening. The author took into account the *distribution of Sr* to explain the difference, that is, Sr distribution is inhomogeneous in 1h-Sr-NTO and relatively homogeneous in 60h-Sr-NTO. Sr doped at B-sites induced peak shifting to lower angle due to lattice expansion. In 1h-Sr-NTO, inhomogeneous distribution of Sr should produce peak shift at different degrees on surface and in bulk. Consequently, the peak width expanded. In 60h-Sr-NTO, homogeneous distribution of Sr will produce a unit degree of peak shifting in any position of particles to eventually form a sharp XRD (110) peak. Sr distribution was more or less controlled by heating time of MSM. Extended heating time induced a homogeneous distribution of Sr, as expected.

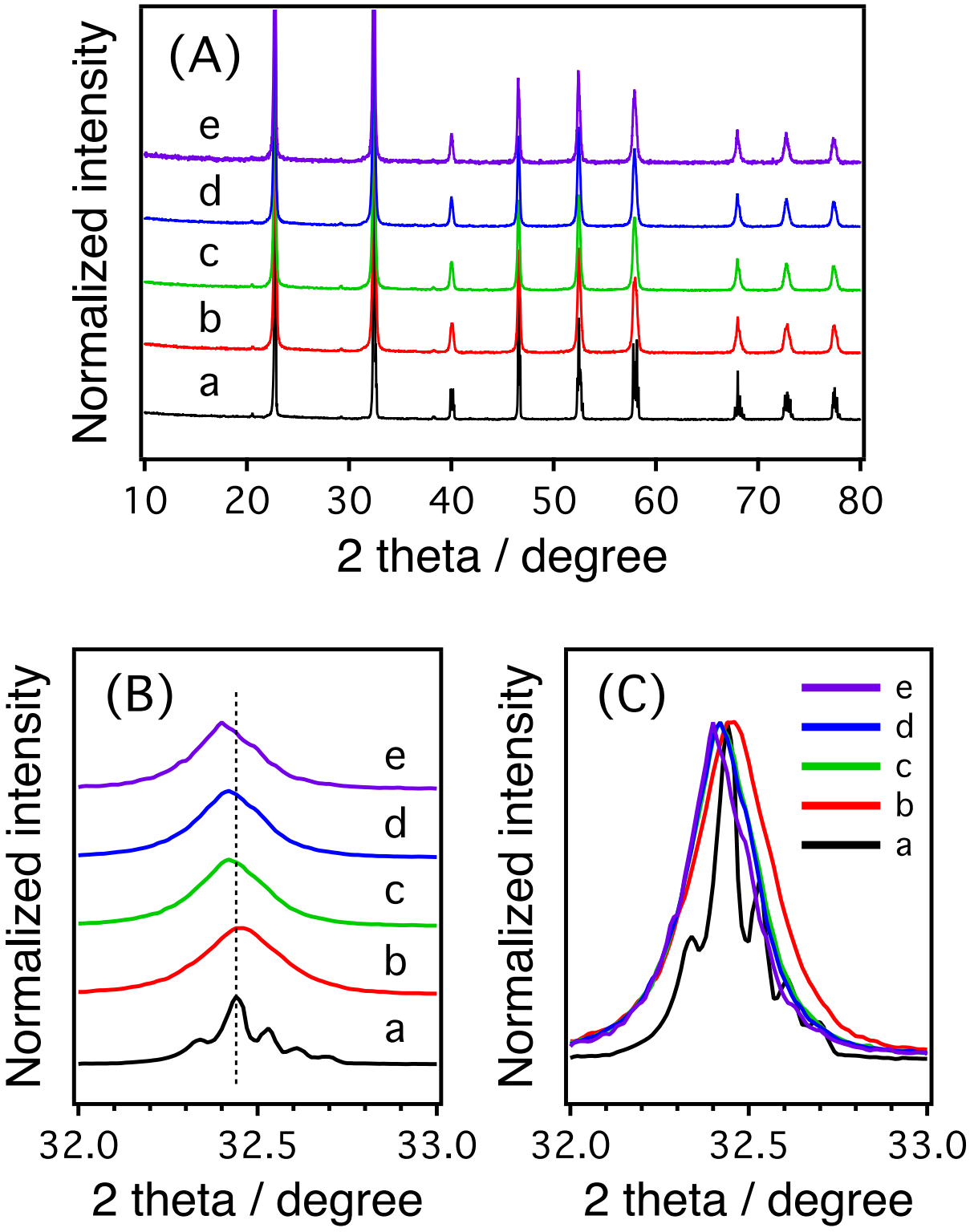

Figure 5.2 X-ray diffraction patterns of a: NTO, b: 1h-Sr-NTO, c: 10h-Sr-NTO, d: 20h-Sr-NTO, and e: 60h-Sr-NTO. (A) X-ray diffraction in a range of 10-80°. (B) Peak shift of the (110) peak. (C) Peak width of the (110) peak.

In XRD results, B-site doping of Sr was proposed to interpret the low-angle shifts and broadening of diffraction peaks. B-site doping was further examined and confirmed by Raman spectroscopy. **Figure 5.3** shows Raman spectra of the photocatalysts. Both in NTO (spectrum e) and Sr-NTOs (spectra a-d), three major bands attributing to Raman-active lattice vibration of $NaTaO_3$ appeared at 450, 500, and 620 cm^{-1}, respectively.[4] Besides, the four Sr-NTOs produced the extra band at 860 cm^{-1}. In chapter 3 of this thesis, assignment of the 860-cm^{-1} band was introduced and referred to the breathing vibration of TaO_6 octahedra in $NaTaO_3$-$Sr(Sr_{1/3}Ta_{2/3})O_3$ solid solution. Similar Raman band can also be seen in another $A(B_{1-x}B'_x)O_3$.[5,6] The presence of the 860-cm^{-1} band, hence, supports B-site doping of Sr as assumed in XRD measurement.

As shown in inset figure, the 860 cm^{-1} band intensity was reduced gradually with increased heating time at 1-60 h. It suggests the amount of Sr^{2+} doped at B sites was reduced because the 860 cm^{-1} band intensity was nearly proportional to Sr concentration. In chapter 3, the plot of the 860 cm^{-1} band intensity in Sr-NTOs (SSM) as a function of input Sr concentration presented nice linear relationship.

To explain XRD peak shifting and broadening, radial distribution uniformity of Sr was introduced. It also works on the results of Raman scattering. Due to the difference of ionic radius between Ta^{5+} and Sr^{2+} cations, B-site doping of Sr will lead to lattice expansion and distortion. Excessive local doping of Sr at B-sites will result in collapse of crystal lattices once the degree of lattice distortion exceeded crystal tolerance. To keep solid crystal lattices, the local amount of Sr doped at B-sites should be controlled. Effect of distribution uniformity of Sr on the amount of B-site doped Sr was discussed in comparison of 1h-Sr-NTO and 60h-Sr-NTO.

In 60h-Sr-NTO, with a homogeneous distribution of Sr, we can roughly consider the lattice expansion mainly occurred in bulk of particles. In bulk, lattice distortion should be controlled at the minimum degree to keep solid crystal lattices. The lattice expansion from B-sites doping is naturally not welcome and will be restricted. As a result, a limited amount of B-site doping is forgiven. Thus the intensity of 860-cm^{-1} band was relatively weak. On the other hand, in 1h-Sr-NTO, most Sr^{2+} cations were doped on the surface of Sr-NTO particles. Lattice

distortions grew on the surface play limited role in the crystal structure in bulk. Hence Sr doped at B-sites is allowed to a higher degree on 1h-Sr-NTO than on 60h-Sr-NTO.

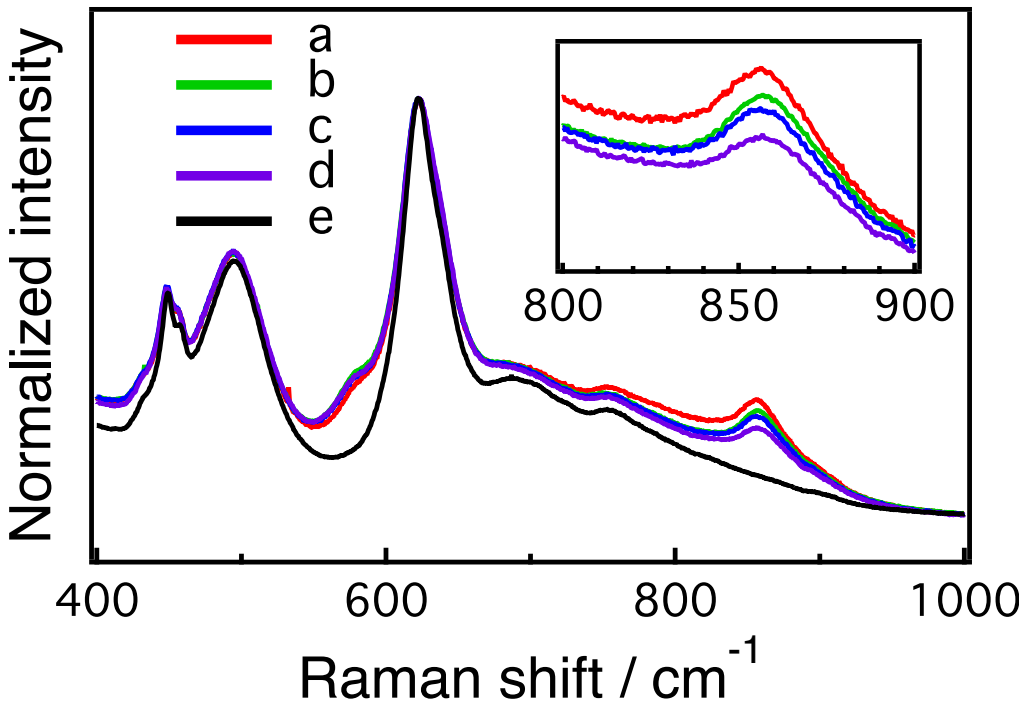

Figure 5.3. Raman spectra of a: 1h-Sr-NTO, b: 10h-Sr-NTO, c: 20h-Sr-NTO, d: 60h-Sr-NTO, and e: NTO. Intensity was normalized at 620 cm^{-1}.

A different number of Sr doped at B-sites in Sr-NTOs affected the particle shape. **Figure 5.4** shows scanning electron micrographs of NTO and Sr-NTOs. Micrometer-sized cubic particles with round corners were produced in NTO (image a). The size of primary, cubic particles was reduced to about 50 nm by Sr doping. The size of particles was insensitive to heating time (images b-e), but the particle shape was. There are two characteristic features of Sr-NTOs particle shape to consider.

One feature is the relatively round corners observed on the surface of 1h-Sr-NTO particles compared to the other three Sr-NTOs particles. As summarized from XRD and Raman results, Sr segregated on the surface of 1h-Sr-NTO particles to form inhomogeneous distribution in the radial direction. Different surface morphology of 1h-Sr-NTO from the other three Sr-NTOs also supports the unique surface composition and structure.

The other characteristic feature is the smooth surface of the four Sr-NTOs. In chapter 3, Sr-NTO (SSM) produced regularly separated ten-nanometer-length steps on the particle surface. As a reference, 2%Sr-NTO (SSM) is presented as image f. In chapter 3, surface restructuring with regular steps was interpreted with the core-shell structure induced by Sr doping: a Sr-rich shell forms in a heteroepitaxial manner over a Sr-poor core. The regularly separated steps spontaneously appear, thereby correcting the lattice mismatch at the epitaxial interface. With this interpretation, the absence of regularly separated steps suggests the absence of the core-shell structure in the MSM-prepared Sr-NTOs. Although XRD results evidenced for Sr segregation to 1h-Sr-NTO particles, a clear phase boundary between core and shell was not absent. In 1h-Sr-NTO (MSM), surface morphology was restructured to be round for keeping Sr segregation on the surface. Not like in Sr-NTO (SSM) where step structures were produced, the lattice mismatch between $Sr(Sr_{1/3}Ta_{2/3})O_3$ and $NaTaO_3$ was smoothly solved in Sr-NTO (MSM). NaCl flux may make a significant contribution to the smooth release of lattice mismatch energy.

So far, Sr segregation was proposed being present in 1h-Sr-NTO and absent in 60h-Sr-NTO. It seems the primary purpose of this chapter, preparing Sr-NTOs with fixed Sr concentration in addition to different Sr distribution uniformity, was completed.

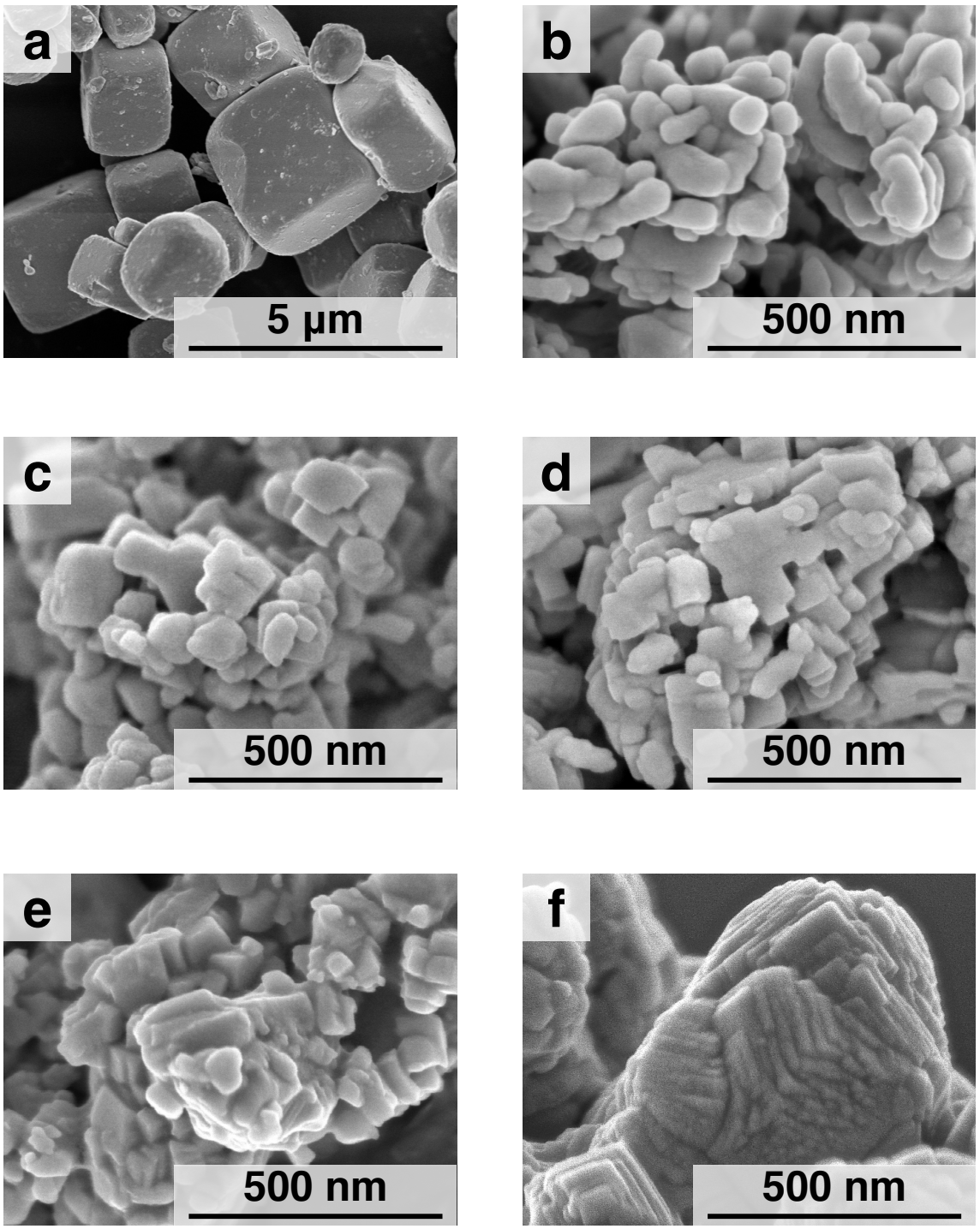

Figure 5.4. Scanning electron micrographs of a: NTO, b: 1h-Sr-NTO, c: 10h-Sr-NTO, d: 20h-Sr-NTO, and e: 60h-Sr-NTO. A micrograph of Sr-doped $NaTaO_3$ with 2 mol% Sr-Ta ratio prepared via the solid-state method is shown in f for comparison.

As a strong support to confirmation of Sr distribution uniformity, energy dispersive X-ray fluorescence spectroscopy (EDX) lined with scanning transmission electron microscopy (STEM) was applied to trace Sr concentration in radial distribution. The STEM-EDX was measured by Dr. Mitsunori Kitta (AIST). **Figure 5.5(A)** shows high-angle annular dark field (HAADF) TEM image of 60h-Sr-NTO. EDX mapping of Sr, Ta, Na, and O are respectively listed in **Fig. 5.5(B-E)**. In **Fig. 5.5(F)**, EDX spectra were detected at two different positions, separately shown as spectrum 1 (Sp 1) and spectrum 2 (Sp 2). Intensities of the spectra were normalized at Ta emissions. **Figure 5.5(G)** shows Sr-focused EDX spectra with Sr-Ka emission at about 14.2 keV. The Sr concentration near to surface (Sp 1) was almost the same as in bulk (Sp 2). Homogeneous distribution of Sr is thus the case in 60h-Sr-NTO, as was previously proposed according to XRD (110) peak shifting.

On the other hand, Sr segregation was observed on the surface of 1h-Sr-NTO, as expected. **Figure 5.6(A-E)** show TEM image and EDX mapping of 1h-Sr-NTO. Again, the EDX spectra were detected at two positions, one is near to surface (Sp 1) and the other is in bulk (Sp 2). **Figure 5.6(F)** shows normalized EDX spectra at two positions. As shown in **Fig. 5.6(G)**, the stronger Sr intensity was produced in surface rather than in bulk. It indicates Sr segregated on the surface in 1h-Sr-NTO.

To detect Sr segregation depth, elements (Sr, Ta, Na, O) concentration were scanned from surface to bulk. Scanning trace was marked by a line (X-Y), as shown in **Fig. 5.7(A)**. EDX spectra with normalized intensity are shown in **Fig. 5.7(B)**. Ta, Na and O presented homogeneous distribution from surface to bulk in about 15 nm depth. On the other hand, Sr segregated seriously on the surface with depth at about 3 nm.

In summary, Sr segregated on the surface in 1h-Sr-NTO. Inhomogeneous distribution of Sr at B-sites induced XRD peak broadening. Surface segregation allowed excessive Sr doped at B-sites and further produced spherical particle morphology. In contrast, 60h-Sr-NTO produced sharp XRD peaks due to the homogeneous distribution of Sr. Moderate degree of B-sites doping of Sr reduced 860 cm^{-1} Raman band.

As planned ahead, a different pattern of Sr distribution alongside fixed Sr concentration was successfully designed through MSM by controlling heating time. Effect of radial distribution of Sr on electron-hole recombination rate was studied IR absorbance spectroscopy upon UV irradiation for quantifying photoexcited electrons.

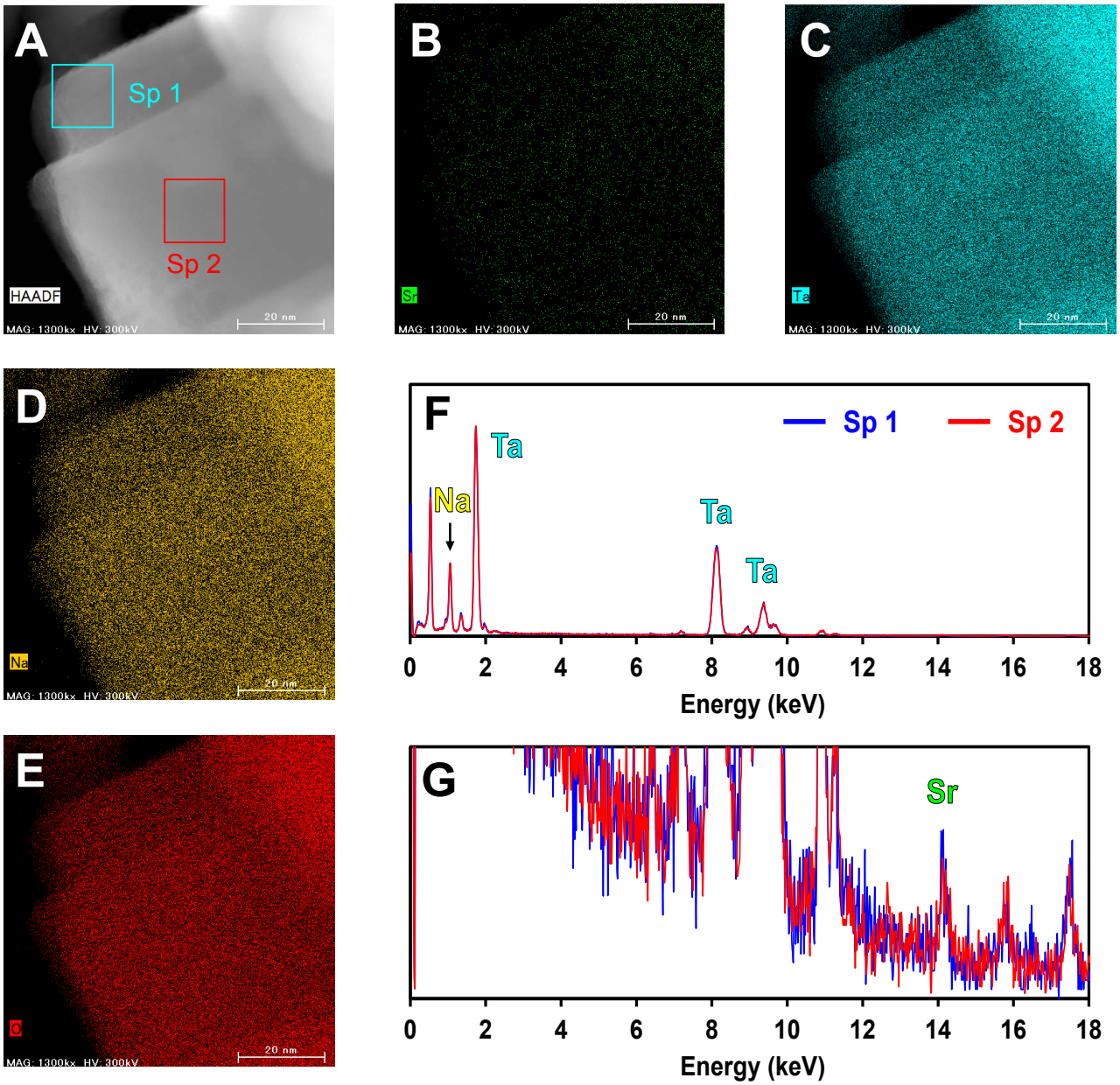

Figure 5.5. (A) High-angle annular dark field (HAADF) scanning transmission electron micrograph of 60h-Sr-NTO. EDX mapping of (B) Sr, (C) Ta, (D) Na, and (E) O. EDX spectra are shown as (F) all and (G) focused on Sr.

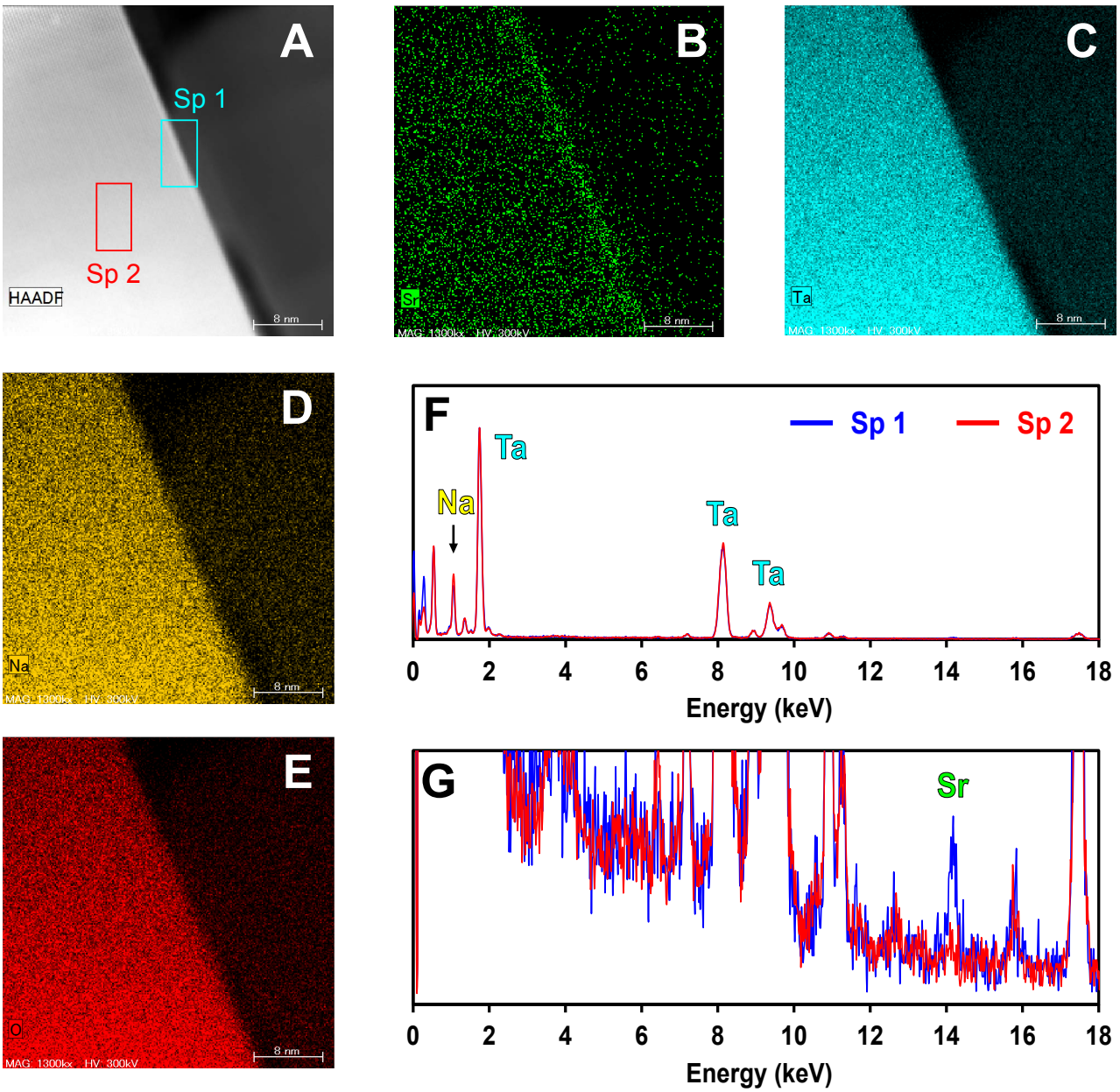

Figure 5.6. (A) High-angle annular dark field (HAADF) scanning transmission electron micrograph of 1h-Sr-NTO. EDX mapping of (B) Sr, (C) Ta, (D) Na, and (E) O. EDX spectra are shown as (F) all and (G) focused on Sr.

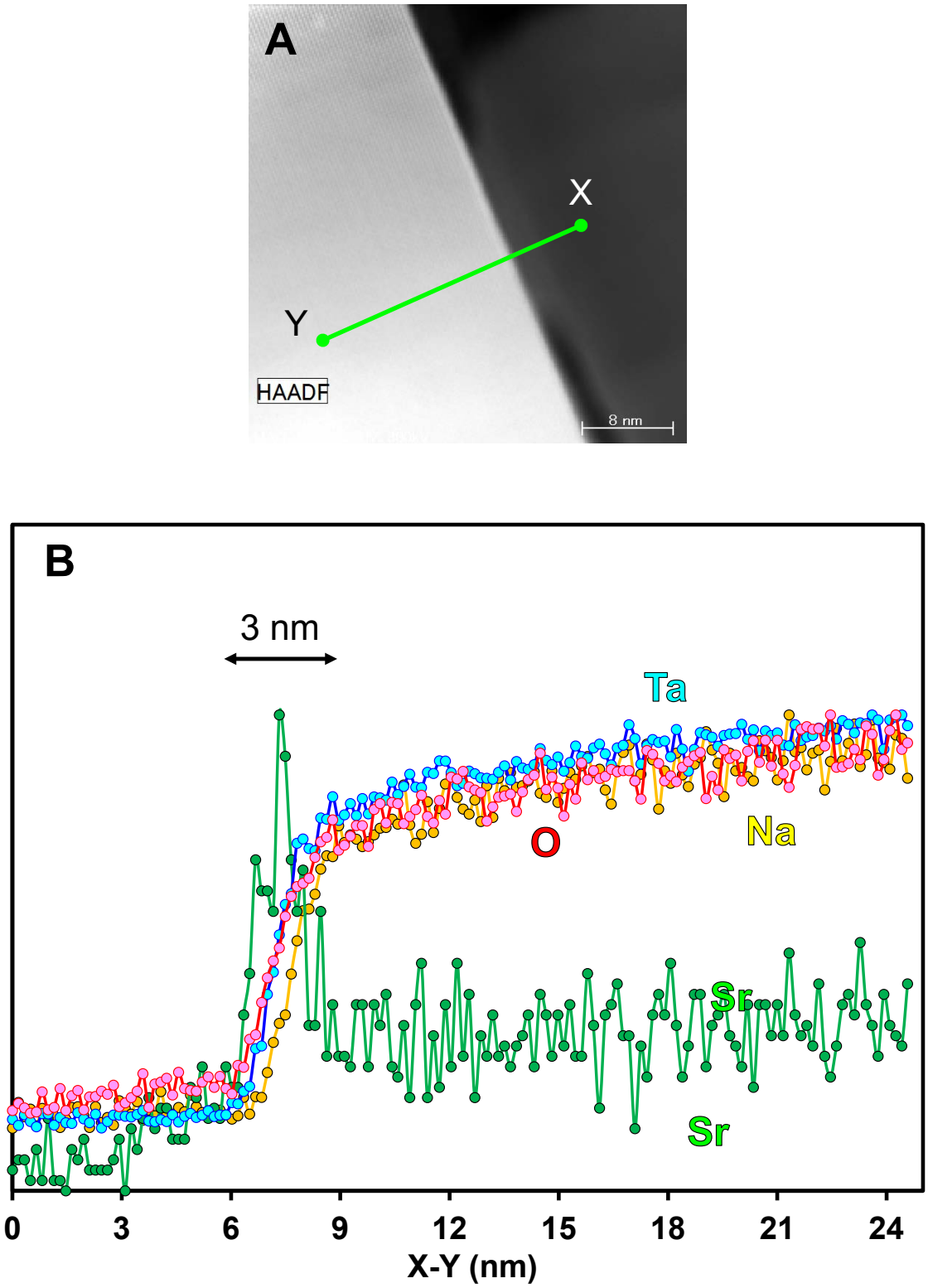

Figure 5.7. (A) High-angle annular dark field (HAADF) scanning transmission electron micrograph of 1h-Sr-NTO. (B) Normalized EDX intensity of Sr, Ta, Na, and O scanned through X-Y line as marked in (A).

Figure 5.8(A) shows the change in the IR absorbance spectra before and after UV irradiation of the NTO and Sr-NTOs. UV-induced absorbance change is always positive and increased monotonically with decreasing wavenumber from 6000 to 900 cm^{-1}.[7-9] This monotonic IR absorption was assigned to electronic excitation of band-gap excited electrons not yet recombined to holes, as described in chapter 3.

IR absorbance change was integrated into the range of 6000 to 900 cm^{-1} for calculating the population of photoexcited electrons. **Figure 5.8(B)** shows the integrated absorbance change of each Sr-NTO normalized to that of NTO. 1h-Sr-NTO presented the strongest absorbance change that was enhanced by 159 times relative to the absorbance change of NTO. Longer heating times reduced absorbance change down to 75 times on 10h-Sr-NTO, 43 times on 20h-Sr-NTO, and eventually 9 times on 60h-Sr-NTO.

It was unexpected that UV-induced absorbance change as so sensitive to extended heating in the flux with a fixed doping concentration. The absorbance change in 1h-Sr-NTO was larger by 18 times than that of 60h-Sr-NTO. The large absorbance change indicates an increased population of excited electrons. The rate of electron-hole recombination should have been restricted in 1h-Sr-NTO accordingly.

Extended heating time from 1 h to 60 h gradually induced a homogeneous distribution of Sr. To confirm the effect of Sr distribution on the electron-hole recombination, 1h-Sr-NTO was calcined for additional 59 h in the presence of NaCl flux to produce 1h+59h-Sr-NTO. Upon additional heating for 59 h, 1h+59h-Sr-NTO should have a similar structure as 60h-Sr-NTO. As expected, 1h+59h-Sr-NTO showed apparently reduced IR absorbance change from 1h-Sr-NTO. The calculated absorbance change was only 11 times relative to that of NTO, showing almost the same value as 60h-Sr-NTO. It is thus concluded the inhomogeneous distribution of Sr plays a key role to restricting electron-hole recombination.

Upon UV irradiation, IR absorbance change in a particular material is also decided by band gap energy. **Figure 5.9** shows UV absorption spectra of NTO and typical Sr-NTOs. The same absorption spectra in each photocatalyst indicate the same rate of excitation with the fixed number of incident UV photons.

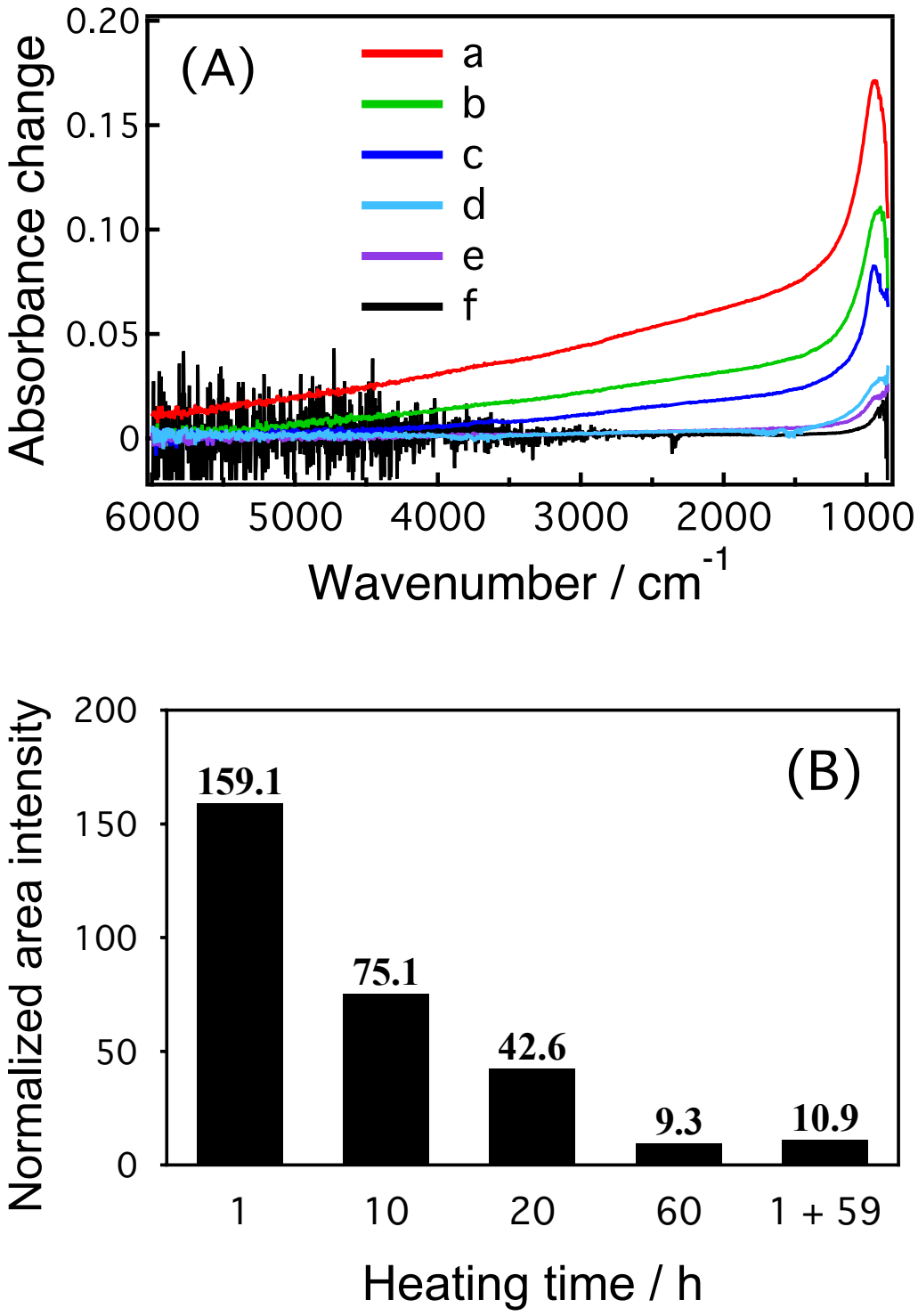

Figure 5.8. IR absorption change induced by UV light irradiation. (A) Absorbance-change spectra of a: 1h-Sr-NTO, b: 10h-Sr-NTO, c: 20h-Sr-NTO, d: 1h+59h-Sr-NTO, e: 60h-Sr-NTO, and f: NTO. (B) Integrated absorbance change of Sr-NTOs relative to that of NTO as a function of heating time.

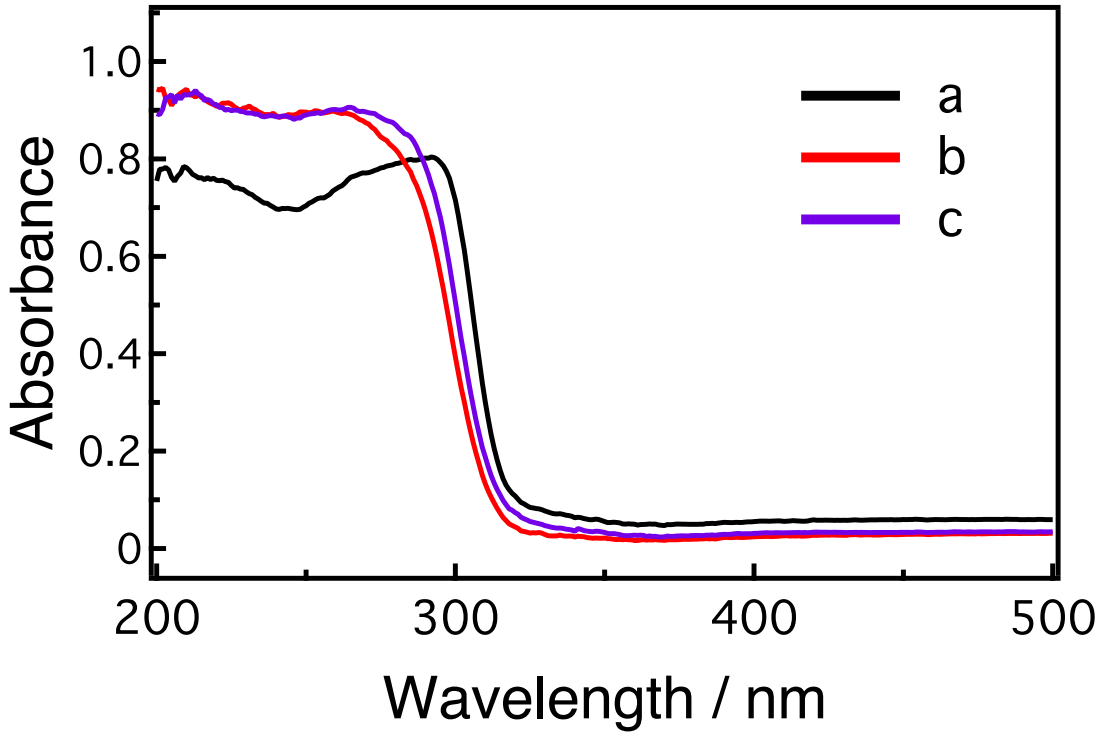

Figure 5.8. UV-Vis absorption spectra of a: NTO, b: 1h-Sr-NTO, c: 60h-Sr-NTO.

5.3.2 Response to HF etching

To confirm the effect of Sr distribution on electron-hole recombination, HF etching was applied. As depicted in chapter 4, $NaTaO_3$ particles were successfully etched with HF solution. In this subsection, two photocatalysts, 1h-Sr-NTO and 60h-Sr-NTO, were chemically etched in the HF solution for 10 min at room temperature. In 1h-Sr-NTO, the concentration gradient is expected to decrease by removing Sr-rich surface layers that consequently reduces photoexcited electron population.

Etched 1h-Sr-NTO was characterized as summarized in **Fig. 5.10**. Etched photocatalyst particles appeared clustered spherical cubes with a smooth surface as seen in the scanning electron micrograph of **Panel (A)**. The size of primary particles was 50-100 nm being unchanged from unetched particles (**Fig. 5.4-b**). These features indicate that surface layer thinner than 10 nm was removed during etching for 10 min. At the same time, Sr-Kα emission intensity decreased by 6% and the 860-cm^{-1} band in Raman scattering also weakened, as shown in **Panel (B)** and **(C)**. Fluorescence x-ray and Raman scattering are bulk-sensitive probes to quantify the particle-averaged concentration of total Sr and Sr placed at B sites, respectively. It is natural that the two concentrations decreased by removing the Sr-rich surface layer. The steady-state population of electrons excited by lamp irradiation reduced as expected. **Panel (D)** presents irradiation-induced IR absorbance change before and after etching. The shape of absorbance change spectrum remained intact, and the integrated absorbance change decreased from 159 (unetched) to 65 (etched). Excited electron population reduced accordingly when we assume constant absorbance per electron in 1h-Sr-NTO etched and unetched.

60h-Sr-NTO with homogeneous Sr distribution was etched and characterized for reference. Scanning electron micrograph, X-ray fluorescence spectrum, and Raman scattering results were almost unchanged during etching, as shown in **Fig. 5.11(A-C)**. It is because Sr was distributed homogeneously in photocatalyst particles. In **Fig. 5.11(D)**, the steady-state population of photoexcited electrons, which was quantified by integrated IR absorbance change, increased from 9 (unetched) to 17 (etched). Compared to the absolute reduction from 159 to 65 on etched 1h-Sr-NTO, the absolute increase from 9 to 17 on etched 60h-Sr-NTO was ignorable.

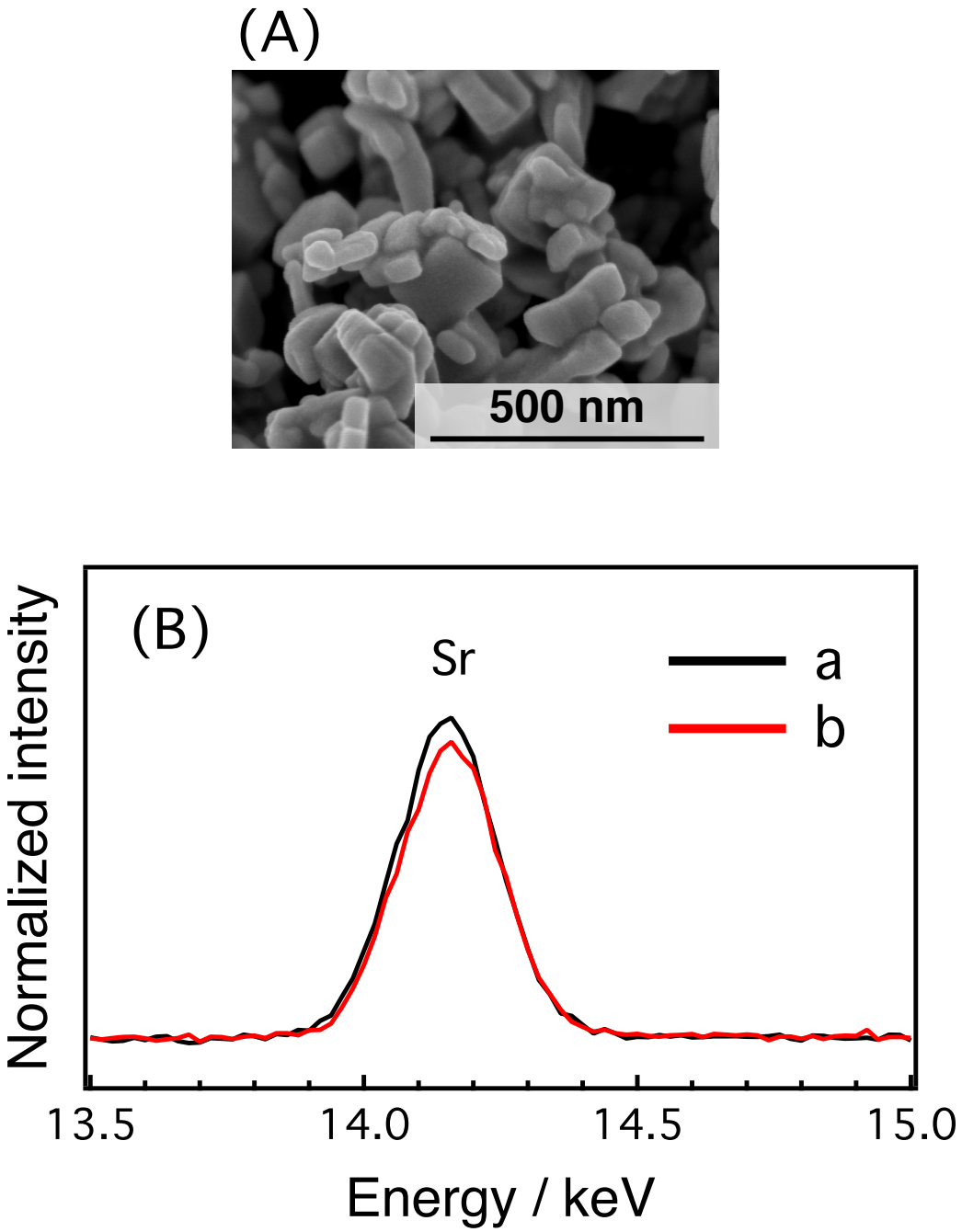

Figure 5.10. 1h-Sr-NTO etched with the HF solution. (A) Scanning electron micrograph. (B) X-ray fluorescence spectra of a: unetched and b: etched photocatalyst. Intensity was normalized to that of Ta-Lα emission.

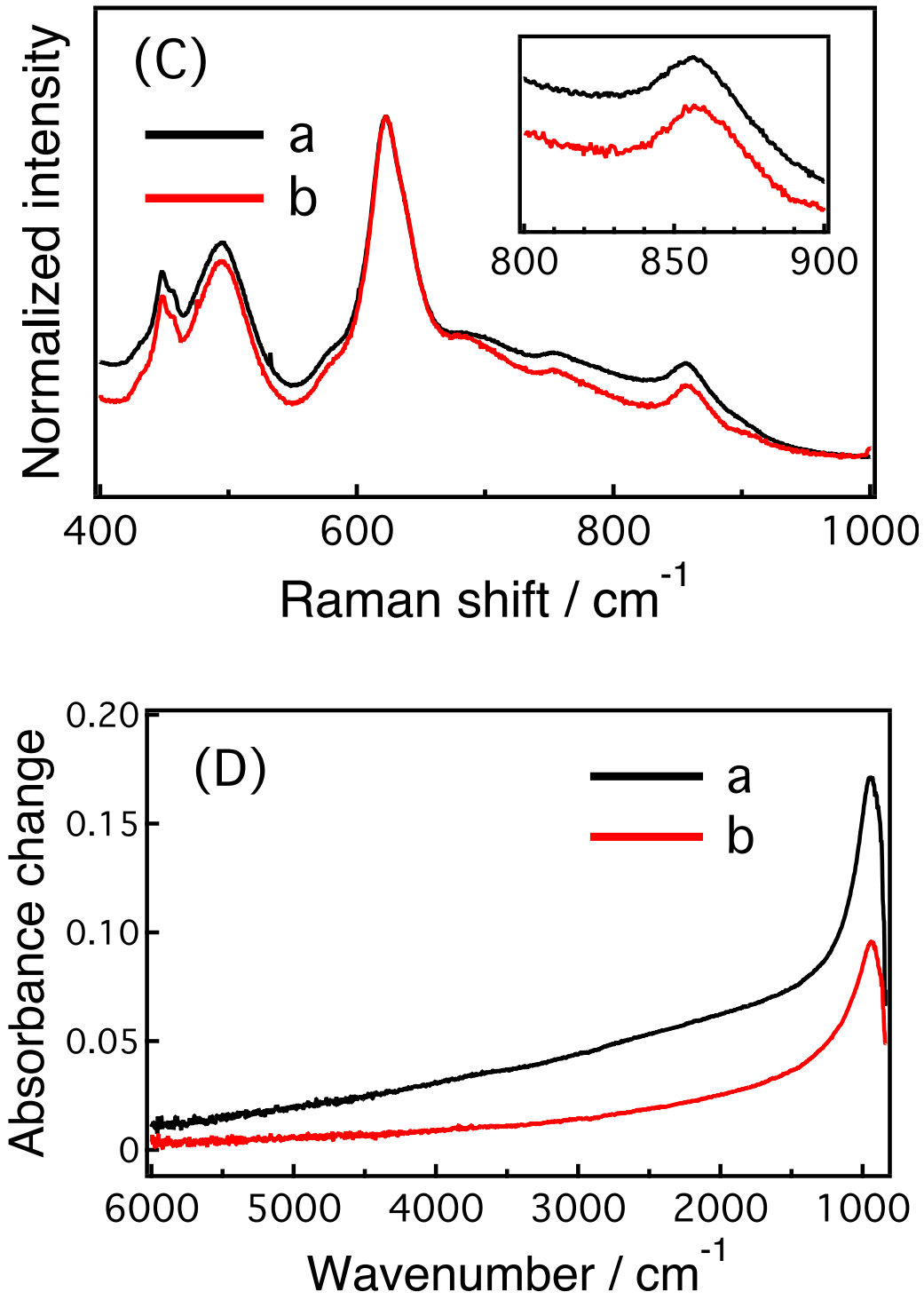

Figure 5.10. 1h-Sr-NTO etched with the HF solution. (C) Raman spectra of a: unetched and b: etched photocatalyst. Intensity was normalized at 620 cm^{-1}. (D) IR absorbance change induced by UV-light irradiation on a: unetched and b: etched photocatalyst.

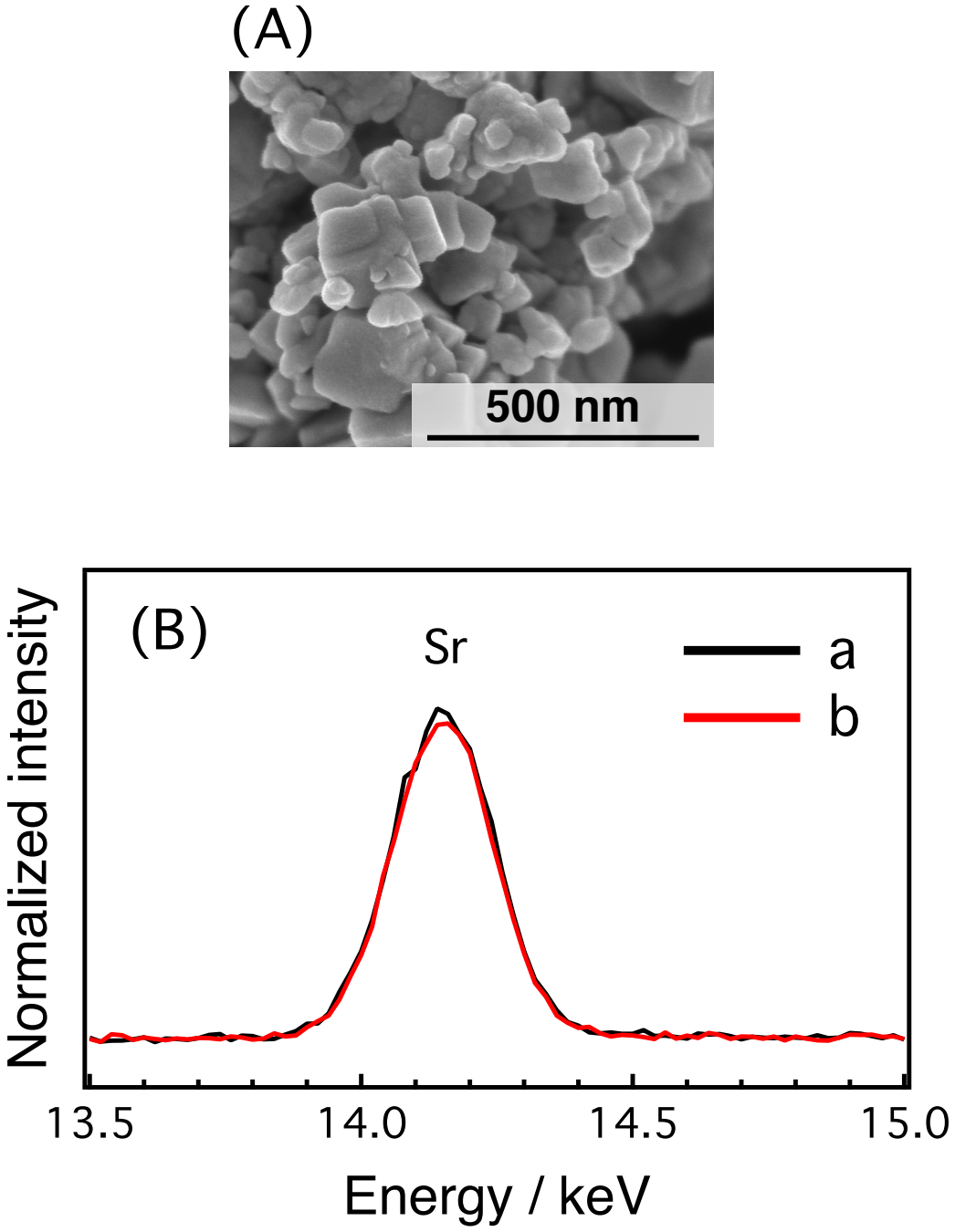

Figure 5.11. 60h-Sr-NTO etched with the HF solution. (A) Scanning electron micrograph. (B) X-ray fluorescence spectra of a: unetched and b: etched photocatalyst. Intensity was normalized to that of Ta-Lα emission.

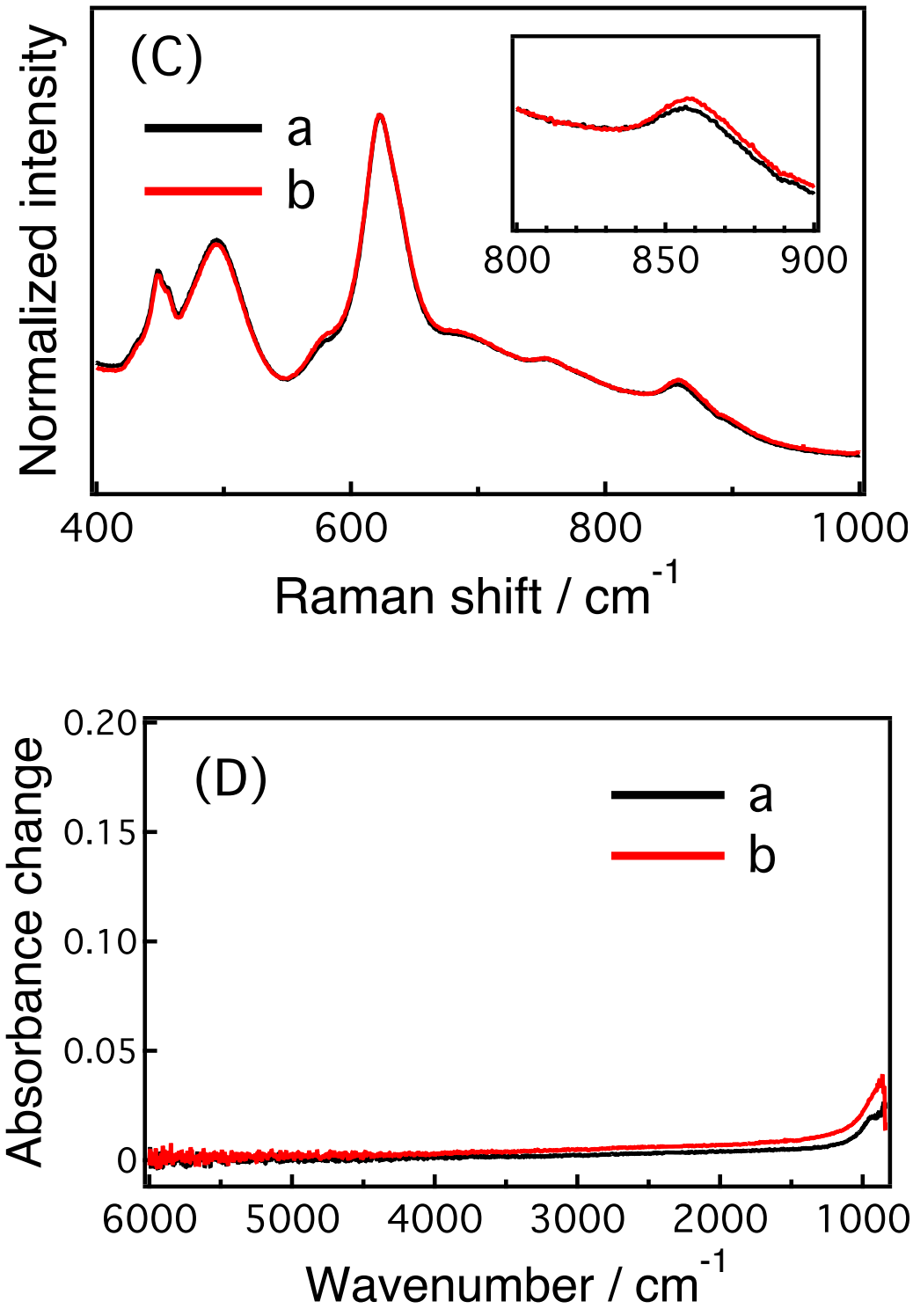

Figure 5.11. 60h-Sr-NTO etched with the HF solution. (C) Raman spectra of a: unetched and b: etched photocatalyst. Intensity was normalized at 620 cm^{-1}. (D) IR absorbance change induced by UV-light irradiation on a: unetched and b: etched photocatalyst.

The above results indicate that recombination of excited electrons and holes was restricted actually by Sr concentration gradient present in 1h-Sr-NTO particles. A possible mechanism behind restricted recombination is considered here.

In chapter 3, it was revealed that $NaTaO_3$-$SrSr_{1/3}Ta_{2/3}O_3$ solid solution was produced in Sr-doped $NaTaO_3$ prepared via the solid-state reaction. In the solid-solution, A site cations and B site cations of the perovskite-structured oxide were simultaneously doped with Sr. The study in the present chapter showed that Sr-NTOs prepared in the NaCl flux also produced $NaTaO_3$-$SrSr_{1/3}Ta_{2/3}O_3$ solid solution. Electron-hole recombination was remarkably restricted in the solid-solution photocatalysts, no matter solid-state-prepared or flux-prepared. The steady-state population of photoexcited electrons was enhanced by 180 times in a solid-state-prepared photocatalyst (Sr concentration: 2.0 mol%) and by 159 times in flux-prepared 1h-Sr-NTO (Sr concentration: 2.0 mol%). On the other hand, Sr doping via the hydrothermal reaction produced a structural isomer with A sites selectively doped. The A-site doped photocatalysts presented no enhancement of electron population (chapter 3). Hence, doping B-site cations is essential to restricting recombination in $NaTaO_3$ photocatalysts.

Meanwhile, in addition to results from chapter 4, the present study demonstrated that Sr concentration gradient controlled recombination rate in Sr-NTO particles. By combining the two findings, we now conclude that concentration gradient of Sr doped at B-sites (CGSrB) is the key for restricted recombination.

The conduction band of $NaTaO_3$ is composed of unoccupied Ta 5d orbitals.[10-12] In the $NaTaO_3$-$SrSr_{1/3}Ta_{2/3}O_3$ solid solution, Sr doped at B-sites mean defect of Ta. Hence the B-site doping with Sr should induce conduction band minimum shifted upward. Consequently, the band gap energy should increase. The central wavelength of the light absorption edge of $NaTaO_3$ (SSM) was at 305 nm and shifted to 300 nm upon Sr doping at 0.5-20 mol%, as shown in chapter 3. A small but finite shift from 305 to 300 nm is consistent to the conduction band minimum shifted upward. With Sr segregation on the surface, bulk-sensitive UV-Vis absorption spectroscopy could not accurately detect possible absorption edge shift that occurred mainly on the surface of Sr-NTO particles. The shift of absorption edge was apparent when doped with Sr at even higher concentration, for example at 50 mol%. With

surface saturation with Sr, excessive Sr penetrated into bulk was detected by UV-Vis spectroscopy.

In this picture, the energy of conduction band minimum is sensitive to the local concentration of SrO_6 octahedra, and hence CGSrB makes a potential gradient of conduction band (CB) minimum in Sr-NTO particles. The Blue shift of UV-Vis absorbance by Sr doping means the CB minimum energy was more negative on the surface (Sr segregation) than in bulk. Photoexcited electrons are driven to bulk through the potential gradient, whereas leaving holes on the surface. Electron-hole recombination is restricted as a result. Such potential gradient formed in crystal were confirmed to drive efficient separation of electrons and holes, as studied on $SrTiO_3$,[13] $KTaO_3$,[14] and TiO_2.[15]

5.3.3 Water splitting activity

No matter how efficiently the electron-hole recombination is restricted, a photocatalyst is useless in the application if without high photocatalytic activity. In this subsection, water splitting activity was measured on NTO (MSM) and Sr-NTOs (MSM) by . Each photocatalyst (0.5 g) was dispersed in 350 ml water before light irradiation (450 W, Hg-lamp). Under stirring, the generation rate of H_2 and O_2 was measured. The measurement was conducted by Professor Dr. Akihide Iwase (Tokyo University of Science).

Figure 5.12 shows H_2 and O_2 generation rate from water splitting on NTO and Sr-NTOs. Measurement on each photocatalyst was performed twice, 8 h for one run, with a middle break. The gas generation rate is summarized in **Table 5.1**. Pristine NTO showed the lowest activity, as expected. The activity of Sr-NTO increased gradually with heating time in a range of 1-20 h but suddenly decreased on 60h-Sr-NTO. In IR absorbance change upon UV irradiation, the population of photoexcited electrons was reduced consistently with extended heating time. Water splitting activity showed different tendency with heating time to the excited-electron population in Sr-NTOs (MSM). This inconsistency can be explained by a concept of "effective electrons".

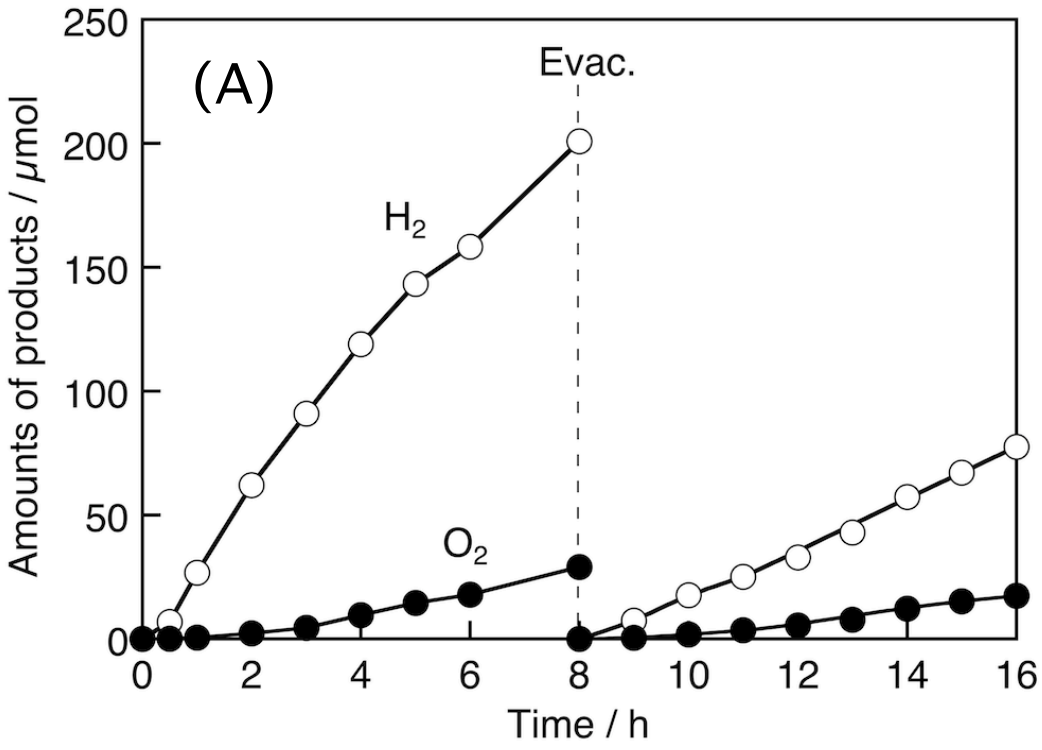

Figure 5.12. H_2 and O_2 generation rate from water splitting of (A) NTO.

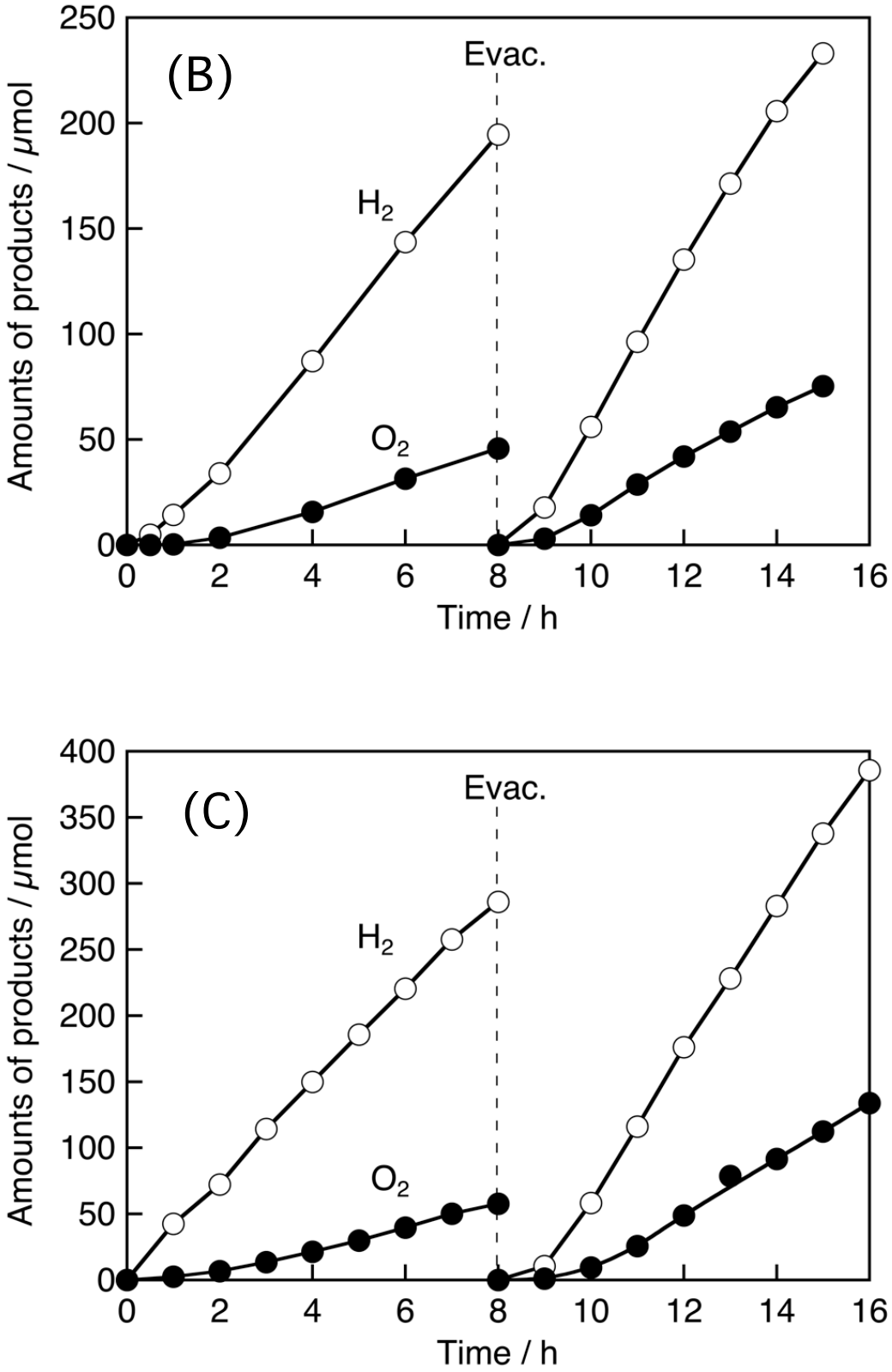

Figure 5.12. H_2 and O_2 generation rate from water splitting of (B) 1h-Sr-NTO, (C)10h-Sr-NTO.

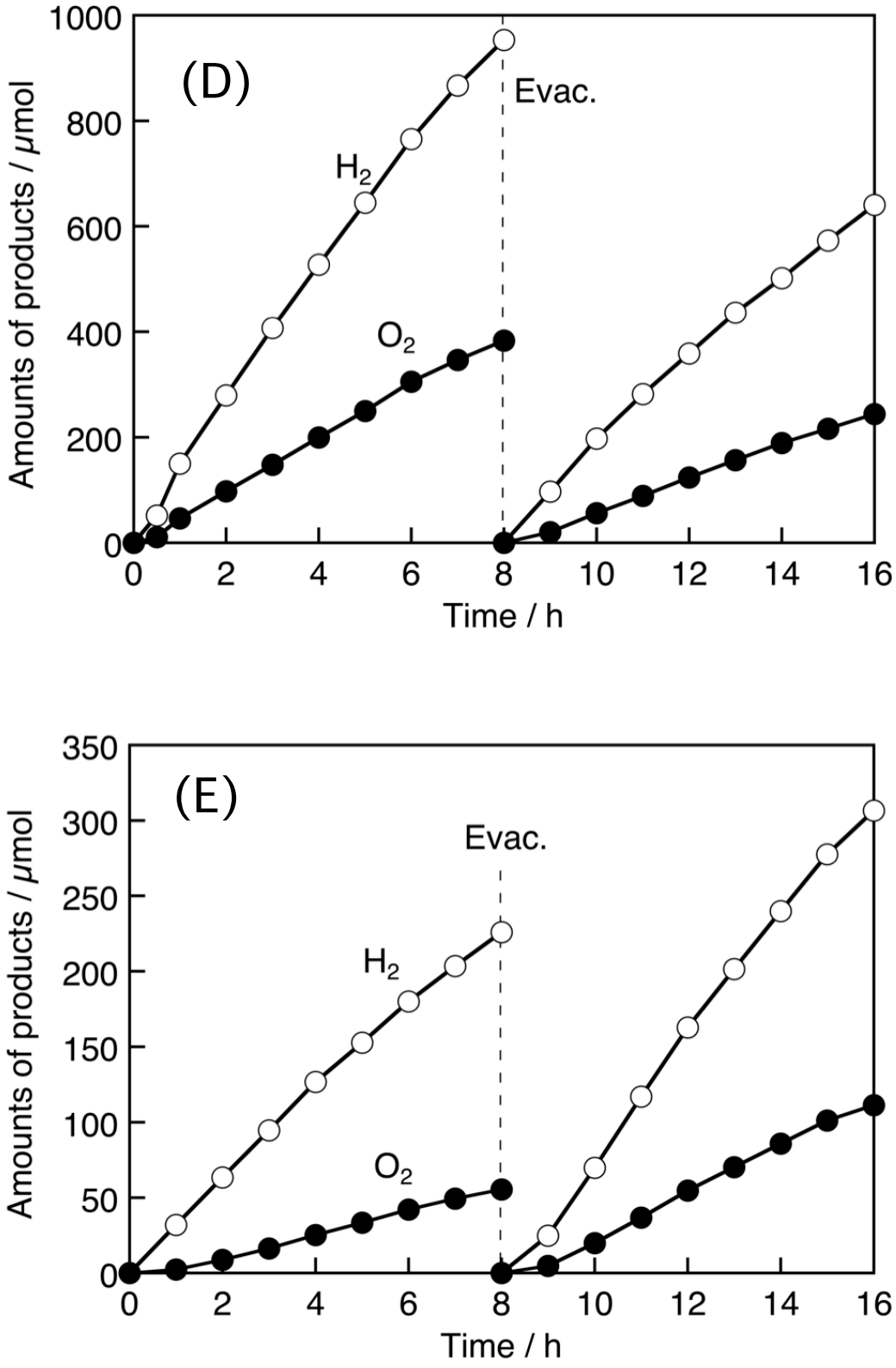

Figure 5.12. H_2 and O_2 generation rate from water splitting of (D) 20h-Sr-NTO, (E) 60h-Sr-NTO.

Sample	Activity / μmol h^{-1}		Period of time for activity calculation
	H_2	O_2	
A	11	2.8	2nd run, 11-16 h
B	39	13	2nd run, 9-12 h
C	55	22	2nd run, 11-15 h
D	123	52	1st, 1-6 h
E	44	16	2nd run, 9-13 h

Table 5.1. H_2 and O_2 generation rate calculated based on **Fig. 5.12**.

Water splitting mainly occurs on the surface of photocatalyst particles. Photoexcited electrons need to transfer to the surface for participating the reaction. Here we name, for a convenience, the electrons capable of reaching the surface as "effective electrons". The population of effective electrons will be decided by two factors; the total population of excited electrons and the ease of electron transferring to surface. **Figure 5.13** shows the effective/ineffective ratio of photoexcited electrons in each Sr-NTO, schemed according to the results of UV-induced IR absorption and water splitting activity.

In the case of 1h-Sr-NTO, CGSrB with strong degree drove charge separation to generate a large population of excited electrons. The potential gradient of CB kept most electrons in bulk. During light irradiation, the CGSrB worked as an energy barrier for preventing electrons from moving to surface, consequently, the population of effective electrons was remained few, despite having a large population of electrons. With extended heating time, the energy barrier was reduced with weakened degree of CGSrB. The ease of electrons transferring to surface increased accordingly. Therefore, the population of effective electrons increased gradually with heating time in a range of 1-20 h. However, in 60h-Sr-NTO, the population of effective electrons was reduced drastically due to the limited population of excited electrons. CGSrB with a very low degree not only produced low energy barrier but also reduced the population of excited electrons. Consequently, the activity decreased. How to adjust a fair degree of CGSrB is thus a key factor to realize water splitting with high efficiency.

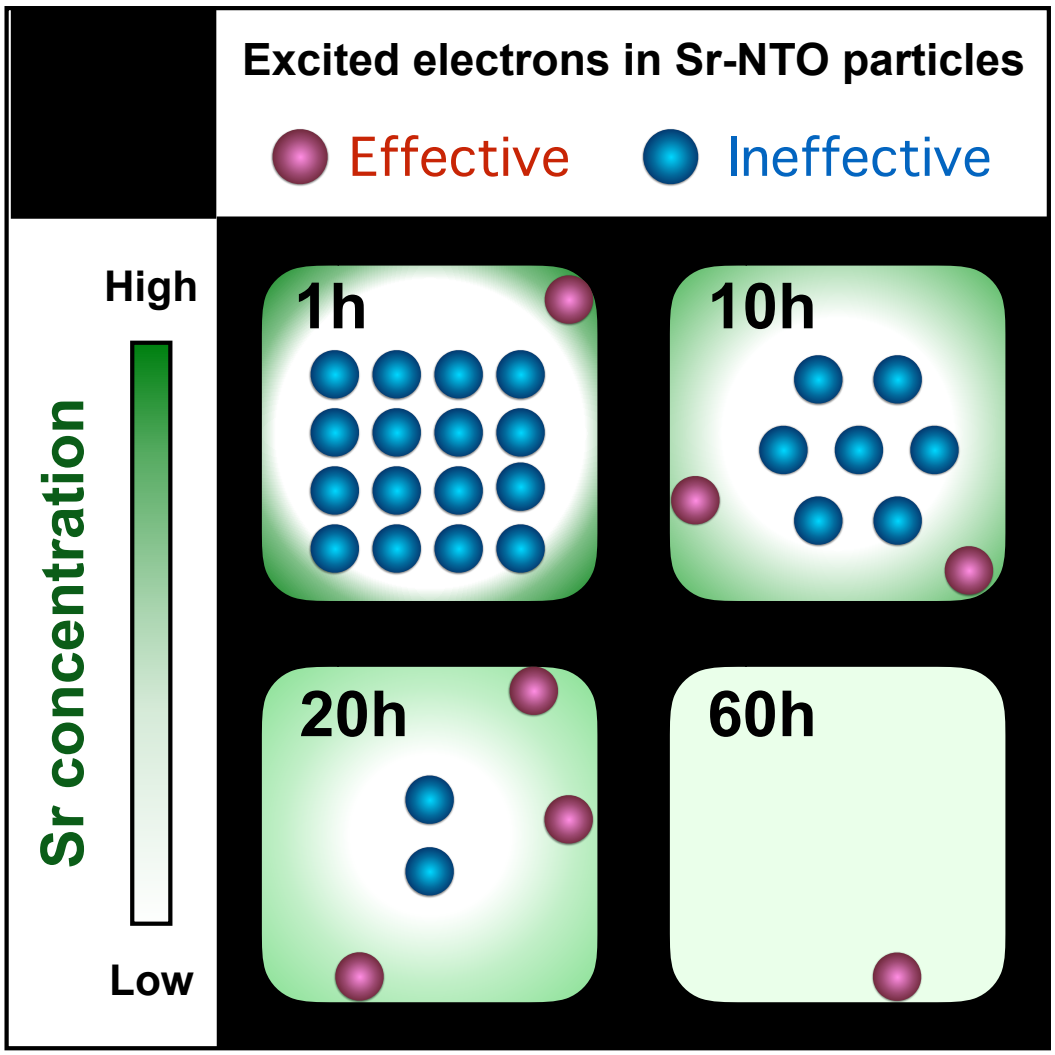

Figure 5.13. Schematic illustration of effective/ineffective ratio of excited electrons in Sr-NTO. Radial distribution of Sr in each Sr-NTO is illustrated.

5.4 CONCLUSION

1) In MSM, radial distribution of Sr was successfully controlled with heating time, in a range of 1-60 h, when the Sr concentration was fixed at 2 mol%. Inhomogeneous Sr distribution was produced by heating for 1 h, and the homogeneity of Sr distribution increased gradually with extended heating time. In 1h-heating, the population of excited electrons increased to 159 times as that of undoped $NaTaO_3$. The electron population decreased gradually with extended heating time, eventually, to 9 times at 60 h. In 1h-heating, the concentration gradient of Sr doped at B-sites (CGSrB) restricted the electron-hole recombination efficiently.

2) When surface Sr segregation was removed by HF etching in 1h-heated Sr-doped $NaTaO_3$, the relative electron population decreased from 159 to 65. The significant role of CGSrB on electron-hole recombination is thus confirmed. It also suggests excited electrons separated from holes mainly on the surface layer of particles. While in 60 h, electron population slightly increased from 9 to 17 after HF etching. Without CGSrB, the effect of etching is inconsiderable.

3) Water splitting activity increased gradually with a heating time of 1-20 h, but decreased with 60 h. In 1h-heating, CGSrB with high degree produced energy barrier in conduction band for preventing surface movement of electrons from bulk. The population of electrons cable of reaching the surface is thus limited, despite the fact that the total electron population is large. In 20h-heating, the energy barrier was reduced drastically by weakened CGSrB degree. Electrons kept in bulk, hence, easily moved to surface for participating water splitting reaction. While in 60h-heating, the total population of excited electrons decreased a lot due to the absence of CGSrB. The population of the excited electrons that can move to the surface was remained little compared to 20h-heating. Adjustment of CGSrB degree is thus a key to controlling water splitting activity.

5.5 REFERENCE

(1) S, Lee.; K, Teshima.; Y, Mizuno.; K, Yubuta.; T, Shishido.; M, Endo.; S, Oishi.; *CrystEngComm* **2010**, *12*, 2871-2877.

(2) McNab, J.; Sandborg, A. *The EDAX EDITOR*, *Vol. 14*, p. 37.

(3) Ahtee, M.; Unonius, L. Acta Crystallogr., Sect. A: Cryst. Phys., Diffr., Theor. Gen. *Crystallogr.* **1977**, *33*, 150-154.

(4) Teixeira, N. G.; Dias, A.; Moreira, R. L.; *J. Euro. Ceram. Soc.* **2007**, *27*, 3683-3686.

(5) Siny, I. G.; Tao, R.; Katiyar, R. S.; Guo, R.; Bhalla, A. S. *J. Phys. Chem. Solids* **1998**, *59*, 181-195.

(6) Zheng, H.; Reaney, I. M.; Csete de Györgyfalva, G. D. C.; Ubic, R.; Yarwood, J.; Seabra, M. P.; Ferreira, V. M. *J. Mater. Res*. **2004**, *19*, 488-495.

(7) Yamakata, A.; Ishibashi, T.; Kato, H.; Kudo, A.; Onishi, H. *J. Phys. Chem. B* **2003**, *107*, 14383-14387.

(8) Furuhashi, K.; Qingxin, J.; Kudo, A.; Onishi, H. *J. Phys. Chem. C* **2013**, *117*, 19101-19106.

(9) Yamakata, A.; Ishibashi, T.; Onishi, H. *Chem. Phys. Lett.* **2001**, *333*, 271-277.

(10) Choi, M.; Oba, F.; Tanaka, I. *Phys. Rev. B: Condens. Matter Mater. Phys.* **2008**, *78*, 014115 (8 pages).

(11) Kato, H.; Kobayashi, H.; Kudo, A. *J. Phys. Chem. B* **2002**, *106*, 12441-12447.

(12) Modak, B.; Srinivasu, K.; Ghosh, S.K. *Phys. Chem. Chem. Phys.* **2014**, *16*, 17116-17124.

(13) Ueno, K.; Inoue, I.H.; Akoh, H.; Kawasaki, M.; Tokura, Y.; Takagi, H. *Appl. Phys. Lett.* **2003**. *83*. 1755-1758.

(14) Ueno, K.; Inoue, I.H.; Yamada, T.; Akoh, H.; Tokura, Y.; Takagi, H. *Appl. Phys. Lett.* **2004**. *84*. 3726-3728.

(15) Li, Ailong.; Wang, Z.; Yin, H.; Wang, S.; Yan, P.; Huang, B.; Wang,X.; Li, R.; Zong, X.; Han, H.; Li, C. *Chem. Sci.* **2016**, *7*, 6076-6082.

Chapter 6

X-ray absorption fine structure

6.1 INTRODUCTION

Chapter 3 of this thesis stated the significant effect of B-site doping of Sr in $NaTaO_3$ photocatalyst on the restricted recombination of electrons and holes. Sr-doped $NaTaO_3$ prepared via solid-state method (SSM) presented the Raman band assigned to an asymmetric TaO_6 breathing vibration caused by Sr that substituted partial Ta at B-sites. Lattice expansion induced by substitution of smaller Ta with larger Sr was also detected by XRD. A supportive study for verifying the doping site of Sr in $NaTaO_3$ was conducted by X-ray absorption spectroscopy (XAS) in this chapter. A-site doping of metal dopants (La) was detected in La-doped $NaTaO_3$ (SSM) by observing XAFS of La due to an earlier study[1]. In this study, simultaneous doping of Sr at A- and B-sites of NTO (SSM) is discussed.

The local structure of Sr in $NaTaO_3$ was detected by observing the X-ray absorption fine structure (XAFS). By analyzing the X-ray absorption near edge structure (XANES) and the extended X-ray absorption fine structure (EXAFS), the doping site of Sr can be known according to a verification of coordination number of Sr and distances of Sr to adjacent atoms. The XAFS measurement provides a more straight information of Sr doping site rather than the Raman spectroscopy or XRD.

In chapter 3, the $NaTaO_3$-$Sr(Sr_{1/3}Ta_{2/3})O_3$ solid solution model was assumed to explain a gradual lattice expansion induced by Sr doping via SSM. The theory requires evidence of simultaneous doping of Sr at A- and B-sites in Sr-doped $NaTaO_3$ (SSM). The EXAFS of Sr observed in this chapter presented the necessary evidence. The EXAFS spectra of Sr-doped $NaTaO_3$ with various Sr concentrations are similar with that of $Sr(Sr_{1/3}Ta_{2/3})O_3$, which has three A-site doping accompany with one B-site doping of Sr. Therefore, Sr substituted both A- and B-sites when doped via SSM. And the amount ratio of Sr doped at A-site/B-site is near to 3 as well as $Sr(Sr_{1/3}Ta_{2/3})O_3$.

The confirmation of doping site by XAFS was also conducted on Sr-doped $NaTaO_3$ prepared via hydrothermal method (HTM) and molten salt method (MSM). Results of XANES observation supports the doping site of Sr via each synthesis method as stated in the previous chapters, that is, simultaneous doping at A- and B-sites via SSM and MSM, but at A-sites alone via HTM. However, in EXAFS analysis, the A-site doping of Sr alone is not supported in HTM prepared Sr-doped $NaTaO_3$, may be due to the complex structure caused by water involved environment during synthesis.

6.2 EXPERIMENTAL SECTION

6.2.1 Synthesis and HCl washing

Synthesis of $NaTaO_3$ and Sr-doped $NaTaO_3$ used in this chapter was the same as the previous chapters. Some of the samples were washed with HCl solution to remove any unreacted SrO, the amount of which is too small to be detected by XRD, remained in the product.

As prepared sample (1 g) was stirred in a Teflon jar containing an aqueous HCl solution (1 wt%, 20 ml, Wako) for 10 minutes. Then washed with purified water until the pH was maintained at about 7.

Hereafter, a 2 mol% Sr-doped $NaTaO_3$ prepared through HTM is referred to as 2%Sr-NTO/ HCl (HTM) when it was washed with HCl, and so on.

6.2.2 Characterization

The X-ray absorption fine structure (XAFS) was observed to determine the local structure of Sr. Synchrotron radiation (BL-12C in Photon Factory) was used as the X-ray resource. XAFS of Sr-doped $NaTaO_3$ photocatalysts with Sr concentration less than 2 mol% were detected by a fluorescence method using multi-element SSD (19 elements) and the other Sr-doped $NaTaO_3$ photocatalysts were detected by a transmission method.

6.3 RESULTS AND DISCUSSION

6.3.1 X-ray absorption near edge structure (XANES)

Figure 6.1 shows Sr K-edge X-ray absorption near edge structure (XANES) spectra of Sr-NTOs (SSM) with various Sr concentration. SrO and $SrTiO_3$ were measured as reference samples. Coordination number (C.N.) of Sr-O shell in SrO and $SrTiO_3$ are 6 and 12, respectively, which is consistent to the Sr doped at B-sites (C.N. = 6) and A-sites (C.N. = 12) in Sr-NTO.

The dashed line in **Fig. 6.1** indicates the X-ray absorption peak top of 2%Sr-NTO (SSM). The peak top energy of 2%Sr-NTO (SSM) is presented in the middle of the two reference samples, SrO and $SrTiO_3$. Thus, the author assumes simultaneous doping of Sr at A- and B-sites in 2%Sr-NTO (SSM).

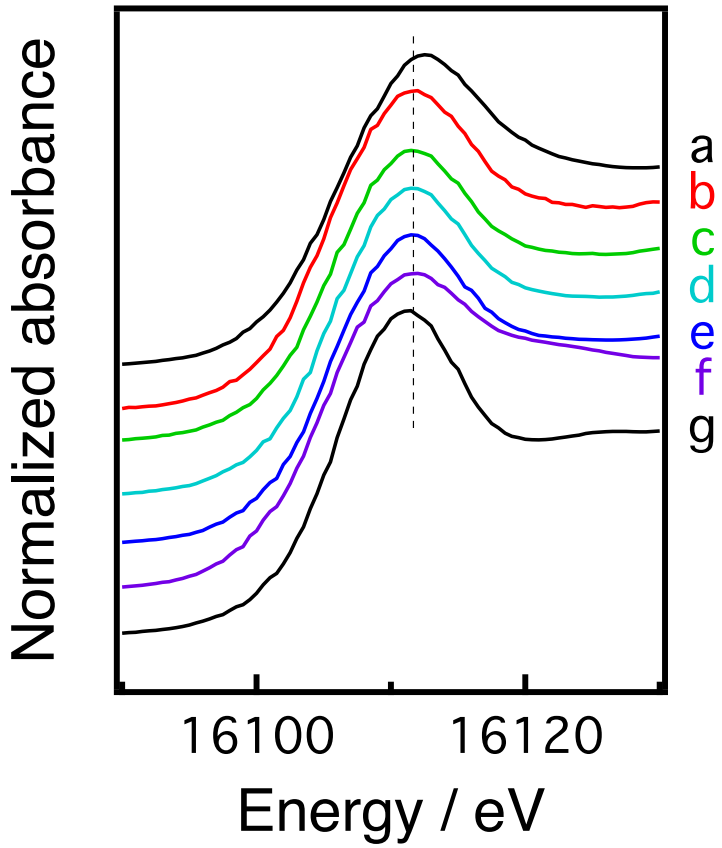

Figure 6.1 Sr K-edge XANES spectra of (a) SrO, (b) 2%Sr-NTO (SSM), (c) 8%Sr-NTO (SSM), (d) 20%Sr-NTO (SSM), (e) 50%Sr-NTO (HTM), (f) SSTO (SSM), and (g) $SrTiO_3$. The dashed line indicates the peak top of trace b.

The other Sr-NTOs (SSM) presented similar X-ray absorption peak top energy as the 2%Sr-NTO (SSM). It not only explains the simultaneous doping of Sr at A- and B-sites, but also suggests the ratio of Sr doped A-sites/B-sites is almost the same in Sr-NTOs (SSM), despite the Sr concentration varied from 2 mol% to 50 mol%. In SSTO, three A-site doping of Sr accompanied with one B-site doping. It is the same case in Sr-NTOs (SSM).

In chapter 3, the peak shift of XRD and Raman band at 860 cm^{-1} provided strong evidence of B-site doping in Sr-NTO (SSM). To keep the charge balance in Sr-NTO, A-site doping was assumed to exist coincident with B-site doping. The XANES spectra of Sr-NTOs (SSM) in this chapter supports the simultaneous presence of A- and B-site doping.

XANES of the Sr-NTOs prepared via different methods were also checked, and the results are shown in **Fig. 6.2**. **Panel (A)** shows energy comparison on peak top of 2%Sr-NTOs prepared via SSM, MSM, and HTM. In HTM, 2%Sr-NTO (HTM) was washed with HCl to remove any remained SrO that is not yet reacted. The Sr concentration decreased from 2.0 mol% to 1.6 mol%, as detected by EDX. The dashed line indicates the peak top energy of $SrTiO_3$. The peak was slightly shifted to lower energy in a sequence of SrO, 2%Sr-NTO (SSM), 2%Sr-NTO (MSM), 2%Sr-NTO (HTM), and 2%Sr-NTO/HCl (HTM), eventually, getting close to that of $SrTiO_3$. The 2%Sr-NTOs (SSM and MSM) showed the same XANES peak energy, while the peak was little shifted to lower energy in 2%Sr-NTO (HTM) and 2%Sr-NTO/HCl (HTM).

A more careful comparison of 2%Sr-NTO (HTM) before and after HCl washing is shown in **Panel (B)**. A slight peak shift to lower energy after HCl washing is attributed to the removal of the SrO remained in the 2%Sr-NTO (HTM). Therefore, the Sr doped at A-sites via HTM were mainly detected by XAS after HCl washing.

In summary, Sr should have been simultaneously doped at A- and B-sites when prepared via SSM and MSM. In HTM, some of the Sr did not completely react that being remained as SrO in the product. While the reacted Sr was mainly doped at A-sites. The results are well consistent with the assumptions as stated in the previous chapters.

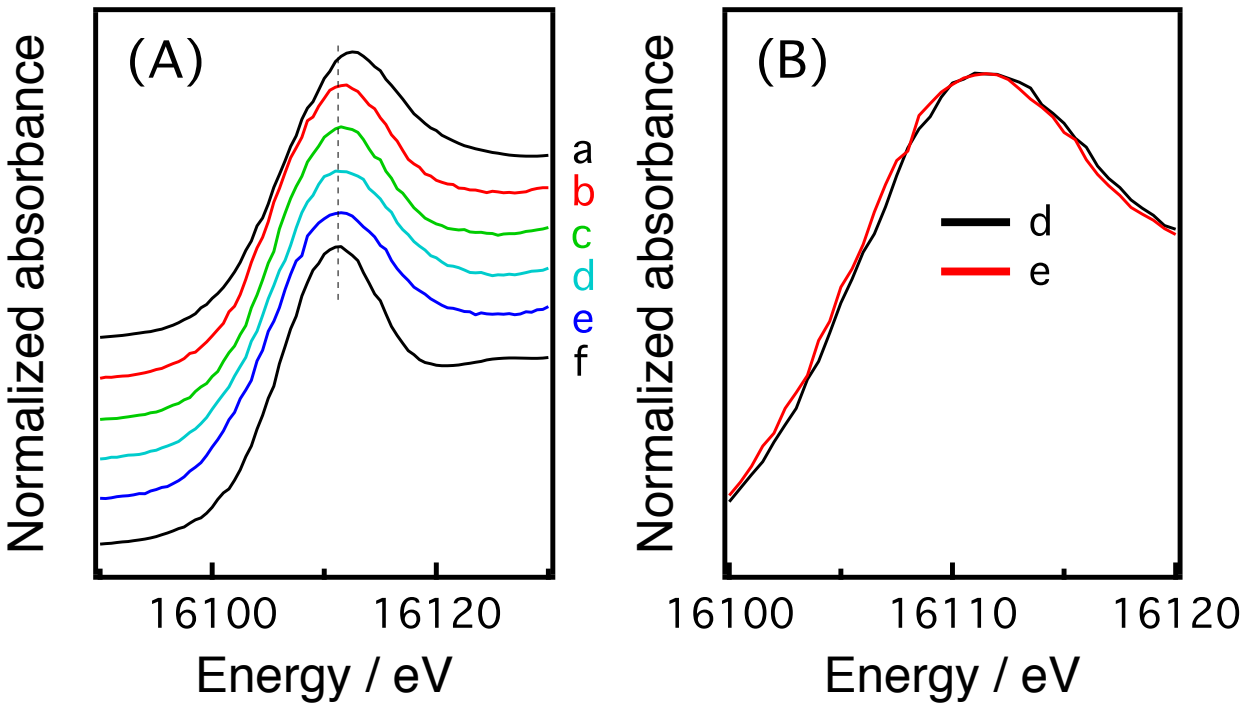

Figure 6.2 Sr K-edge XANES spectra of (a) SrO, (b) 2%Sr-NTO (SSM), (c) 2%Sr-NTO (MSM), (d) 2%Sr-NTO (HTM), (e) 2%Sr-NTO/HCl (HTM), and (f) $SrTiO_3$. The dashed line in panel A indicates the peak top of trace f. The trace d and e are carefully compared in panel B.

6.3.2 Extended X-ray absorption fine structure (EXAFS)

Extended X-ray absorption fine structure (EXAFS) interpretation was performed on Sr-NTOs prepared via various methods to identify Sr doping sites by verifying the Sr-O distances.

50%Sr-NTO (SSM) was washed with HCl solution to remove impurity phase (SrO) from the perovskite-structured Sr-NTO. The Sr concentration decreased from 49.0 mol% to 44.2 mol% by HCl washing. Among various Sr-NTOs (SSM), 50%Sr-NTO (SSM) exhibited the best EXAFS signal. Thus the impurity removed 50%Sr-NTO/HCl (SSM) should provide better accuracy of EXAFS signal.

Figure 6.3(A) shows Ta L_3-edge EXAFS spectra of 50%Sr-NTO/HCl (SSM) in addition to NTO (SSM), NTO (HTM), and NTO (MSM). With k selected in a range of 3-13 $Å^{-1}$, NTO (MSM) exhibited the clearest oscillation signal among three NTOs prepared via different methods. In a comparison on the EXAFS oscillation, only 50%Sr-NTO/HCl (SSM) presented apparent difference from the other three NTOs, which showed high identity. It indicates the Sr doping caused changes in the local structure of Ta in NTO.

EXAFS spectra of NTO (MSM) were Fourier transformed (FT) to present the local structure of Ta in NTO visually. **Figure 6.3(B)** shows the FT results of NTO (MSM) in addition to the curve-fitting (CF) analysis. The FT was performed with k in a range 3-13 $Å^{-1}$. NTO (MSM) presented four major peaks within 1.0-2.0 Å, 2.5-3.2 Å, 3.5-4.3 Å, and 5.0-6.0 Å, respectively. CF was conducted to each of the four peaks using NTO (62 Pnma group) structure model, which has an orthorhombic structure. The lattice constants followed with an earlier study,[2] that is a = 0.552 nm, b = 0.779 nm, c = 0.548 nm. As a result, the peak within 1.0-2.0 Å is assigned to Ta-O shell in NTO, 2.5-3.2 Å is assigned to Ta-Na, 3.5-4.3 Å is assigned to Ta-Ta, and 5.0-6.0 Å is assigned to Ta-Ta in a diagonal direction. Detailed results of CF are summarized in **Table 6.1**. There are four parameters shown in the table, where the N represents the coordination number of Ta to adjacent atom, R represents the curve-fitted atomic distance, ΔE represents the X-ray absorption edge difference between simulation and the model, and DW represents the Debye-Waller factor.

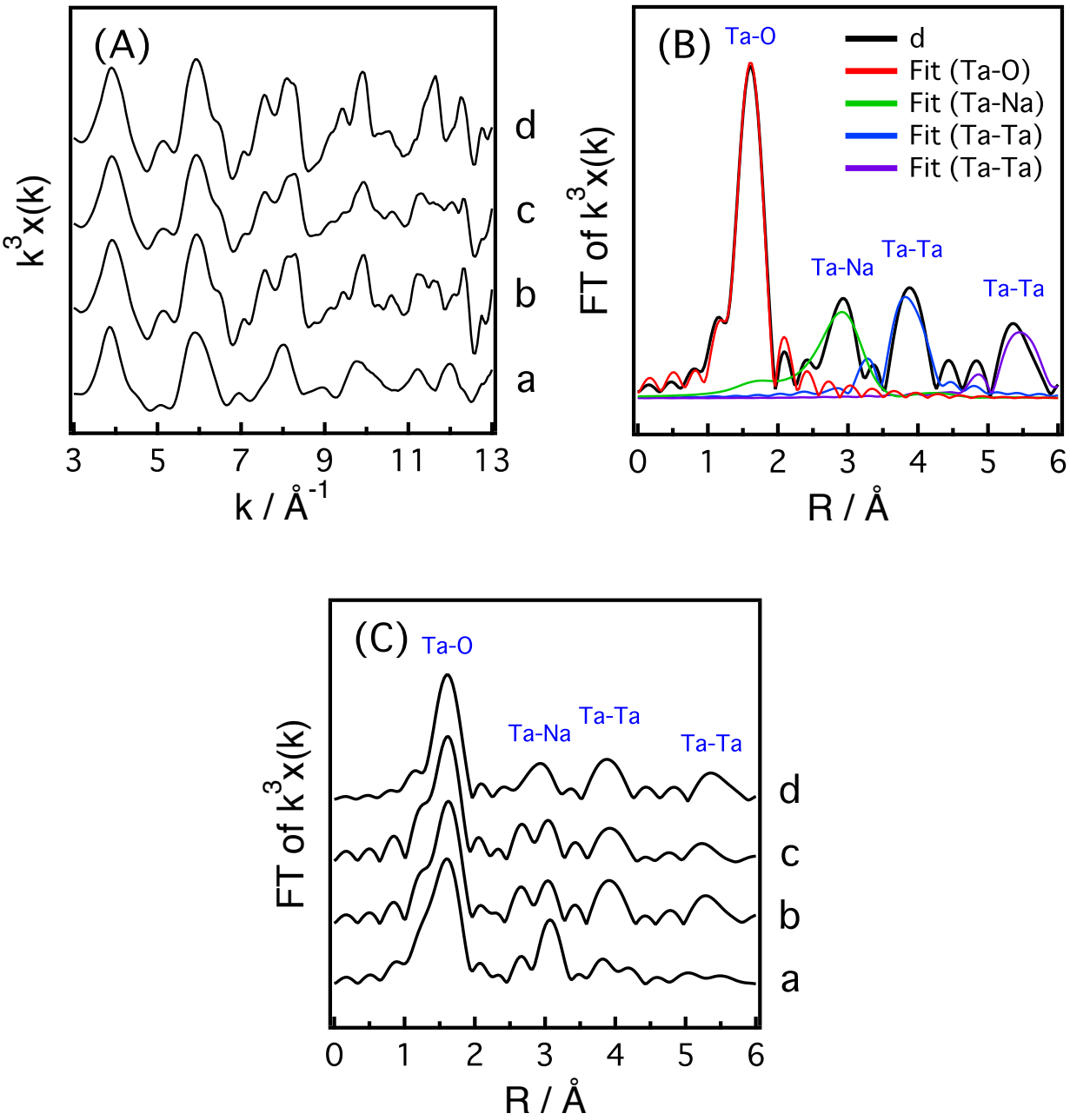

Figure 6.3 (A) Ta L_3-edge EXAFS spectra of a: 50%Sr-NTO/HCl (SSM), b: NTO (SSM), c: NTO (HTM), and d: NTO (MSM). (B) Fourier transform (FT) of EXAFS spectrum of trace d. Curve fitting was performed on trace a in a range of 1.0-2.0 Å for Ta-O scattering, 2.5-3.2 Å for Ta-Na, 3.5-4.3 Å for Ta-Ta, and 5.0-6.0 for Ta-Ta (diagonal two Tantalums). (C) FT of EXAFS spectra of traces a-d.

From knowing the assignment of each peak in FT EXAFS spectra of NTOs, the peak changing caused by Sr doping in Sr-NTO was considered. **Figure 6.3(C)** shows a comparison of FT EXAFS spectra of 50%Sr-NTO/HCl (SSM) with NTOs prepared via various methods. The intensities were normalized in the peak within 1.0-2.0 Å. The three NTOs exhibited similar spectra as expected in **Fig. 6.3(A)**. But in the case of 50%Sr-NTO/HCl (SSM), the peak intensity of Ta-Na shell increased; meanwhile, Ta-Ta shell decreased.

The intensity changes in the Ta-Na and Ta-Ta shells can be explained with simultaneous doping of Sr at A- and B-sites. Sr will substitute Na in the case of A-site doping. Due to the larger atomic number of Sr (38) than Na (11), the EXAFS signal of the Ta-Sr shell should be stronger than Ta-Na shell. Therefore, the increased intensity of Ta-Na shell indicates some of the doped Sr substituted Na at A-sites. On the other hand, Sr will replace Ta in B-site doping. Since Sr has a smaller atomic number than Ta (73), the intensity of Ta-Sr shell should be weaker than that of Ta-Ta shell. It explains some of the doped Sr substituted Ta at B-sites. Consequently, Sr is assumed to substitute both A- and B-sites in 50%Sr-NTO/HCl (SSM).

Peak range	N	R / Å	ΔE / eV	DW / Å^2
1.0-2.0 Å	4.8	1.92	9.4	0.0014
2.5-3.2 Å	18.9	3.32	4.4	0.0156
3.5-4.3 Å	7.0	3.96	12.7	0.0064
5.0-6.0 Å	12.1	5.55	14.1	0.0064

Table 6.1. Results of curve fitting on NTO (MSM).

Simultaneous doping of Sr at A- and B-sites in 50%Sr-NTO/HCl (SSM) can also be supported with Sr K-edge EXAFS spectrum, as shown in **Fig. 6.4**. **Panel (A)** shows EXAFS spectra of 50%Sr-NTO/HCl (SSM) obtained in Ta L_3-edge and Sr K-edge, respectively. The Sr K-edge EXAFS oscillation is different from the Ta L_3-edge. It suggests the local structure of doped Sr is distinct from that of Ta in 50%Sr-NTO/HCl (SSM). **Panel (B)** shows FT EXAFS spectra for visualizing the difference. Sr K-edge FT EXAFS presented an additional peak from Ta L_3-edge at 2.0 Å. The 1.5 Å peak detected both in Ta L_3-edge and Sr K-edge absorption should attributed to Sr(B)-O shell, where the Sr(B) represents the Sr doped at B-sites. The assignment of the additional peak at 2.0 Å is needed to determine.

In pristine NTO, the second coordination sphere of Ta is Ta-Na. The FT EXAFS peak attributing to Ta-Na is presented at 3.0 Å. The extra peak at 2.0 Å is apparently not assigned to the coordination of Sr doped at B-sites. A possible assignment of 2.0 Å peak is thus Sr(A)-O coordination. In the model of NTO (62 Pnma group), the Ta-O distance is 1.9 Å and the Na-O distance is 2.4 Å. Considering the photoelectrons scattered on the electron shell around the scattering atom, the measured distance is usually shorter than the real distance. It explains the change in distance between measured Sr(B)-O and ideal Ta-O. In the same way, the peak at 2.0 Å is highly assumed to be assigned to Sr(A)-O shell.

To verify the assumption, CF was performed on the peaks at 1.5 Å and 2.0 Å, as shown in **Panel (C)**. Backward FT of the peaks and the CF are shown in **Panel (D)**. In the orthorhombic model of NTO, there are three Ta-O coordinations with different atomic distance fits on the 1.5 Å peak, and two different Na-O coordinations fits on the 2.0 Å peak. Detailed CF results are summarized in **Table 6.2**. The acceptable CF parameters show the 1.5 Å and 2.0 Å peaks are assigned to Sr(B)-O and Sr(A)-O coordinations, respectively.

Peak	N (total)	R / Å (each)	ΔE / eV	DW / Å^2
1.5 Å	1.8	1.95, 2.00, 2.05	-13.1	0.0048
2.0 Å	3.8	2.36, 2.40	6.9	0.0132

Table 6.2. Results of curve fitting on NTO (MSM).

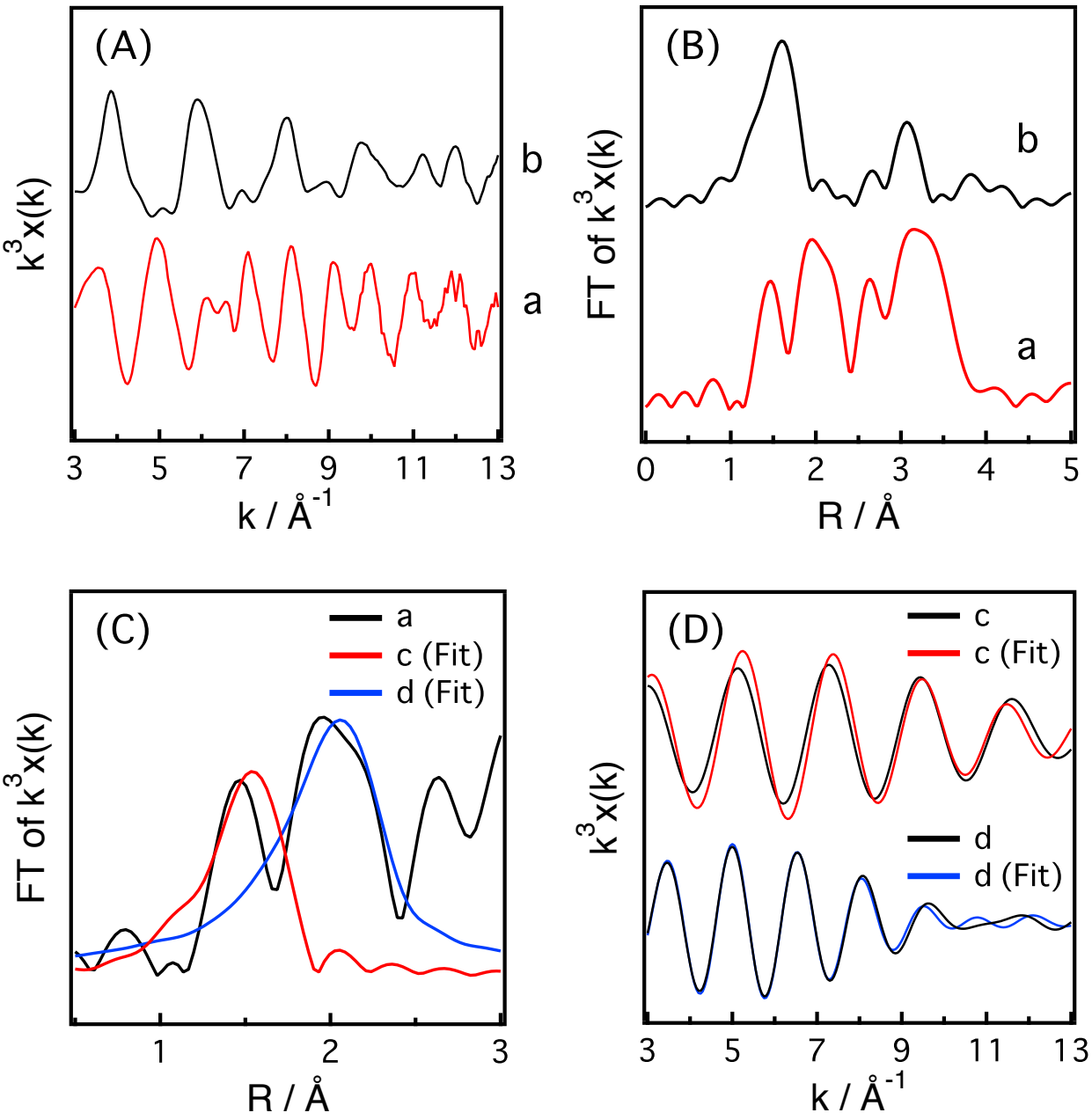

Figure 6.4 (A) EXAFS spectra of 50%Sr-NTO/HCl (SSM) on a: Sr K-edge, and on b: Ta L_3-edge. (B) FT of EXAFS spectra. (C) Curve fitting on trace a. Fitting operated on peak at 1.5 Å is presented as trace c (Fit), and 2.0 Å as trace d (Fit). (D) Backward FT of peak at 1.5 Å is shown as c and 2.0 Å as d.

In 50%Sr-NTO/HCl (SSM), the coexistence of FT peak at 1.5 and 2.0 Å provided strong evidence to simultaneous doping of Sr at A- and B-sites. Doping site of Sr was also detected on the other Sr-NTOs (SSM). **Figure 6.5(A)** shows EXAFS spectra of Sr-NTOs (SSM) with various Sr concentration. In general, all the Sr-NTOs show similar spectra. It indicates Sr concentration does not control the local structure of Sr in Sr-NTOs (SSM).

Figure 6.5(B) shows FT of EXAFS spectra, where the FT was operated with k in a range of 3-13 $Å^{-1}$. All the Sr-NTOs exhibited at least two different coordinations of Sr-O shells at 1.5 and 2.0 Å. According to the above analysis of 50%Sr-NTO/HCl, 1.5 Å peak should represent Sr(B)-O coordination, and 2.0 Å peak represents Sr(A)-O. The identification of the different types of Sr-O coordinations is confirmed in Sr-NTOs as well as in 50%Sr-NTO/HCl.

The clear separation of FT peaks attributing to the Sr-O shells is also observed in SSTO. The intensity ratio of peaks at 2.0 Å/1.5 Å in SSTO is similar to the other Sr-NTOs. The amount ratio of Sr doped at A-site/B-site is 3 in a perfect perovskite-structured SSTO.[3] Therefore, almost three Sr doping at A-sites should accompany with one Sr doping at B-sites in Sr-NTOs (SSM). It supports well the model of $NaTaO_3$-$Sr(Sr_{1/3}Ta_{2/3})O_3$ solid solution in Sr-NTOs (SSM) that suggested in chapter 3.

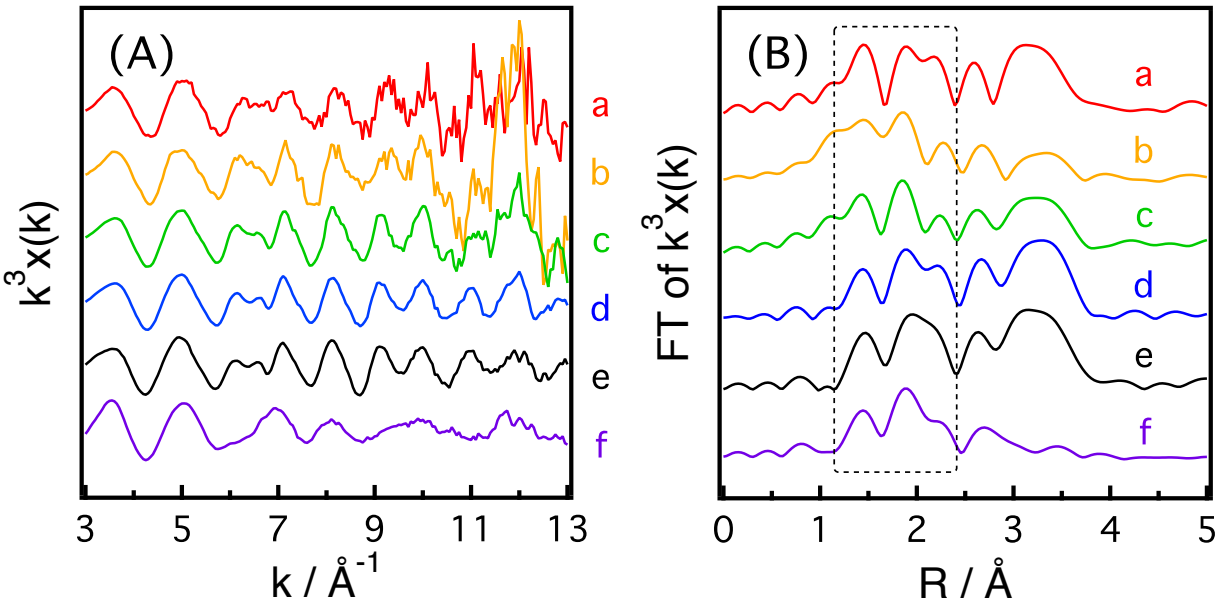

Figure 6.5 (A) Sr K-edge EXAFS spectra of SSM prepared a: 2%Sr-NTO, b: 8%Sr-NTO, c: 20%Sr-NTO, d: 50%Sr-NTO, e: 50%Sr-NTO/HCl, and f: $Sr(Sr_{1/3}Ta_{2/3})O_3$. (B) FT of EXAFS spectra.

In the previous chapters, Sr was assumed to substitute both A- and B-sites when doped via SSM and MSM, but substitute A-sites alone when doped via HTM. In this subsection, Sr doping sites in Sr-NTOs prepared via the three methods were examined by observing EXAFS of Sr.

Figure 6.6(A) shows Sr K-edge EXAFS spectra of 2%Sr-NTO (SSM), 2%Sr-NTO (MSM), and 2%Sr-NTO/HCl (HTM) with k in a range of 3-13 $Å^{-1}$. Each EXAFS spectrum of the samples presented weak S/N due to the limited Sr concentration. Compared to the relatively stable oscillation of EXAFS signals in 2%Sr-NTO (SSM) and 2%Sr-NTO (MSM), 2%Sr-NTO/HCl (HTM) exhibited abnormal EXAFS signal with $k > 11$ $Å^{-1}$. The abrupt change in the oscillation might be caused by artificial elements, such as a sudden change of incident X-ray intensity during measurement. Although, the exact reason is uncertain.

To remove any results that are caused by artificial elements, the EXAFS spectrum of each samples was Fourier transformed with k ranges of 3-11 $Å^{-1}$. A direct effect from shrinking the k range is the decline in accuracy of FT EXAFS spectrum. **Figure 6.6(B)** shows the FT EXAFS spectra of the three samples. 2%Sr-NTO (SSM) and 2%Sr-NTO (MSM) presented almost the same FT spectra in a range of 1.0-4.0 Å. On the other hand, 2%Sr-NTO/HCl (HTM) showed different spectrum within a range of 2.5-4.0 Å, but similar spectrum at 1.0-2.5 Å, from that of 2%Sr-NTO (SSM). The difference in 2.5-4.0 Å indicates the local structure of Sr in Sr-NTO (HTM) is different from that of Sr-NTO (SSM). However, the similarity in 1.0-2.5 Å suggests a conflicting result that the local structure of Sr is the same when doped via SSM or HTM. To clarify the contradiction, backward FT was operated for the FT EXAFS signals with R in a range of 1.0-2.5 Å.

Figure 6.6(C) shows backward FT spectra. Almost the same spectra were detected in 2%Sr-NTO (SSM) and 2%Sr-NTO (MSM). 2%Sr-NTO/HCl (HTM) exhibited a finite but clear difference in the backward FT spectra from the other two samples. It suggests the local structure of Sr in 2%Sr-NTO/HCl (HTM) is different from that of 2%Sr-NTO (SSM) and 2%Sr-NTO (MSM). Although the exact Sr doping site in 2%Sr-NTO/HCl (HTM) is unclear from the EXAFS measurement in this study due to the weak S/N, the Sr doping site should be different from 2%Sr-NTO prepared via SSM or MSM, as expected. On the other hand in SSM and MSM, Sr substituted both A- and B-sites as well as 50%Sr-NTO/HCl (SSM).

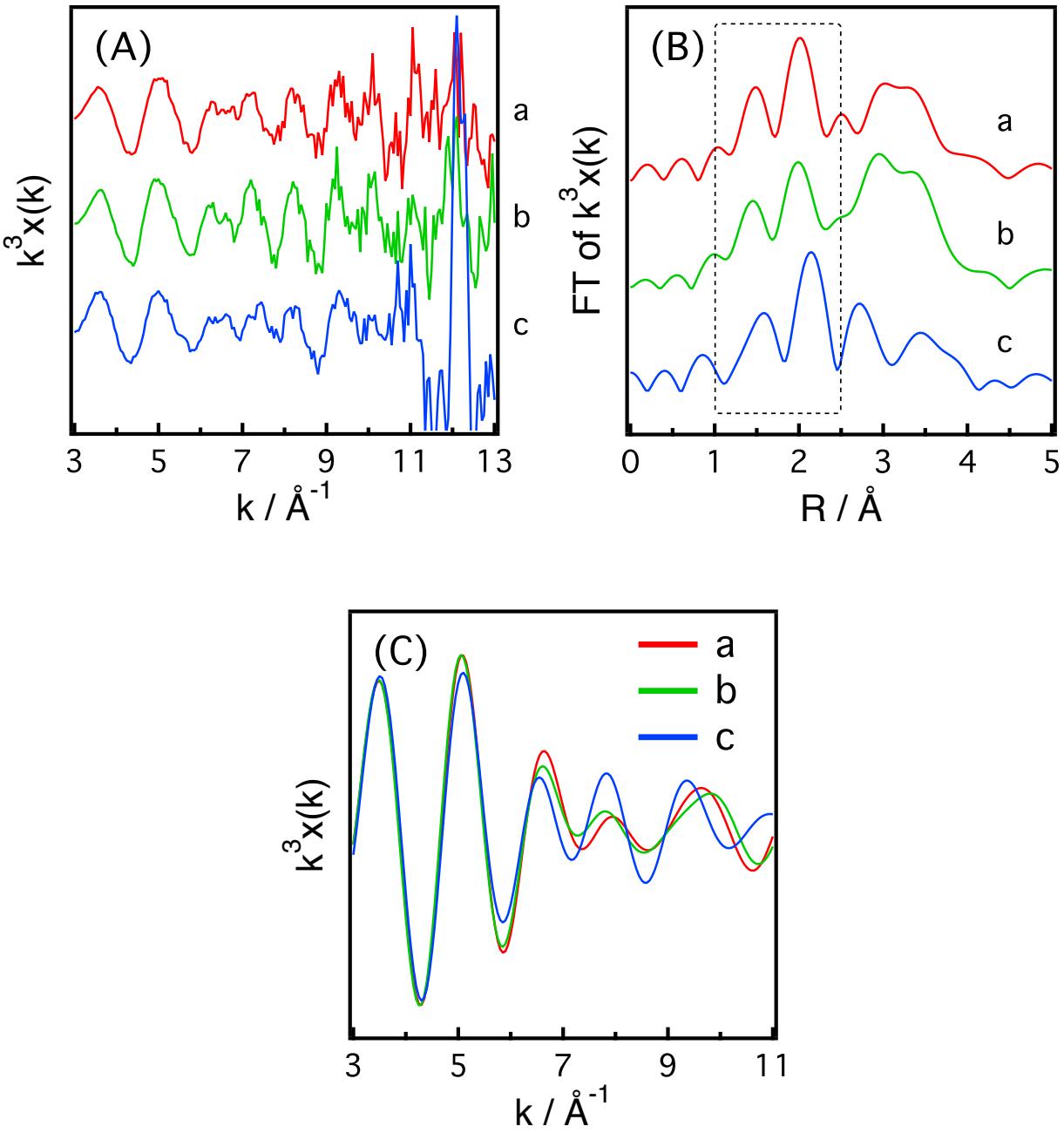

Figure 6.6 (A) Sr K-edge EXAFS spectra. (B) FT with k in a range of 3-11 Å^{-1} of EXAFS spectra. (B) FT of EXAFS spectra. (C) Backward FT with R in a range of 1.0-2.5 Å. a: 2%Sr-NTO (SSM), b: 2%Sr-NTO (MSM), and c: 2%Sr-NTO/HCl (HTM).

6.4 CONCLUSION

1) In Sr K-edge XANES interpretation, the X-ray absorption peak top is almost the same on Sr-NTOs prepared via SSM. The peak top energy of Sr-NTOs (SSM) is located between that of SrO (C.N. = 6) and $SrTiO_3$ (C.N. = 12). Hence the Sr should substitute both A- and B-sites when doped via SSM. MSM-prepared Sr-NTO showed the same peak top energy as SSM. But in Sr-NTO (HTM) before and after HCl washing, the peak top is shifted to lower energy than that of Sr-NTO (SSM). The energy is very close to $SrTiO_3$. The C.N. of Sr in $SrTiO_3$ is 12, which is the same as Sr substituted A-sites in Sr-NTO. In summary, Sr substitute both A- and B-sites when doped via SSM and MSM, but only substitute A-sites when doped via HTM.

2) In Ta L_3-edge EXAFS interpretation, 50%Sr-NTO/HCl (SSM) presented a stronger peak at 2.5-3.2 Å corresponding to Ta-Na coordination, and a weaker peak at 3.5-4.3 Å corresponding to Ta-Ta coordination, when compared to NTO (SSM). It indicates simultaneous doping of Sr at A- and B-sites. In A-site doping, Sr with the larger atomic number should substitute Na to increase the Ta-Na intensity. On the other hand, in B-site doping, Sr with smaller atomic number substituted Ta to decrease Ta-Ta intensity.

3) In Sr K-edge EXAFS interpretation, all the Sr-NTOs (SSM) exhibited two Sr-O coordination peaks at 1.5 and 2.0 Å, respectively. 1.5 Å peak was attributed to Sr doped at B-sites, and 2.0 Å peak was attributed to Sr doped at A-sites. Sr-NTO (MSM) showed the same EXAFS spectrum as Sr-NTO (SSM) but Sr-NTO/HCl (HTM) showed different spectrum. Sr should substitute both A- and B-sites when doped via SSM and MSM. While the exact doping site of Sr in Sr-NTO/HCl (HTM) is not clear due to the low S/N in this study.

6.5 REFERENCE

(1) Shimura, Katsuya.; Kato, S.; Yoshida, T.; Itoh, H.; Hattori, T.; Yoshida, H. *J. Phys. Chem. C* **2010**, *114*, 3493-3503.

(2) Kanhere, D.P.; Zheng, J.; Chen, Z. *J. Phys. Chem. C* **2011**, *115*, 11846-11853.

(3) Caldes, M.T.; Deniard, P.; Zou, X.D.; Marchand, R.; Diot, N.; Brec, R. *Micron* **2001**, *32*, 497-507.

Chapter 7

General conclusion

In **chapter 3**, $NaTaO_3$ was doped with Sr via three methods for the examination of the effect of Sr doping sites on electron-hole recombination.

1) In SSM, Sr was doped A- and B-sites, simultaneously, to form a solid solution of $NaTaO_3$-$Sr(Sr_{1/3}Ta_{2/3})O_3$, as shown in section 3.3.1. Electron-hole recombination was restricted accordingly as B-site doping.

2) In HTM (section 3.3.2), Sr was doped at A-sites alone. As a result, electron-hole recombination was not affected by doping.

3) In STM (section 3.3.3), B-site doping of Sr, again, restricted electron-hole recombination.

In **chapter 4**, Sr-doped $NaTaO_3$ prepared via SSM was etched with HF solution for checking the radial distribution of Sr. Sr distribution highly controlled the electron-hole recombination.

1) As shown in section 4.3.1, 5% Sr-doped $NaTaO_3$ produced a core-shell structure. In the shell, a complex structure and serious Sr segregation accelerated recombination of electrons and holes. While in the core, a smooth concentration gradient of Sr doped at B-sites restricted the charge recombination.

2) In section 4.3.2, the possible effect of F^- anions adsorbed on the surface was eliminated by etching undoped $NaTaO_3$. The population of photoexcited electrons was almost the same before and after F^- removal.

3) In section 4.3.3, HF etching was applied to $NaTaO_3$ doped with Sr at 1% and 8%, respectively. Core-shell structured 8% Sr-doped $NaTaO_3$ exhibited electron-hole recombination that was restricted in the core and recombined in the shell. On the other hand, doping of Sr at 1% produced the core alone. The electron-hole recombination was restricted in the core.

In **chapter 5**, Sr-doped $NaTaO_3$ was synthesized via MSM to control radial distribution of Sr. Inhomogeneous distribution of Sr doped at B-sites are believed to restrict electron-hole recombination.

1) Sr-doped $NaTaO_3$ photocatalysts with fixed Sr concentration but different Sr distribution were synthesized by adjusting heating time, as shown in section 5.3.1. Inhomogeneous distribution of Sr, which was produced under short heating time, restricted electron-hole recombination. While the extended heating time induced a homogeneous distribution of Sr. Limited suppression of charge recombination was revealed accordingly.

2) In section 5.3.2, results of HF etching confirmed the positive effect of the concentration gradient of Sr doped at B-sites on the suppression of electron-hole recombination.

3) In section 5.3.3, water splitting activity increased to a peak when heated for 20 h. The inconsistent results of the water splitting activity and the population of excited electrons suggest the significance of the number of electrons being able to transfer to the particle surface.

In **chapter 6**, XAFS of Sr-doped $NaTaO_3$ prepared via SSM, MSM and HTM was observed to determine the local structure of Sr.

1) In section 6.3.1, the XANES interpretation verified the simultaneous doping of Sr at A- and B-sites when doped via SSM and MSM. In HTM, only A-site doping is assumed.

2) In section 6.3.2, the EXAFS interpretation verified the simultaneous doping of Sr at A- and B-sites when doped via SSM and MSM. In HTM, the exact doping site is uncertain but is different from that of SSM or MSM.

In summary, Sr substituted both A- and B-sites of $NaTaO_3$ to produce solid solution of $NaTaO_3$-$Sr(Sr_{1/3}Ta_{2/3})O_3$ with Sr concentration gradient in SSM. Conduction band (CB) minimum potential was shifted upward by replacement of Ta^{5+} cations at B-sites with Sr^{2+} cations to form potential gradient of CB in radial direction. Band gap excited electrons transferred through the CB potential gradient in certain direction. Consequently, the electrons separated from the holes to restrict electron-hole recombination. In short, gradient of Ta concentration in radial direction is important to efficiency restriction of electron-hole recombination in $NaTaO_3$ photocatalyst.

ACKNOWLEDGEMENT

Firstly, I would like to express my special appreciation and thanks to my advisor Professor Dr. Hiroshi Onishi for the continuous support of my Ph.D study. His immense knowledge and patient leading helped me in all the time of research and study. As an international student living in Japan, may every day life would have been tough without the careful attention and the advice of life from professor Dr. Hiroshi Onishi. I could not have imagined having a better advisor and mentor for my Ph.D study and life in Japan.

Besides my advisor, I would like to express my sincere gratitude to Professor Dr. Yasuhiro Kobori, Professor Dr. Kazuyuki Takahashi, Professor Dr. Akira Sasahara, and Professor Dr. Takashi Tachikawa for their insightful comments and encouragement, but also for the hard questions which led me to consider deeply for my research from various perspectives.

I also would like to thank Professor Dr. Nobuyuki Ichikuni (Chiba University), Takuro Sasaki (Chiba University), Professor Dr. Akihide Iwase (Tokyo University of Science), Dr. Hidenori Saito (KAST), Dr. Yohan Park (Tokyo University), Dr. Mitsunori Kitta (AIST), for their kind assistance and technical support on XAFS measurement, H_2 evolution reaction rate from water splitting, SEM images, and TEM-EDX measurement. Without their precious support, it would not be possible to conduct this research.

My sincere thanks also goes to Professor Dr. Akihide Wada, Professor Dr. Kenjiro Kimura, Professor Dr. Kazuo Eda, and Professor Dr. Syunji Kasahara, for the valuable support on my study in Kobe University. The smooth progress of my Ph.D study depends highly on the precious advice and help in learning from them.

I thank my labmates in Onishi group and Kimura group, for the stimulating discussions, the linguistic help, and all the fun we have had in the last five years. This thesis can not be fully completed without the continuous encouragement from my labmates.

Also, I would like to express my gratitude to all of those who supported in any respect during the completion of this work.

Last but not the least, I would like to thank my family: my wife and my parents for supporting me spiritually and financially throughout writing this thesis and my life in general.

LIST OF PUBLICATIONS

1. “Electron–Hole Recombination Controlled by Metal Doping Sites in $NaTaO_3$ Photocatalysts”
   Longjie An, Hiroshi Onishi
   ACS catal. **2015**, *5*, 3196−3206.

2. “Rate of Ag Photodeposition on Sr-doped $NaTaO_3$ Photocatalysts as Controlled by Doping Sites”
   Longjie An, Hiroshi Onishi
   e-j. Surf. Sci. Nanotech. **2015**, *13*, 253−255.

3. “Effect of Etching on Electron–Hole Recombination in Sr-Doped $NaTaO_3$ Photocatalysts”
   Longjie An, Yohan Park, Youngku Sohn, and Hiroshi Onishi
   J. Phys. Chem. C **2015**, *119*, 28440−28447.